Sensitive, Label-free Biomolecular Binding Detection Using a One-dimensional Photonic Crystal Sensor

by

Yunbo Guo

A dissertation submitted in partial fulfillment
of the requirements for the degree of
Doctor of Philosophy
(Electrical Engineering)
in The University of Michigan
2010

Doctoral Committee:

Professor Theodore B. Norris, Chair
Professor James R. Baker, Jr.
Professor Duncan G. Steel
Assistant Professor Jingyong Ye, University of Texas at San Antonio

To my wife Yuwei

Acknowledgements

When I first came to the University of Michigan, I asked myself what I would learn during my Ph.D. study. Five years later, I am happy that I have found my interest and passion in an interdisciplinary area, biophotonics, and have done some interesting work here. I also feel very privileged to express my gratitude for all the help, input and advice I received from many colleagues and friends without whom this thesis would not have been possible.

First and foremost, I would like to thank my mentor Dr. Theodore Norris for his guidance, inspiration, support, and patience during my Ph.D. study. Ted never pushed me on my research projects, allowed me great freedom to work independently and to initiate projects, and encouraged me to work with my own imagination and creativity. Meanwhile, he guided, criticized, and provided any support I needed. I am immensely grateful for his advice, support and perpetual optimism during my graduate time.

I am also indebted to Dr. James R. Baker, Jr., who has been one of my advisors and who guided my work in weekly group meetings. I am very impressed that he always could give explanations on my biomolecular experimental results and lead me to the right direction. Without his academic excellence and continuous encouragement, I could not imagine my work on biomolecular detections could have become such a success.

I would especially like to thank Dr. Duncan Steel, who is a great professor to whom I cannot over-express my appreciation. Since I joined the degree program, he has kept helping me all the way: giving me suggestions on courses selection, teaching me quantum mechanics, and serving as a member of my qualifying examination, prelim and defense committees. He is always nice to students and has been a tremendous role model for me.

I would like to give special thanks to Dr. Jingyong Ye, who has given me great support and guidance on both research and life during my early graduate years. I also appreciate him much for his time serving on my Ph.D. committee and his efforts to assist in this endeavor even after he left for Texas.

The University of Michigan has provided a fertile and cooperative environment for research. I am grateful to Dr. Lingjie Jay Guo, who has been always welcome to my visits and has given me his continuous support and suggestions on various projects. My appreciation also goes to Dr. Fred Terry for his help on spectroscopic ellipsometry measurement, Dr. Nils Walter for fruitful discussion on total internal reflection fluorescence microscopy (TIRFM), Dr. Mark Banaszak Holl for his suggestion on surface chemistry, Dr. Tom Bersano for his help on PDMS channel fabrication, and Dr. James Deane and Matthew Bell for their help on patent application. I also would like to thank Dr. Ovidiu Toader and Dr. Fabian Naab, who provided me a comfortable, convenient and supportive working environment on thin film fabrication.

I am extremely thankful to my fellow research group members for the often helpful, usually entertaining discussions we've had: Chuck Divin, Noah Chang, Dong Sun, Yu-Chung Chang, Malakeh Musheinish, Jessica Ames, Eric Tkaczyk, Moussa Ngom, Hyunyong Choi, Pacha Mongkolwongrojn, and Momchil Mihnev. In particular, I'm deeply indebted to Chuck for his help during my graduate time. Chuck provided great help and numerous suggestions on my experimental setup, LabVIEW programming, data interpretations, and thesis writing. Without him, I can hardly imagine my thesis work being accomplished so smoothly and comprehensively. I'd like to wish he could achieve great success in prototyping our biosensor. I also greatly appreciate Noah's valuable help on my research and life during my early years.

I feel extremely lucky that I had a chance to be part of MNIMBS and got various help from Baohua Huang, Thommey Thomas, Pascale Leroueil, Nicholas Mank, Dan McNerny, Ming-Hsin Li, Alina Kotlyar, Andrzej Myc, Seok-Ki Choi, Yuehua Zhang, Shengzhuang Tang and Istvan Majoros, as well as from Patricia Gold, Claire Verwejj and Gloria Lippens. I'd like to thank Baohua for his expert guidance on surface chemistry, which solved one of the biggest problems in my thesis work. I especially thank Ms. Patricia Gold, who generously contributed plenty of time to proofread this thesis and encouraged me a lot during my thesis writing.

I would also like to thank Sung-Liang Chen, Hyoung Won Baac, Carlos Alberto Pina, Yi-Kuei Wu and Tao Ling from Dr. Jay Guo's group, for their collaboration and help on

ultrasound experiments and device fabrication; I thank Nicole Michelotti and Tony Manzo from Dr. Nils Walter's group, for their suggestion on TIRFM.

The CUOS has provided a second-to-none environment for my research. I would like to extend my thanks to CUOS staff members: Linda Owens, Bett Weston, and Debra Dieterle, as well as Beth Stalnaker from the EE graduate program.

I sincerely thank my English teachers Elizabeth Axelson, Brenda Imber, Roann Altman, and Merle Brenner for their help. I also want to thank my friends and colleagues: Yang Hou, Chenan Xia, Yun Zhou, Meng Cui, Tsai-Wei Wu, Chi-Hung Liu, Jun Yang, Ching-Wei Chang, Wei-Zung Chang, Bing Liu, Xu Chen, Haixiong Wang, Li Xu, Nengfeng Zhou, and many others, for their help and friendship.

Finally, I would like to thank my parents, sister and brother. Although I have been working in a field so foreign to them, their selfless love and endless support are the continuous spring for me to face challenges and to move forward. I am also deeply grateful to my uncle Zhenhua Liu and my aunt Yuehua Liu, who have supported me to pursue my dream here and have taken care of me all of the time.

Most importantly, I would like to thank my wife Yuwei for her love, encouragement, support and patience. For the past five years, I have had the joy and privilege to share all of my successes and all of my fears with her. Without her support, nothing would have ever been possible.

Table of Contents

List of Figures

List of Tables

Abstract

Sensitive, Label-free Biomolecular Binding Detection Using a One-dimensional Photonic Crystal Sensor

by

Yunbo Guo

Chair: Theodore B. Norris

Novel optical methods for performing label-free detection have attracted growing attention driven by increasing demands for better understanding of specific interactions between biomolecules, which provide a chemical foundation for all cellular processes. Although a number of label-free techniques for directly monitoring biomolecular binding exist, they are limited in their ability to measure the binding kinetics of very small molecules, to detect low concentrations of molecules, or to detect low affinity interactions. In this thesis, I develop a one-dimensional photonic crystal biosensor which enables highly-sensitive, label-free, real-time biomolecular binding analysis.

This sensor uses a one-dimensional photonic crystal (PC) structure in a total-internal-reflection (TIR) geometry (PC-TIR), which forms a high-finesse Fabry-Pérot resonator with an open cavity. Detailed analysis on how to effectively design and fabricate suitable

sensor structures is discussed. Experimentally, the sensor achieved a narrow resonance width (~ 1 nm) and large sensitivity (~ 1840 nm per refractive index unit (RIU)).

By adopting normalized intensity modulation, this sensor demonstrates ultralow detection limits (i.e., high performances) in a series of experiments: 10^{-8} RIU for bulk solvent refractive index, 2×10^{-5} nm for molecular layer thickness, and 6 fg/mm^2 for surface mass density. Moreover, its capability for label-free biomolecular detection is characterized with a standard streptavidin-biotin binding system. The specific binding of biotinylated molecules ranging over three orders of magnitude in molecular weight, including very small molecules (< 250 Da), DNA oligonucleotides, proteins, and antibodies (> 150,000 Da), to streptavidin covalently adsorbed on a sensing surface are detected in real time with high signal-to-noise ratios. Furthermore, it shows high efficiency for quantitative analysis on DNA studies, including strand length measurement, low concentration binding, and hybridization.

Compared to the state-of-the-art surface-plasmon-resonance (SPR)-based biosensors whose performance is mainly restricted by broad resonance widths, the ultrahigh-Q resonant cavities such as whispering gallery modes (WGMs)-based biosensors which suffer from low sensitivity, thermal instability and nontrivial coupling, the PC-TIR sensor employing a simple geometry and a moderate Q, has achieved orders of magnitude higher detection sensitivity than other label-free optical biosensors reported to date, and thus is promising as a new sensing platform for biomolecular binding detection.

Chapter 1

Introduction

1.1 Optical Biosensors

The rapid development of analytical equipment for characterizing molecular interactions has been driven over the last two decades by the increasing demand for a better understanding of the specific interactions among biomolecules, which provide insights into fundamental biological processes and serve as the cornerstones of life science research, pharmaceutical discovery, medical diagnosis, food/water safety assurance, environmental monitoring, and homeland security. This demand is reflected by the market value of approximately $11 billion in 2005, which is growing at an average rate of 8% per year [1]. Quantitative measurement of the binding of an analyte to a target biomolecule and biomolecules in complexes is an essential step in understanding how such molecules interact with each other under physiological conditions, such as whether the analyte interacts with another (i.e., specificity), how strong the binding affinity is between two molecules, and whether a chemical compound will interact with a therapeutic target for cancer within a patient's blood, all of which are of central importance to the discovery and development of new pharmaceuticals [2, 3].

For example, in order to discover a novel therapeutic antibody to treat cancer and other diseases, the screening of a large repertoire of antibodies is necessary in order to identify high specificity and high affinity binders, followed by a more detailed characterization of the binding properties and the determination of epitope specificity. However, the development of technology to identify such binding is challenging because of the characteristics of biomolecular analytes, such as drug compounds (often with molecular weights of 500 Daltons or below), DNA oligonucleotides, lipids, peptides, enzymes, antibodies, and viral particles. These molecules are exceedingly small or

diversified and are sometimes present within a test sample at concentrations in the *fM* to *nM* concentration range in solutions that also simultaneously contain thousands of other molecules at concentrations that are orders of magnitude greater. Sensitive, specific, accurate and high throughput analytical instruments that can provide insights into these critical biological processes are in high demand.

With the advantages of robustness, simplicity and high sensitivity, optical biosensors have attracted significant attention and have become mainstream research tools for biomolecular detection [4-6]. Generally, there are two detection protocols that can be implemented in optical biosensing: fluorescence-based detection and label-free detection. In fluorescence-based detection, either target molecules or biorecognition molecules are labeled with fluorescent tags, and the emitted fluorescence at a particular wavelength acts as a surrogate to indicate the presence of the target molecules to determine the interaction strength between the target and biorecognition molecules. Fluorescence spectroscopies include the measurements of fluorescence intensity, decay time, polarization, energy transfer, quenching efficiency, etc. [7] Though fluorescence-based optical detection has been central to implementing nearly all biochemical and cell-based assays with extremely high sensitivity [8, 9], the labels themselves pose several potential problems. For example, there must be prior knowledge of the target's presence and the target molecule must be modified to incorporate the label. This is a laborious process and may alter or inhibit the functionality of the molecules under study. Moreover, quantitative analysis is challenging due to the unpredictability of the fluorescence efficiency and the inability to acquire kinetics information from an assay [10].

In contrast, there are many methods that allow direct detection of biological analytes without labels. They generally measure some physical properties of the analytes, such as mass, volume, polarization, dielectric permittivity, and conductivity, using an appropriate sensor. The sensor functions as a transducer that can convert one of these physical properties (such as the mass of a substance deposited on the sensing surface) into a quantifiable signal that can be measured by an instrument (such as a current or voltage proportional to the deposited mass). Label-free based detection measures the analytes in

their natural forms and removes the problems of fluorescence labels, allowing for accurate, quantitative and kinetic measurement of biomolecular interactions [11-13].

Most label-free optical sensors utilize evanescent waves to probe the presence of analytes at the sensor surface or in the surrounding medium by detecting the effective index change within an evanescent field [14]. The evanescent field intensity decays exponentially from the sensing surface, with a decay length of 100 ~ 200 nm into the test sample. Therefore, for those analytes that are far away from the sensor surface and thus do not efficiently interact with the evanescent field, the sensing signal decreases significantly. One key to high sensitivity sensor design is to match the regions of greatest biomolecular binding to those regions with the highest evanescent field intensity.

1.2 Main Performance Characteristics

There are many parameters to consider in evaluating the performance of biosensors, including sensitivity, resolution (or detection limit), dynamic range, throughput, sensor cost, ease of use, robustness, and others [13]. These are different parameters, but they are also related to each other. In this section, we define some of the main parameters used to compare the performance of optical biosensors.

1.2.1 Sensitivity

Sensor sensitivity is an important parameter in evaluating a sensor's performance. Sensitivity is defined as the ratio of the change in sensor output response to the change in the quantity to be measured (e.g., the analyte mass density on the sensing surface). The mass density change is usually assumed to be directly proportional to the change in the effective thickness or the effective refractive index. The expressions of the sensor's sensitivity depend on the detected change (the thickness or refractive index) and the detection methods (the angle, wavelength, intensity, or phase). For example, in section 2.4.4, the sensitivity using intensity modulation depends on two figures of merit: the conversion efficiency of the resonant wavelength shift to the change of the intensity I_r (the optical sensitivity) and the conversion efficiency of the biomolecular binding (a change in the effective thickness d_{ad}) to the resonant wavelength shift λ_R (the binding sensitivity).

$$S = \frac{\partial I_r}{\partial d_{ad}} = \frac{\partial I_r}{\partial \lambda_R} \cdot \frac{\partial \lambda_R}{\partial d_{ad}} \qquad (1.1)$$

In section 4.3.3, we discuss the bulk solvent refractive index sensitivity S_{sol} using a wavelength modulation which is the ratio of the resonance wavelength shift λ_R to the change of the bulk solvent refractive index n_t:

$$S_{sol} = \frac{\partial \lambda_R}{\partial n_t} \qquad (1.2).$$

For optical sensors, sensitivity is fundamentally determined by how efficiently the electromagnetic field interacts with biomolecules bound on the sensor surface or simply by the fraction of light in the solution or by the light intensity at the sensor surface [15]. So the bulk solvent refractive index sensitivity in the units of nm per refractive index unit (*nm/RIU*) reflects the fraction of light in the solution and enables a rough comparison of the sensing capability among different optical technologies and structures.

The sensitivity of an optical biosensor can be characterized in a number of ways, depending on the applications and detection methods. However, an important and inherent comparative parameter of sensing devices is the figure of merit (FOM) [16]

$$FOM = \frac{S_{sol}}{\Delta\lambda} \qquad (1.3)$$

where $\Delta\lambda$ is the full-width of the resonant dip at half-maximum, and S_{sol} is defined in Equation 1.2.

1.2.2 Resolution (or detection limit)

Resolution is another important parameter to consider in characterizing a sensor's performance. Sensitivity refers to the magnitude of a sensor's response to a given change in analytes on the sensor surface, and resolution refers to the smallest change in analytes that can be measured. To determine the resolution of a sensor, one must characterize the noise of the sensor, which can be easily obtained by measuring the signal output at a steady-state condition (e.g., as in section 4.2.2). The noise is thus defined as the standard deviation σ of the measurements. If we define a signal to be detectable when the signal has a magnitude of σ, then the smallest measurable analyte change of the sensor is the detection limit (DL), with the expression written as:

$$DL = \frac{\sigma}{S} \qquad (1.4)$$

where S is the sensor sensitivity.

Similarly, the detection limit can be specified in different ways according to the measurable changes on the sensor surface. First, most of the optical sensors are sensitive to a refractive index (RI) change in the bulk solution, and the detection limit in units of *RIU* can be used to compare the sensor capability (e.g., as in section 4.3.3).

The second is to use the surface mass density in units of pg/mm^2, which is what a biosensor actually measures. It is an especially critical performance criterion for detection of analytes present at low concentration or detection of adsorbed molecules with low molecular weight. However, the surface mass density is experimentally difficult to determine, and it is usually obtained by relating it to the effective refractive index or thickness that could be measured experimentally (e.g., as in section 4.3.5).

The third way to measure interaction is to use the analyte concentration or thickness (in units of *pg/mL* or molarity or *nm*), which is useful and easy to determine in experiments. However, a detection limit defined in this manner needs to be specified for each type of a biomolecule, as it depends on the target molecule and its affinity to the biorecognition molecule on the sensor surface (e.g., as shown in section 5.5.6 using *pM* and in section 4.3.4 using *nm*).

Obviously, an improvement in the detection limit can be achieved by increasing the sensor's sensitivity or reducing the noise level. Sensitivity can be enhanced by increasing the interaction between light and the biomolecules [14]. Factors causing noise include temperature fluctuations, light source intensity instability, nonspecific binding, etc. In section 4.2.2, we have a detailed discussion on how to effectively reduce the sensor noise and thus improve the detection limit.

Sensitivity and detection limit are two important parameters to use in characterizing the performance of the optical sensors, and they can be defined numerically. Other parameters such as ease of use or instrument robustness are subjective but can have a significant impact on the commercial success of an optical sensor.

1.3 Motivation

Label-free optical sensing platforms based on surface plasmon resonance, interferometry, optical waveguides or optical fibers, ring resonators and photonic crystals, as well as many others, have been investigated. An optical label-free sensor may involve two or more of the optical structures mentioned above to enhance its sensing performance. Review articles and books focusing on these label-free optical biosensors or commercial systems can be found in the references [11], [12], [13], and more. In this section, I mainly talk about the motivation behind the dissertation research work.

Currently the most widely used technology for label-free binding analysis is surface plasmon resonance (SPR) [6, 17-19]. As Figure 1.1 shows, the SPR sensor detects the binding of analytes to ligands immobilized on a continuous metal (gold or silver) surface in a total-internal-reflection geometry. The excited surface plasmon modes are very sensitive to the influence of bound molecules on the refractive index of the dielectric medium adjacent to the metal film, with a sensitivity exceeding 10^3 nm per refractive index unit (RIU). However, owing to large absorption in the metal film, the SPR resonance mode is broad (a few tens of nm), which restricts its detection sensitivity and precludes its use for applications that require detection of small molecules or low surface coverage of bound molecules [17]. Although sophisticated engineering has improved the performance of commercial SPR-based systems, such as the Biacore S51 which shows a detection limit of 0.5 pg/mm^2 for small molecule binding [20], inherently improving the sensor's sensitivity is still the key to further advances [16].

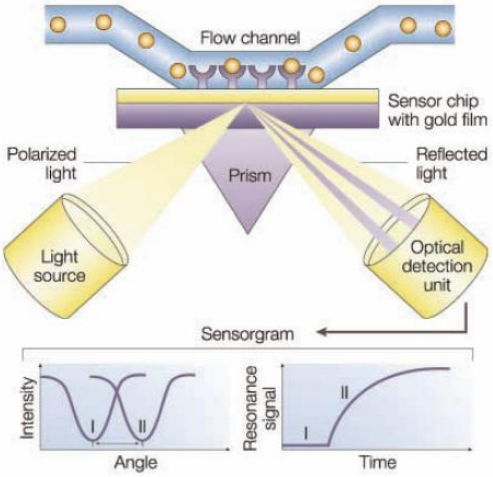

Figure 1.1 Typical set-up of an SPR biosensor. The SPR detects changes in the refractive index in the immediate vicinity of the surface layer of a sensor chip. SPR is observed as a sharp shadow in the reflected light from the surface at an angle that is dependent on the mass of material at the surface. The SPR angle shifts (from I to II in the lower left-hand diagram) when biomolecules bind to the surface and change the mass of the surface layer. This change in resonant angle can be monitored non-invasively in real time as a plot of the resonance signal (proportional to mass change) versus time (from Cooper [4]).

One key to obtaining higher sensitivity is to narrow the optical resonance to below that exhibited by classical surface plasmon resonances. As Figure 1.2 shows, an optical microring resonator based on whispering gallery modes (WGMs) has recently been under intensive investigation as an emerging sensing technology [21-24]. The WGM has the evanescent field present at the ring resonator surface and responds to the binding of biomolecules. In contrast to the straight waveguide, the effective light-analyte interaction length of a ring resonator sensor is no longer determined by the sensor's physical size but rather by the number of revolutions of the light supported by the resonator, which is characterized by the resonator quality factor Q. Ring resonators using WGMs exhibit ultrahigh Q values ($> 10^6$) and extremely narrow resonances (< 1 pm), enabling very high detection resolution [21-23]. However, a problem with ultrahigh-Q resonators is that the light is tightly confined by the resonator and only a very small portion of the optical mode interacts with the analyte solution; this leads to a relatively low sensitivity (a few nm/RIU) and thus restricts the detection limit [15]. In addition, ultrahigh-Q resonators generally suffer thermal instability [25] and have difficulties with consistency between experiments arising from coupling light into and out of the resonators.

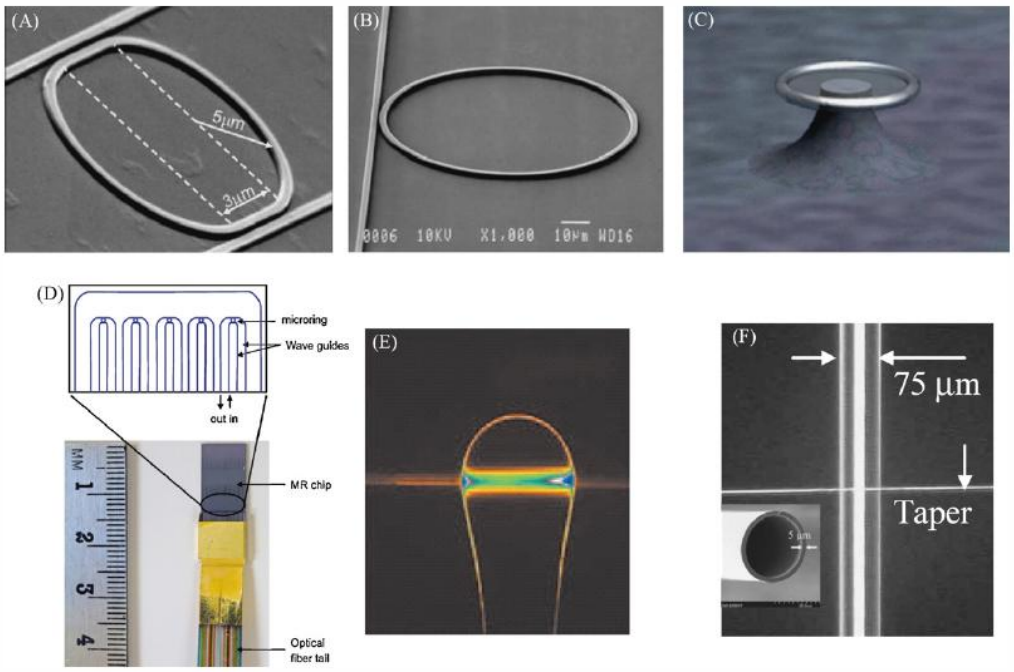

Figure 1.2 Various ring resonator biosensors. (A) Silicon-on-insulator ring resonator; (B) Polymer ring resonator; (C) Microtoroid; (D) Glass ring resonator array; (E) Microsphere; (F) Capillary-based opto-fluidic ring resonator (OFRR) (from Fan et. al. [11]).

Another way to obtain higher sensitivity is to increase the sensor sensing surface area, as the response of a biosensor depends on the interaction of the analyte with the ligand immobilized on the sensing surface [26, 27]. As Figure 1.3 shows, the SPR-based sensors (and others with a planar surface) only have a two-dimensional biosensing surface, but nanoporous silicon-based sensors use a three-dimensional biosensing surface and serve as host to a far greater number of molecules than can be accommodated on a planar, solid surface, which greatly improves the sensing surface-to-volume ratio (a few hundred square meters per cubic centimeter) and thus the detection sensitivity. With this significant advantage as well as fast fabrication and diverse and tunable optical properties, porous silicon sensors with different designs, such as single or double thin layers, waveguides, Bragg mirrors, rugate filters, and microcavities have been intensively investigated [26-32]. However, one of the big disadvantages is that it is challenging to measure real-time binding kinetics due to the slow diffusion of biomolecules into the sub-micron pores.

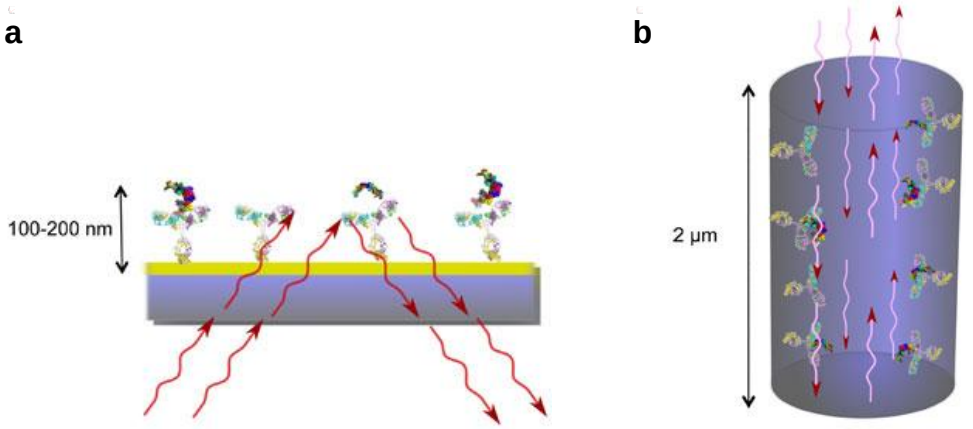

Figure 1.3 Comparison between 2-D and 3-D biosurfaces. (a) 2-D biosurface: sensing light passes through fewer biolayers; (b) nanoporous silicon 3-D biosurface: sensing light passes through many biolayers (from Silicon Kinetics [32]).

Given the properties of ultralow-Q resonators (i.e., SPR-based sensors with broad resonance but large sensitivity), ultrahigh-Q resonators (i.e., WGM-based sensors with narrow resonance but low sensitivity), and porous structure-based sensors with a large sensing area but slow diffusion time, we focus our attention on simple one-dimensional photonic crystal (1-D PC) structures (i.e., alternating pairs of dielectric layers). Compared to complicated 2-D PC structure-based sensors [33-35]or photonic crystal fibers [36], 1-D PC structures are simpler and easier to control in that the Q value can be easily adjusted by varying the number of alternating pairs [31, 37-39]. The periodicity of the PC structure forms a 1-D photonic bandgap, such that a range of wavelengths is not allowed to propagate within the structure. By introducing "defects" into the PC layer structure at an appropriate position, the electric field can be confined and enhanced in the vicinity of the sensing area where target analytes are adsorbed.

In this dissertation, I describe our efforts to develop a novel optical sensor using a 1-D PC structure in a total internal reflection (TIR) geometry (a PC-TIR sensor) [40-42]. As discussed in section 2.4, this PC-TIR sensor functions as a Fabry-Pérot resonator, yielding a much sharper resonance (~ 1 nm) than the SPR sensor but still with large sensitivity (~ 1840 nm/RIU). Moreover, it has an open sensing surface available for analyte binding and allows label-free, real-time binding measurements. This configuration possesses the advantages of evanescent-field-based optical resonators

without the light-coupling problems [14], and the properties of the PC structures make it easy to be designed and engineered to operate at any desired optical wavelength and to detect analytes over a large dynamic range.

1.4 Dissertation Outline

In Chapter 2, I derive an effective transfer matrix method to simulate multiple dielectric layers structure at arbitrary angles and polarizations. The underlying and operating principles of the PC-TIR sensor are investigated. Then I discuss how to characterize the resonance mode, how to effectively monitor the resonance shift, and how to derive the sensor's sensitivity. The effects of the structure parameters and the incident light properties on the sensor's sensitivity are comprehensively investigated and analyzed via simulations.

In Chapter 3, I propose a design criterion to make a suitable PC-TIR sensor structure. Three coatings of 1-D PC structures with different light confinement abilities and their corresponding PC-TIR structures are fabricated, tested and analyzed.

In Chapter 4, an integrated experimental system combining the white light spectra measurement and the normalized intensity measurement is built. The sensor noise is characterized and analyzed. Moreover, I explore the optical properties of the PC-TIR biosensor and experimentally characterize its sensitivity regarding bulk solvent refractive index change, thin molecular films adsorption, and real-time analyte binding. Finally the performances of the PC-TIR biosensor and the SPR-based biosensor are compared.

In Chapter 5, I make a systematic investigation into the PC-TIR sensor's capability for label-free biomolecular binding detection, including sensitivity characterization, surface functionalization, binding experiments design and execution, and results analysis. The specific binding of biotinylated analyte molecules (antibodies, proteins, DNA oligonucleotides and D-Biotin) are investigated in detail. Moreover, I also perform quantitative analysis on DNA studies, including strand length measurement, low concentration DNA oligonucleotide binding, and DNA hybridization.

Contributions and further developments are presented in Chapter 6.

Chapter 2

Principle and Simulation of a PC-TIR Structure

2.1 Introduction

A One-dimensional photonic crystal (1-D PC) in the form of a periodic multilayer dielectric stack (such as the Bragg mirror) is the simplest photonic crystal structure. It affects the propagation of electromagnetic waves in a spectral range by defining one-dimensional allowed and forbidden photonic bands. Due to its simplicity in fabrication, the 1-D PC has been studied extensively and used in a diverse range of applications, including highly reflective mirrors, omnidirectional reflectors [43], and nonlinear optical diodes [44]. When a structural defect is introduced in the 1-D PC, a photon-localized state can be created in the photonic band gap and the electrical field around the defect can be confined and enhanced. Control of defect modes by PC structures is becoming a key technology for many new photonic devices, such as photonic crystal fibers [36], low-threshold optical switching [45], and optical biosensors [37-42].

A major topic of this dissertation is how to effectively control the defect mode of a 1-D PC structure to create a highly sensitive biosensor (PC-TIR sensor). In this chapter, I first introduce an effective transfer matrix method to simulate the sensor structure; then explore the principle of the PC-TIR sensor and discuss effective methods for monitoring the resonance mode shift and derive the detection sensitivity; finally I analyze the effects of the structure parameters and the incident light properties on the sensitivity of the PC-TIR sensor.

2.2 Transfer Matrix Method

There are many ways developed to calculate the transmission, reflection and absorption spectra of multilayer structures, including analytical solutions [43, 46], the

transfer matrix method [47-49], the scattering matrix method [50], and the Kronig-Penney model [51]. The principal simulation method adopted in this dissertation is the transfer matrix method, which is easy to derive and can also calculate each component of the electromagnetic field within the multilayer structure.

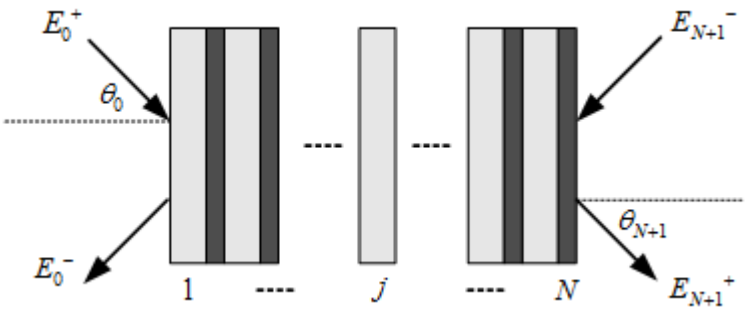

Figure 2.1 Schematic diagram of a multilayer structure.

Figure 2.1 shows the schematic diagram of a multilayer structure. In order to connect the output field ($E_{N+1}{}^+$, $E_{N+1}{}^-$) with the input field ($E_0{}^+$, $E_0{}^-$), a series of matrices must be obtained, including each interface matrix $M_{i,j}$ between two medium layers (i and j) and each propagation matrix M_j connecting the beginning and the end within the layer j. The total transfer matrix can be achieved by simply multiplying all the interface and propagation transfer matrices as follows:

$$\begin{bmatrix} E_{N+1}{}^+ \\ E_{N+1}{}^- \end{bmatrix} = M_{N,N+1} M_N M_{N-1,N} \cdots M_{j,j+1} M_j M_{j-1,j} \cdots M_{1,2} M_1 M_{0,1} \begin{bmatrix} E_0{}^+ \\ E_0{}^- \end{bmatrix} \qquad (2.1).$$

2.2.1 Interface matrix

The interface matrix of two different media can be derived from the boundary conditions of Maxwell's equations:

$$\begin{cases} \vec{E}_i^{\parallel} = \vec{E}_j^{\parallel} \\ \vec{H}_i^{\parallel} - \vec{H}_j^{\parallel} = \alpha \\ \vec{D}_i^{\perp} - \vec{D}_j^{\perp} = \sigma \\ \vec{B}_i^{\perp} = \vec{B}_j^{\perp} \end{cases} \qquad (2.2)$$

where α and σ are the free current density and free change on the interface between medium i and medium j, respectively. The superscripts ∥ and ⊥ stand for the components of the field parallel and perpendicular to the interface.

For a special case where there is no free charge or current, the tangential components of E and H and the normal components of D and B must be continuous across the interface. The interface matrix is related to the polarization and incident angle of the electromagnetic waves. It is the same for transverse electric (TE) and transverse magnetic (TM) polarization at a normal incidence, but different at an oblique incidence. In the following, I will derive the interface matrix for TE and TM polarizations separately.

A. The interface matrix for TE polarization

Figure 2.2 shows the interface between medium i and medium j for TE polarization light. Assuming $E_i^+$and E_i^- are the incident forward and reflected waves, and $E_j^+$and E_j^- are the transmitted and backward propagating waves. H_i^+, H_i^-, H_j^+ and H_j^- are the corresponding magnetic fields defined similarly, k_i^+, k_i^-, k_j^+, and k_j^- are the corresponding propagation constants, and θ_i, θ_j are the incident angles in medium i and medium j.

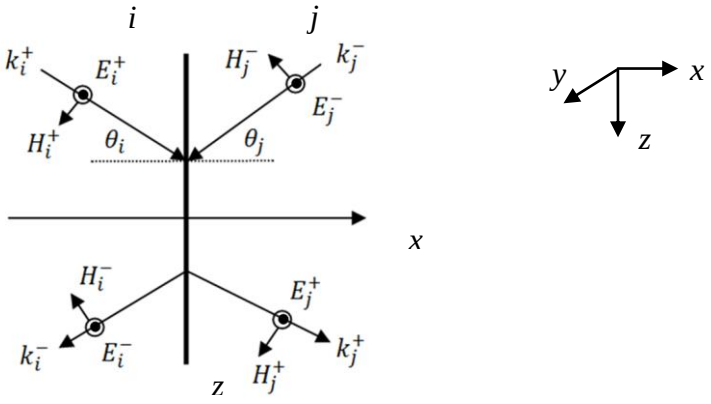

Figure 2.2 Schematic diagram of the interface for TE polarization.

Since $\vec{D}_i^{\perp} = \vec{D}_j^{\perp} = 0$ automatically holds, the boundary conditions in Equation 2.2 become

$$\begin{cases} E_i^+ + E_i^- = E_j^+ + E_j^- \\ (H_i^+ - H_i^-)cos\theta_i = (H_j^+ - H_j^-)cos\theta_j \\ (H_i^+ + H_i^-)sin\theta_i = (H_j^+ + H_j^-)sin\theta_j \end{cases} \tag{2.3}$$

where $H = \sqrt{\frac{\varepsilon}{\mu}}E$, $\varepsilon = \varepsilon_0\varepsilon_r$, and $\mu = \mu_0\mu_r$ and where ε and μ are the permittivity and the magnetic permeability of the medium, ε_0 and μ_0 are the free-space permittivity and permeability, and ε_r , μ_r are the relative permittivity (dielectric constant) and relative permeability of the medium. For non-magnetic and homogenous media, which commonly constitute optical layers, $\mu_r = 1$ and $\varepsilon_r = {n_r}^2$, where n_r is the refractive index of the medium.

Since the first and third expressions in Equation (2.3) duplicate the Snell's law, the boundary conditions of the interface become

$$\begin{cases} E_i^+ + E_i^- = E_j^+ + E_j^- \\ (E_i^+ - E_i^-)\eta_i = (E_j^+ - E_j^-)\eta_j \end{cases} \qquad (2.4)$$

where $\eta_p = \sqrt{\frac{\varepsilon_p}{\mu_p}}cos\theta_p = \frac{n_p}{Z_0}cos\theta_p$ (p= i, j), and $Z_0 = \sqrt{\frac{\mu_0}{\varepsilon_0}}$, the free space impedance.

Solving Equation 2.4, I find the interface matrix for TE polarization as follows:

$$\begin{bmatrix} E_j^+ \\ E_j^- \end{bmatrix} = {M_{i,j}}^{TE} \begin{bmatrix} E_i^+ \\ E_i^- \end{bmatrix} = \frac{1}{2}\begin{bmatrix} 1+\frac{\eta_i}{\eta_j} & 1-\frac{\eta_i}{\eta_j} \\ 1-\frac{\eta_i}{\eta_j} & 1+\frac{\eta_i}{\eta_j} \end{bmatrix} \begin{bmatrix} E_i^+ \\ E_i^- \end{bmatrix} \qquad (2.5).$$

B. The interface matrix for TM polarization

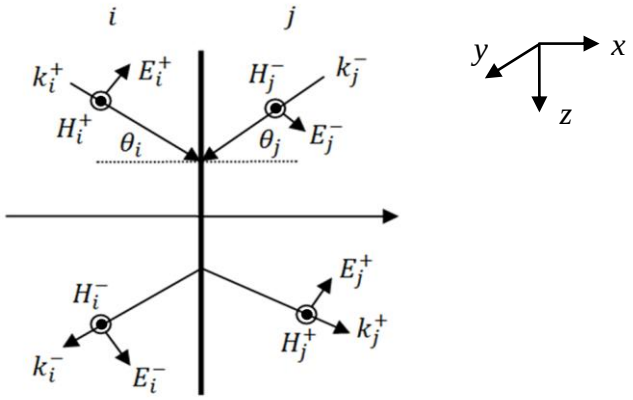

Figure 2.3 Schematic diagram of the interface for TM polarization.

Figure 2.3 shows the interface between medium *i* and medium *j* for TM polarization light. Similarly, since $\vec{B}_i^{\perp} = \vec{B}_j^{\perp} = 0$ automatically holds and one more boundary condition (on the perpendicular components of *D*) duplicates Snell's law, the boundary conditions of the interface for TM polarization can be derived from Equation 2.2 as follows:

$$\begin{cases} H_i^+ + H_i^- = H_j^+ + H_j^- \\ (E_i^+ - E_i^-)cos\theta_i = (E_j^+ - E_j^-)cos\theta_j \end{cases} \quad (2.6).$$

Defining $\eta_p = \sqrt{\frac{\varepsilon_p}{\mu_p}}/cos\theta_p = \frac{n_p}{Z_0}/cos\theta_p$ (p= i, j), the interface matrix for TM polarization can thus be expressed:

$$\begin{bmatrix} E_j^+ \\ E_j^- \end{bmatrix} = M_{i,j}{}^{TM} \begin{bmatrix} E_i^+ \\ E_i^- \end{bmatrix} = \frac{1}{2}\frac{n_i}{n_j} \begin{bmatrix} 1+\frac{\eta_j}{\eta_i} & 1-\frac{\eta_j}{\eta_i} \\ 1-\frac{\eta_j}{\eta_i} & 1+\frac{\eta_j}{\eta_i} \end{bmatrix} \begin{bmatrix} E_i^+ \\ E_i^- \end{bmatrix} \quad (2.7).$$

2.2.2 Layer matrix

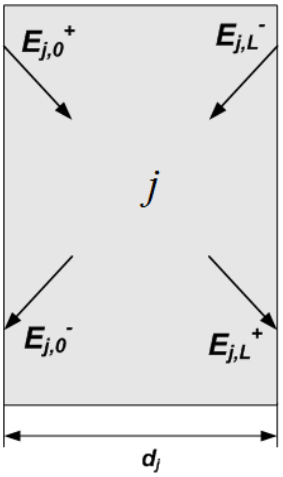

Figure 2.4 Schematic diagram of the layer *j*.

When the electric field propagates through layer *j*, the field at the end of the layer is related to the beginning of the layer by a layer matrix (the same is true for TE and TM polarization):

$$\begin{bmatrix} E_{j,L}{}^{+} \\ E_{j,L}{}^{-} \end{bmatrix} = M_j \begin{bmatrix} E_{j,0}{}^{+} \\ E_{j,0}{}^{-} \end{bmatrix} = \begin{bmatrix} \exp(i\alpha_j) & 0 \\ 0 & \exp(-i\alpha_j) \end{bmatrix} \begin{bmatrix} E_{j,0}{}^{+} \\ E_{j,0}{}^{-} \end{bmatrix} \qquad (2.8)$$

where $\alpha_j = -\frac{2\pi}{\lambda} n_j d_j cos\theta_j$ and d_j is the thickness of the layer j.

2.2.3 Reflection and transmission

The beauty of the transfer matrix method is that a stack of layers can be represented as a system matrix, M_{total}, which is simply the product of the individual 2×2 interface matrices and layer matrices, as Equation 2.1 shows. It can be simplified as

$$M_{total} = \begin{bmatrix} \mathrm{A} & B \\ C & \mathrm{D} \end{bmatrix} \qquad (2.9);$$

therefore $$\begin{bmatrix} E_{N+1}{}^{+} \\ E_{N+1}{}^{-} \end{bmatrix} = \begin{bmatrix} \mathrm{A} & B \\ C & \mathrm{D} \end{bmatrix} \begin{bmatrix} E_0{}^{+} \\ E_0{}^{-} \end{bmatrix} \qquad (2.10).$$

Assuming there is no backward propagating transmitted electric field, that is $E_{N+1}{}^{-} = 0$, we can derive the transmission T and reflection R from the system transfer matrix to be

$$R = |r|^2, \text{and r} = \frac{E_0{}^{-}}{E_0{}^{+}} = -\frac{C}{D} \qquad (2.11)$$

$$T = |t|^2, \text{and t} = \frac{E_{N+1}{}^{+}}{E_0{}^{+}} = A - \frac{BC}{D} \qquad (2.12).$$

If scattering loss from the surface is neglected, the absorption can be simply expressed as: $A = 1 - R - T$. Thus we get all of the transmission, reflection and absorption directly from the transfer matrix calculation.

2.2.4 Field distribution within a multilayer structure

Assuming the incident electrical field is $E_0{}^{+} = \left|E_0{}^{+}\right| \exp(i\alpha)$ and α is the initial phase of the field, the reflected electrical field $E_0{}^{-}$ can be expressed as $E_0{}^{+} = \left|E_0{}^{+}\right| \exp(i\alpha) r$, where the reflection coefficient r (including both amplitude and phase information) is obtained by the transfer matrix method above (Equation 2.11). With all the information

of the input field, we can further calculate the electromagnetic field of any position within the multilayer structure (as Figure 2.1 shows).

For an arbitrary position *x* within a layer *j*, the electric field can be calculated by the transfer matrix method as follows:

$$\begin{bmatrix} {E_{j,x}}^{+} \\ {E_{j,x}}^{-} \end{bmatrix} = M_{j,x} M_{j-1,j} M_{j-1} \cdots M_1 M_{0,1} \begin{bmatrix} {E_0}^{+} \\ {E_0}^{-} \end{bmatrix} = \begin{bmatrix} \mathrm{A_{j,x}} & \mathrm{B_{j,x}} \\ \mathrm{C_{j,x}} & \mathrm{D_{j,x}} \end{bmatrix} \begin{bmatrix} {E_0}^{+} \\ {E_0}^{-} \end{bmatrix} \quad (2.13)$$

where $M_{j,x} = \begin{bmatrix} \exp(i\alpha_{j,x}) & 0 \\ 0 & \exp(-i\alpha_{j,x}) \end{bmatrix}$, $\alpha_{j,x} = -\frac{2\pi}{\lambda} n_j d_{jx} cos\theta_j$, and d_{jx} is the distance from the previous interface (between *j-1* and *j*) to position *x*.

Therefore, the total electric field at position *x* is

$$E_{j,x} = {E_{j,x}}^{+} + {E_{j,x}}^{-} = (\mathrm{A_{j,x}} + \mathrm{C_{j,x}}){E_0}^{+} + (\mathrm{B_{j,x}} + \mathrm{D_{j,x}}){E_0}^{-} \quad (2.14).$$

The electric field intensity and the magnetic field intensity can be also obtained:

$${I_{j,x}}^{TE} = \left|E_{j,x}\right|^2 \quad (2.15)$$

$${I_{j,x}}^{TM} = \left|\frac{\varepsilon_j}{\mu_j}\right| \left|E_{j,x}\right|^2 \quad (2.16).$$

The calculation of the intensity distribution within the multilayer structure is very helpful to determine the field enhancement and then to design a high-sensitivity sensor, where one key is to match the regions of the greatest biochemical binding to those regions with the highest evanescent field intensity.

2.3 One-dimensional Photonic Crystal

In this section, I use the transfer matrix method derived above to explore the properties of a one-dimensional photonic crystal structure (1-D PC). Figure 2.5 shows the structure used in the simulation. It is composed of N pairs of alternating lower-index layer A and higher-index layer B: substrate / $(BA)^N$/substrate.

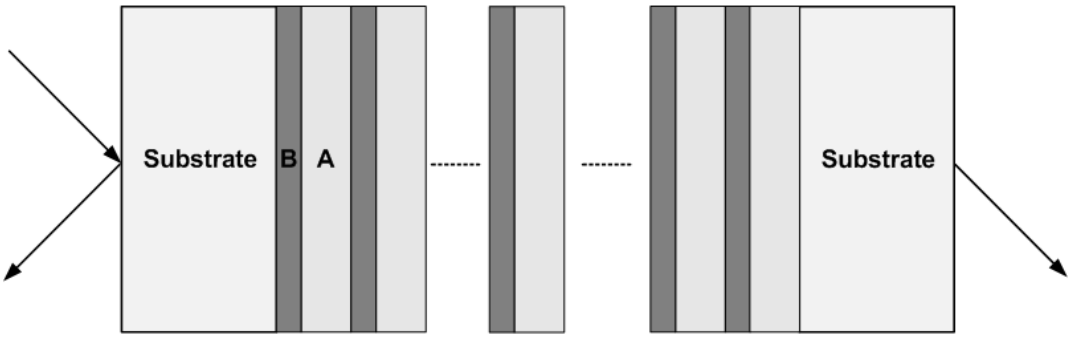

Figure 2.5 Schematic diagram of a 1-D photonic crystal structure.

Assume the incident angle at the substrate layer is θ_s, and the refraction angles in the lower index layer and higher index layer are θ_s, θ_A, and θ_B, respectively. Let n_s, n_a, and n_b be the refractive indices of the substrate, lower index layer, and higher index layer, respectively. According to Snell's law,

$$n_s sin\theta_S = n_a sin\theta_A = n_b sin\theta_B \qquad (2.17)$$

In order to form a 1-D photonic crystal structure, the thicknesses of the dielectric multilayers should satisfy the quarter wavelength condition:

$$n_a d_a cos\theta_A = n_b d_b cos\theta_B = \lambda_R/4 \qquad (2.18)$$

where λ_R is the resonance wavelength and d_a and d_b represent the physical thickness of the lower and higher index layers A and B, respectively.

For example, at normal incidence, for $\lambda_R = 633$ nm, $n_s = 1.51$, $n_a = 1.45$, $n_b = 2.25$, the thicknesses of the A and B layers come out to be $d_a = 109.1\, nm$ and $d_b = 70.3\, nm$. The reflectance and transmission spectra obtained from the transfer matrix calculation are shown in Figure 2.6 (a) (the same as for the TE and TM modes at normal incidence). A clear photonic bandgap forms in the spectrum range, which can be used as a high-reflectivity mirror. The bandgap width and position change with the incident angle, polarization, the number of alternating layers N, and the index contrast of these two dielectric layers [52].

If there exists a defect layer X, breaking the periodic structure like substrate / B $(AB)^{N/2}$ / X / $(BA)^{N/2}$ B/ substrate, there will appear a defect state (resonance mode) at a certain position in the bandgap. As a matter of fact, the 1-D PC structure with a defect layer can be considered as a Fabry-Pérot cavity, where two 1-D PC structures on each side act as high-reflectivity mirrors and the defect layer as the cavity layer. In order to get a resonance mode at the wavelength λ_R, the thickness of the defect layer has to satisfy the resonance condition of the Fabry-Pérot cavity:

$$\frac{2\pi}{\lambda_R} n_x d_x cos\theta_x = m\pi \qquad (m = 1,2,\dots) \qquad (2.19)$$

where n_x and d_x represent the refractive index and the physical thickness of the defect layer, respectively. θ_x is the refractive angle in the defect layer, which can be derived from Snell's law.

We follow the previous example at normal incidence for $\lambda_R = 633$ nm and $n_x = 1.45$, and the thickness of the defect layer is calculated to be $d_x = 218.2\, nm$ from Equation 2.19. With the transfer matrix method, the reflectance and transmission spectra in Figure 2.6 (b) are simulated and show clear resonance dip and peak at the resonance wavelength 633 nm in the bandgap.

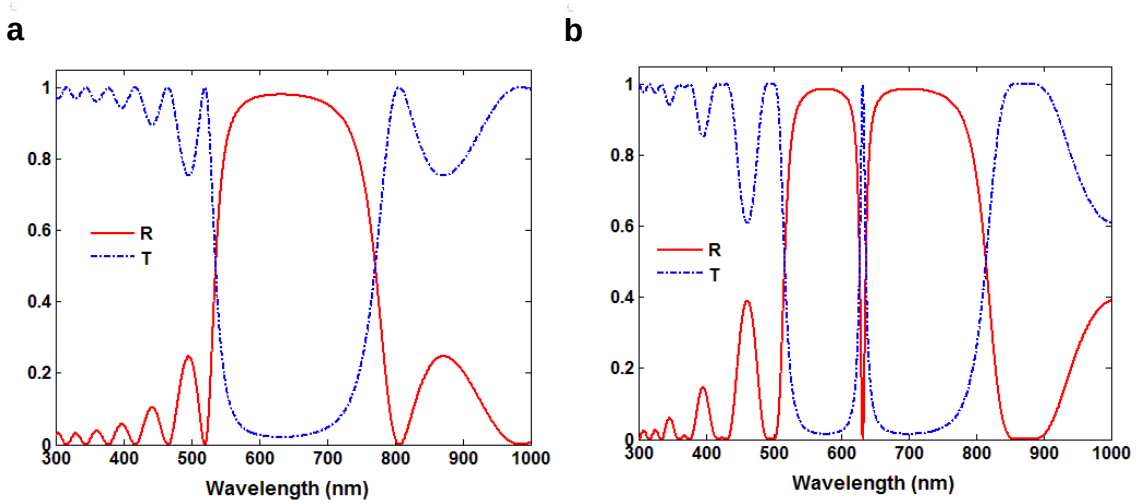

Figure 2.6 The reflectance and transmission spectra showing (a) the photonic band gap without the defect layer and (b) the resonance modes with the defect layer (N=6).

The resonance mode (dip or peak) is sensitive to the thickness or index change of the defect layer. For example, if d_x is changed by 1 nm, the resonance mode shifts by 1.08 nm; if n_x is changed by 10^{-3} refractive index unit (RIU), the resonance mode shifts by 0.17 nm. Therefore, if some analyte could access the defect layer, its adsorption on the defect layer will change the thickness or index–or both–of the defect layer, which can be detected by measuring the shift of the resonance modes. For example, the resonant cavity imaging biosensor made use of two separate 1-D PC structures and a fluidics cavity (defect) layer which could be accessed by analyte molecules for biosensing [53]; a 1-D PC based on a porous silicon structure was also developed, where analyte molecules infiltrating into pores changed the refractive index of the structure and thus shifted the resonance modes [30, 31].

Since the 1-D PC structure with a defect layer can be considered as a Fabry-Pérot cavity, the incident light oscillates in the cavity and the electromagnetic field gets enhanced at resonance, as Figure 2.7 shows. This property can enhance the fluorescence intensity if a fluorophore-doped polymer layer is used as the defect layer [54] or to increase the nonlinear effect if nonlinear material is used as the defect layer [55].

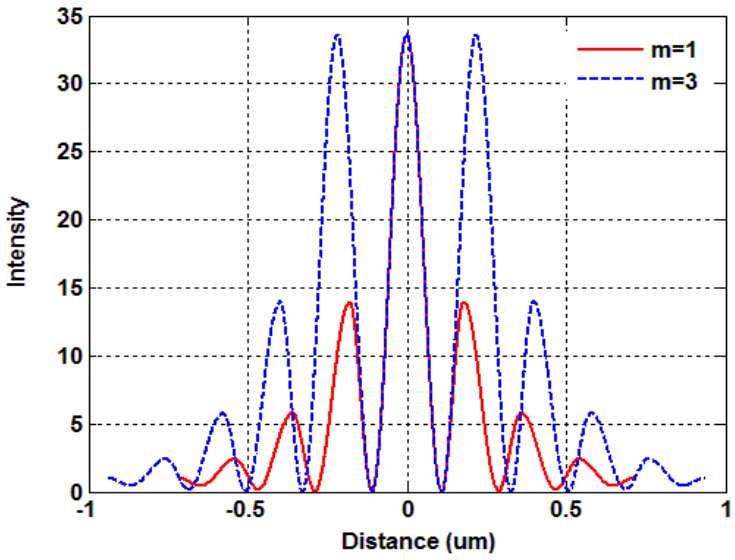

Figure 2.7 Field distribution of the 1-D PC structure with the defect layer (x=0 is the middle of the defect layer; m is the number in Equation 2.19).

2.4 One-dimensional Photonic Crystal in Total Internal Reflection

2.4.1 Introduction

Although a 1-D PC structure has been developed as a biosensor or as an intensity enhancement measurement, its application in these areas is limited. Because the sample of interest is sandwiched inside two pieces of 1-D PC due to the thick substrate (typically a few mm to ensure good surface flatness) and the dielectric layers, the sample is difficult to be accessed by either an objective lens for fluorescence detection or by biomolecules for investigating their interactions.

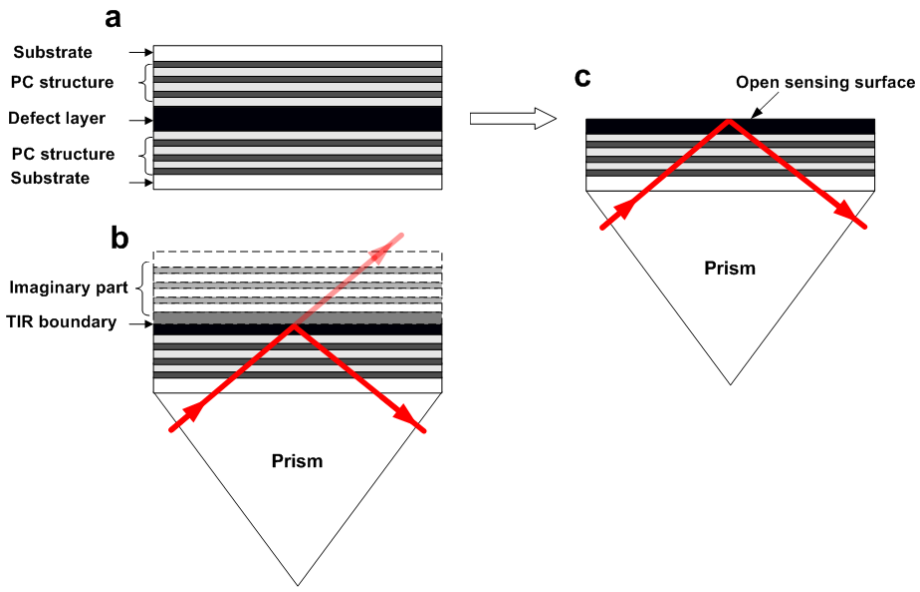

Figure 2.8 Principle of a PC-TIR sensor. (a) A sample sandwiched by two pieces of the PC structure. We conceptually split this structure from the middle layer into two pieces. **(**b) Use of only one piece of the PC structure in a TIR geometry. Owing to the TIR, conceptually an imaginary PC structure exists and forms a microcavity as if there would be two pieces of the PC structure. (c) This PC-TIR sensor offers a unique sensing interface open for targets.

To solve this problem, Ye, et al. [56] proposed a novel configuration, in which a Fabry-Pérot cavity (shown in Figure 2.8a) was conceptually split in half and put in a total-internal-reflection (TIR) geometry (Figure 2.8c). Light is incident through a coupling prism at an angle greater than the angle for TIR. Owing to the TIR, the light propagation may be thought of in terms of an imaginary PC structure (Figure 2.8b), forming a microresonator like the whole 1-D PC structure. In other words, since both the

TIR boundary and a high-reflecting PC structure provide high reflectivity, a new Fabry-Pérot resonator forms in a single defect layer. As shown in Figure 2.9, for light that is resonant with the cavity mode, the optical field will be enhanced near the surface of the defect layer; light outside the photonic bandgap is reflected from the PC layers and has a reduced field amplitude at the surface. Compared to the symmetrical field distribution for a symmetrical structure in Figure 2.7, the field of the 1-D PC structure in TIR geometry (abbreviated as PC-TIR) is asymmetrical, which is quite different. The electromagnetic field still gets its largest enhancement in the defect layer and has a large field on the TIR boundary but decays in the evanescent region.

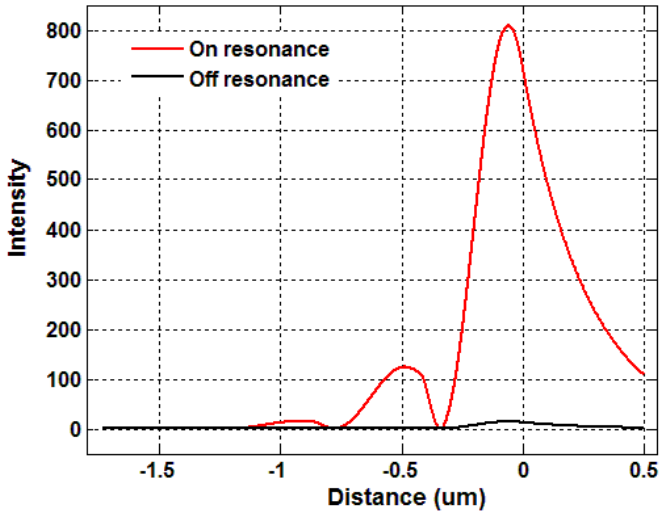

Figure 2.9 Field distributions of the PC-TIR structure when the incident wavelength is on resonance and off resonance (x=0 shows the interface of the defect layer and the surrounding medium).

The unique PC-TIR configuration, with a large enhanced field on the accessible sensing surface, opens up a wide range of applications, such as fluorescence enhancement [57, 58], observation of nonlinear effect [59], electro-optic modulation [60], ultrasound detection [61], etc. In this dissertation, we explore its application in biosensing [40-42, 62], which provides many advantages. First, this PC-TIR sensor functions as a high-finesse Fabry-Pérot resonator, which enables it to yield a sharper resonance mode than SPR-based sensors and thus higher detection sensitivity; and yet the surface available for analyte binding is open to free space and allows real-time binding measurements, bypassing the problems of porous structure-based biosensors. This configuration

possesses the advantages of evanescent field-based optical resonators without light coupling problems, as the cavity Q is not made too large. Moreover, the properties of PC structures make it easy to be designed and engineered to operate at any optical wavelength or incident angle.

In the following sections, I will investigate in detail the optical properties of the PC-TIR sensor and its application in biomolecular detection.

2.4.2 Operating principle of a PC-TIR sensor

The operating principle of a PC-TIR sensor is as follows. The lower-index layer and the higher-index layer consisting of a 1-D PC structure are still designed to form a high-reflectivity mirror, following Equation 2.18, with an incident angle larger than the critical angle for total internal reflection. However, the thickness of the defect layer has a different design because the resonance condition of the PC-TIR changes from Equation 2.19 to Equation 2.20 as follows:

$$2 \cdot \frac{2\pi}{\lambda_R} n_x d_x cos\theta_x + \alpha = (2m+1)\pi \qquad (m = 0,1,2 \ldots) \qquad (2.20)$$

where α represents the Goos-Hänchen phase shift between the defect layer and the surrounding medium. The factor of 2 in the first term on the left hand side is due to the fact that the light double-passes the defect layer, owing to the TIR.

For TE polarization (that is, *s* polarization) of the incident light, the Goos-Hänchen phase shift is given by the following expression:

$$\alpha_s = -2\tan^{-1}\left(\left(\frac{n_S^2 \sin^2\theta_S - n_t^2}{n_x^2 - n_S^2 \sin^2\theta_S}\right)^{1/2}\right) \qquad (2.21)$$

where n_t is the refractive index of the surrounding medium on the defect layer.

For TM-polarization (that is, *p* polarization) of the incident light, the Goos-Hänchen phase shift is given by the following expression:

$$\alpha_P = -2\tan^{-1}\left(\left(\frac{n_x}{n_t}\right)^2 \bullet \left(\frac{n_S^2\sin^2\theta_S - n_t^2}{n_x^2 - n_S^2\sin^2\theta_S}\right)^{1/2}\right) \qquad (2.22).$$

If analyte molecules bind to ligand molecules on the surface of the defect layer, they will give rise to a shift in the cavity resonance, due to the phase shift seen by light propagating in the defect layer and undergoing TIR. Because of the field enhancement near the surface and the high Q of the microcavity, the shift can be very sensitive to molecular binding. Actually two cases are possible here. One is that the refractive index of the molecule layer (adlayer) is so small that TIR happens between the defect layer and the adlayer, and the adlayer will change the effective refractive index of the surrounding medium in the evanescent region, just as in SPR-based sensors [63]; the other is that the refractive index of the adlayer is large enough that TIR occurs between the adlayer and the surrounding medium. The latter case is not limited by the length of the evanescent region (~ 200nm); the resonant mode shifts within a wide bandgap (> 500nm) and thus has a larger detection range than in the first case or with SPR. Since the refractive index of molecules normally is large (~ 1.45) and is close to that of silica commonly made of dielectric layers of the PC structures, in this dissertation, I will focus on the latter case. In addition, the key feature of the PC-TIR sensor is that the surface available for binding is open, thus reducing mass transport limitations. However, as with the SPR sensor, the analytes bound to the sensing surface do not need to absorb the light, and the method is label-free.

The adlayer binding to the sensing surface changes the resonant condition to

$$2\cdot\frac{2\pi}{\lambda_R'}(n_x d_x\cos\theta_x + n_{ad}d_{ad}\cos\theta_{ad}) + \alpha' = (2m+1)\pi \quad (m = 0,1,2,...) \quad (2.23)$$

where n_{ad}, d_{ad}, and θ_{ad} are the refractive index, thickness, and refracted angle of the adlayer, respectively. The symbol λ_R' represents the new resonance wavelength, and α' is the effective Goos-Hänchen phase shift after the adlayer binding [64]. Therefore, by monitoring the shift of the resonance mode, one can detect the properties of binding biomolecules, such as physical thickness, refractive index, mass density, affinity constants, etc.

2.4.3 Characterizing the resonance mode of a PC-TIR sensor

Since the 1-D PC structure is in a total-internal-reflection geometry, all of the incident light is reflected. In order to characterize the resonant mode of the Fabry-Pérot microcavity formed in the defect layer, one can either use phase modulation, which yields insight into the nature of these resonances [60], or modulate reflected light amplitude by an energy loss mechanism [40, 65]. Here we incorporate a small amount of absorption in the defect layer [40]; only light resonant with the microcavity mode is absorbed in this layer, and off-resonant light is totally reflected by the 1-D PC structure. Thus the reflectance spectrum of the total PC-TIR structure will show a pronounced dip at the resonant frequency, the smallest reflectance of which can be engineered to zero by optimizing the absorption in the defect layer, as shown in Figure 2.10.

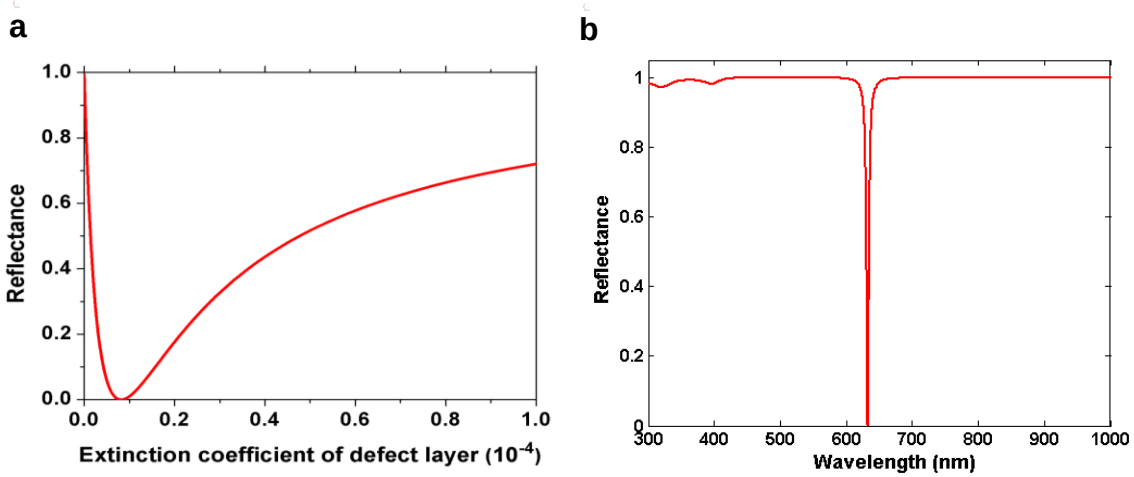

Figure 2.10 (a) The relationship between the minimum reflectance and extinction coefficient of the defect layer; (b) a typical PC-TIR optical spectrum that shows a primary resonance dip at the resonance wavelength.

The absorption needed to get a deep resonance dip is very critical. Neither too much nor too little absorption can achieve a sharp resonance mode. As we are going to discuss in Chapter 3, in addition to intentional absorption in the defect layer, scattering loss on the interface of layers also affects when the 1-D PC structure has strong light confinement.

Similar 1-D PC structures, such as surface electromagnetic waves (SEW) excited in a Kretschmann-like geometry, have also been investigated [38, 65-67]. However, the

principle behind the appearance of the resonance in our PC-TIR structure has some important differences from SEW devices. In the case of the SEW there is a natural mechanism for energy loss via tunneling of localized bulk excitations [65]. This SEW mode in essence comes from the violation of a uniform waveguide system caused by edge effects [68], so the structure is normally an incomplete layer on top of a 1-D PC. The SEW mode is confined in the evanescent region and propagates along the interface, and it is highly sensitive to the incomplete layer, which has been used for sensor applications [38, 66, 67]. In contrast, instead of an incomplete layer without absorption on top of a 1-D PC in the SEW sensor, the resonance mode of our PC-TIR sensor is due to an intentionally inserted absorbing layer in the defect region of the PC structure. There is no surface-propagating wave present. The resonant PC structure defines a wavelength range over which the field is enhanced in the defect region, thus leading to selective absorption and the appearance of a resonance. This approach has a significant advantage in that the absorption can be engineered to yield an optimum resonance – i.e., an extra and highly controllable degree of freedom is available in the design.

2.4.4 Monitoring the shift of the resonance mode

There are usually three types of modulation methods to monitor the resonance mode shift and then to retrieve the information of biomolecular interactions: spectroscopy (angular or wavelength) modulation, intensity modulation, and phase modulation [18]. For an SPR-based biosensor with a broad resonance mode, all of these modulation methods have been widely investigated, but the most common approaches used in high-performance systems are based on angular or wavelength modulation, which is reaching SPR's theoretical detection limit of 10^{-7} RIU [69].

However, the sensitivity of the spectroscopy modulation is limited because the bottom of the resonance mode (a dip or peak) is usually flattened. As Figure 2.11 shows, for a narrower resonance, much higher sensitivity can be obtained by performing an intensity measurement with a single-wavelength laser probe tuned to the steepest fall-off region of the resonance [70-73]. Because of the relative large slope of the fall-off, a minor shift of the resonance mode due to the analyte's binding on the sensing surface can

be transformed into a detectable change in light intensity. Besides the improvement of detection sensitivity or resolution, the intensity modulation also increases throughput, which has been studied in surface-plasmon-resonance imaging systems [18, 73].

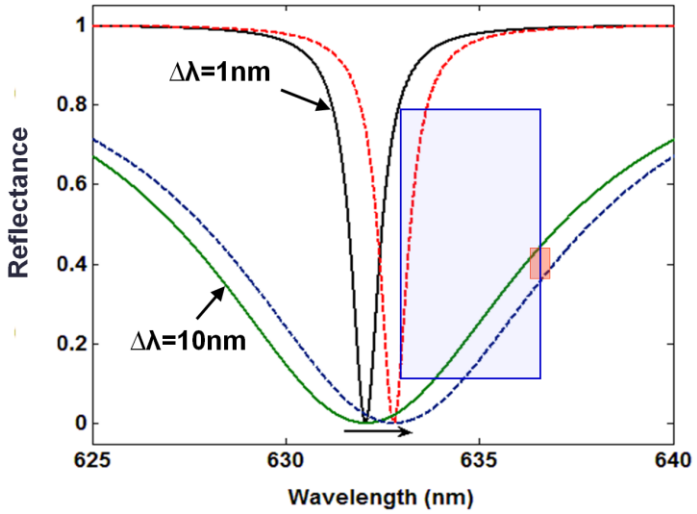

Figure 2.11 Monitoring the shift of a (broad or narrow) resonance mode with the wavelength or intensity modulation method.

The intensity modulation needs high-stabilized and single-wavelength laser sources, such as a Helium-Neon (HeNe) laser. It may be a limitation for very high-Q WGM resonators with extra-narrow resonance, where the high performance is usually achieved using wavelength modulation with a tunable laser source [21]. However, the PC-TIR sensor with a moderate narrow resonance and a tunable working wavelength can greatly benefit from the intensity modulation and achieve the highest possible detection sensitivity.

The overall sensitivity S of the PC-TIR sensor using the intensity detection approach depends on two figures of merit: the conversion efficiency of the resonant wavelength shift to the change of the intensity I_r (optical sensitivity O_s) and the conversion efficiency of molecular binding to the resonant wavelength shift (binding sensitivity B_s). The latter term B_s is a function of the thickness (d_{ad}) and refractive index (n_{ad}) of the adlayer bound to the sensing surface. Since the biomolecular layer usually has a refractive index of 1.45, which is close to that of the silica used as the defect layer in our study, in this dissertation,

we presumed the adlayer has essentially the same refractive index as the sensing surface and emphasized the relation between the sensitivity and the adlayer thickness d_{ad},

$$S = \frac{\partial I_r}{\partial d_{ad}} = \frac{\partial I_r}{\partial \lambda_R} \cdot \frac{\partial \lambda_R}{\partial d_{ad}} = O_s \cdot B_s \qquad (2.24)$$

which indicates that the overall sensitivity S of the PC-TIR sensor is given by the product of O_s and B_s.

Since the resonance of the PC-TIR sensor is a Fabry-Pérot cavity mode, its reflectance spectrum near the resonance can be described by the Lorentz equation as

$$I_r = I_0 \left[1 - \frac{1 - R_{\min}}{1 + \left(\frac{\lambda_R - \lambda_0}{\Delta\lambda / 2} \right)^2} \right] \qquad (2.25)$$

where I_0 is the incident probe light intensity, R_{min} is the minimum reflectance of the resonance dip, λ_0 is the initial resonance wavelength, and $\Delta\lambda$ is the full width at half maximum (FWHM) of the resonance dip.

When $\lambda_R = \lambda_0 \pm 0.29\Delta\lambda$, the maximum optical sensitivity $O_{s,max}$ can be obtained.

$$O_{s,\max} = \left(\frac{\partial I_r}{\partial \lambda_R} \right)_{\max} = \pm \frac{1.3 I_0 (1 - R_{\min})}{\Delta\lambda} \qquad (2.26)$$

The positive (negative) sign corresponds to the probe light wavelength lying on the lower (upper) side of the resonant dip.

According to Equation 2.23, with the assumption $n_{ad} = n_x$, there is $\alpha' = \alpha$, and the binding sensitivity B_s can be expressed as

$$B_s = \frac{4\pi n_x \cos\theta_x}{(2m+1)\pi - \alpha} \qquad (2.27).$$

Substituting Equations 2.26 and 2.27 into Equation 2.24, one obtains the maximum overall sensitivity,

$$S_{\max} = \pm \frac{5.2\pi n_{ad} \cos\theta_{ad}}{[(2m+1)\pi - \alpha]} \frac{I_0(1-R_{\min})}{\Delta\lambda} \qquad (2.28).$$

Since the minimum reflectance R_{min} can be nearly 0 by optimizing the absorption in the defect layer, and the smaller resonance dip width $\Delta\lambda$ can be easily obtained by increasing the number of the dielectric layers in the PC structures, the intensity detection mode may be used rather than the full spectral measurement in order to take advantage of the narrow resonance dip of a PC-TIR microcavity and thus achieve the highest possible sensitivity.

Of course, Equation 2.28 also implies that intensity fluctuations of the incident probe light directly affect the PC-TIR sensor response. Thus, a normalized reflectance method is required to suppress the effect of laser instability, temperature fluctuations, etc. [74]. As illustrated in Figure 2.12, a polarized probe laser beam was split into two and injected onto the PC-TIR sensor via prism coupling. The reflected light intensities from a binding area to a reference area of the sensor were recorded, and the ratio between them was used to monitor the real-time biomolecular binding event.

The normalized intensity measurement can provide very high detection resolution and then high sensitivity, but its detection range is limited by the resonance width (normally 2~3 nm). In order to extend the PC-TIR sensor's detection range, we also combined spectra measurement with normalized intensity measurement in an integrated system that will be shown in Chapter 4.

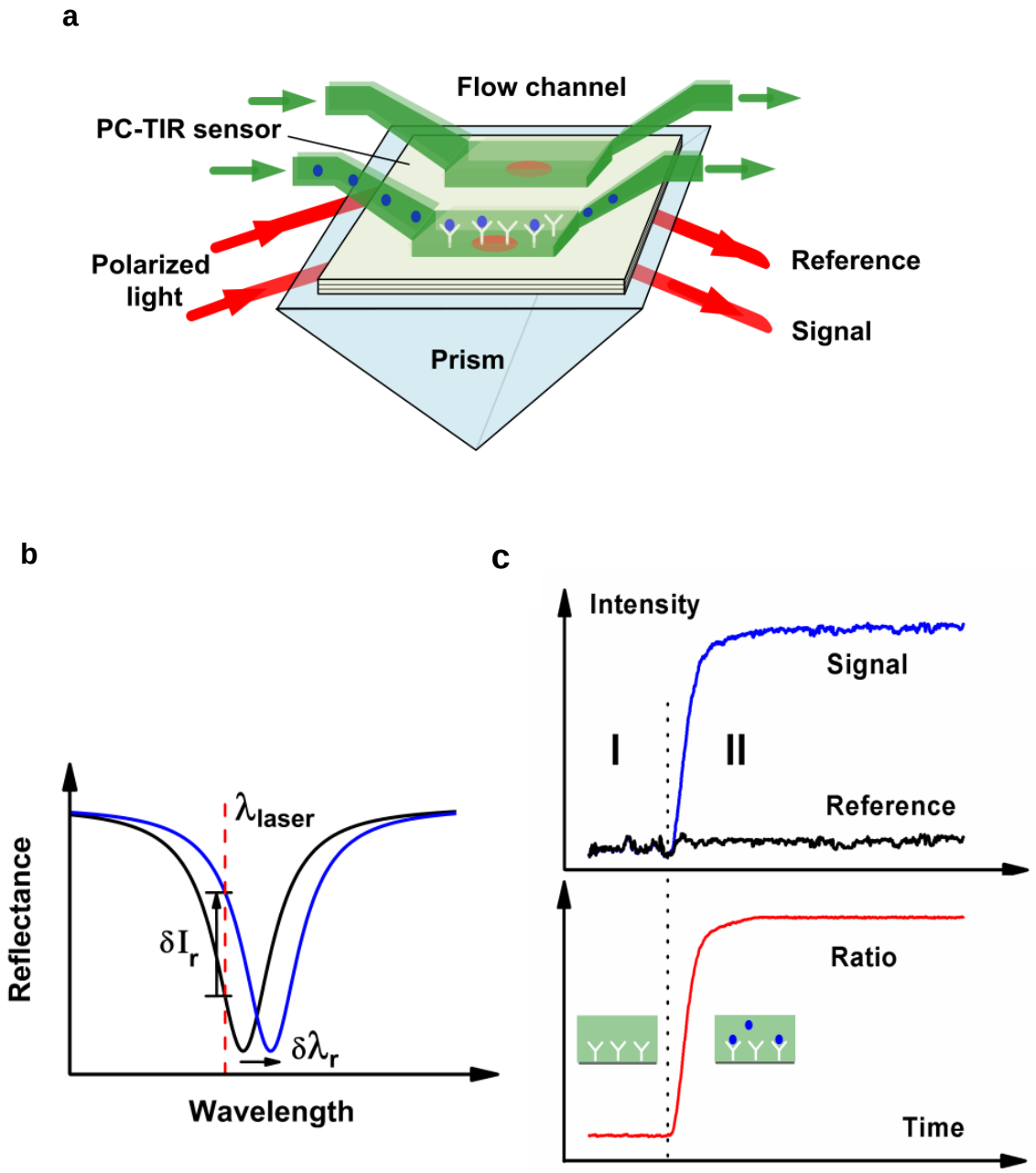

Figure 2.12 Concept of the PC-TIR sensor measurement. (a) Schematic sensor configuration showing identically polarized beams from the same light source incident on separate signal and reference channels. (b) The resonance mode shift can be monitored by directly observing the reflectance spectrum or by measuring the reflected intensity change at a laser wavelength. (c) Binding kinetics monitored by the reflected signal intensity and by the normalized intensity ratio, where region I is the baseline with ligand on the surface, and region II reflects real-time analyte binding to ligand.

2.5 Simulation on a PC-TIR Structure

As Equation 2.28 shows, the detection sensitivity of the PC-TIR sensor is mainly decided by the resonance dip width $\Delta\lambda$, minimum reflectance R_{min}, and binding sensitivity B_S, which further depends on the parameters of the PC-TIR structure: the refractive indices and thicknesses of the two dielectric constituents n_a, n_b and d_a, d_b, the number of alternating multilayer N, and the refractive index n_x, thickness d_x, and absorption k_x of the defect layer; as well as the properties of the incident light–the light polarization, the operated angle θ_i, and the probe beam size. In the following, we performed extensive numerical simulations in order to find the optimal design of the PC-TIR structure.

2.5.1 Polarization

Compared to SPR-based sensors that can only be excited with *p* polarized light, the PC-TIR structure can be operated for either *s* or *p* polarization. However, *s* polarization is preferred in biosensing applications due to its narrower resonance width and larger binding sensitivity. This can be understood from the following simulation.

As Figure 2.13 (a) shows, for the interface between layer A and layer B ($n_a = 1.45$, $n_b = 2.25$), with the same incident angle (in the substrate $n_s = 1.51$), *s* polarization obtains a larger reflectivity than *p* polarization, so that the 1-D PC structure generates a higher finesse (i.e., larger light confinement) for *s* polarization than for *p* polarization. Therefore, we can use fewer alternating dielectric layers and less optimal absorption to get a much narrower resonance dip for biosensing. As Figure 2.13 (b) shows, the 1-D PC structure ($substrate/B/(AB)^N/X$) is designed to be operated with $\lambda_R = 632.8\,\text{nm}$, $\theta_i = 63^o$, and $n_t = 1.333$. According to Equations 2.18, 2.20, 2.21, and 2.22, the thicknesses of layer A, layer B, layer X (*s* polarization), and layer X (*p* polarization) are 292.6 nm, 87.7 nm, 353.2 nm, and 359.9 nm, respectively. If the number of alternating dielectric layers (*N)* is 2, the resonance dip widths are 1 nm for *s* polarization with an optimal extinction coefficient in the defect layer $k_{xs} = 9 \times 10^{-5}$, and 70 nm for *p* polarization with an optimal extinction coefficient in the defect layer $k_{xp} = 1.5 \times 10^{-2}$. Of course, increasing the PC number can narrow down the resonance width for *p*

polarization; for example, if $N = 6$, the resonance dip width becomes 4.9 nm for p polarization with an optimal extinction coefficient in the defect layer $k_{xp} = 1 \times 10^{-3}$.

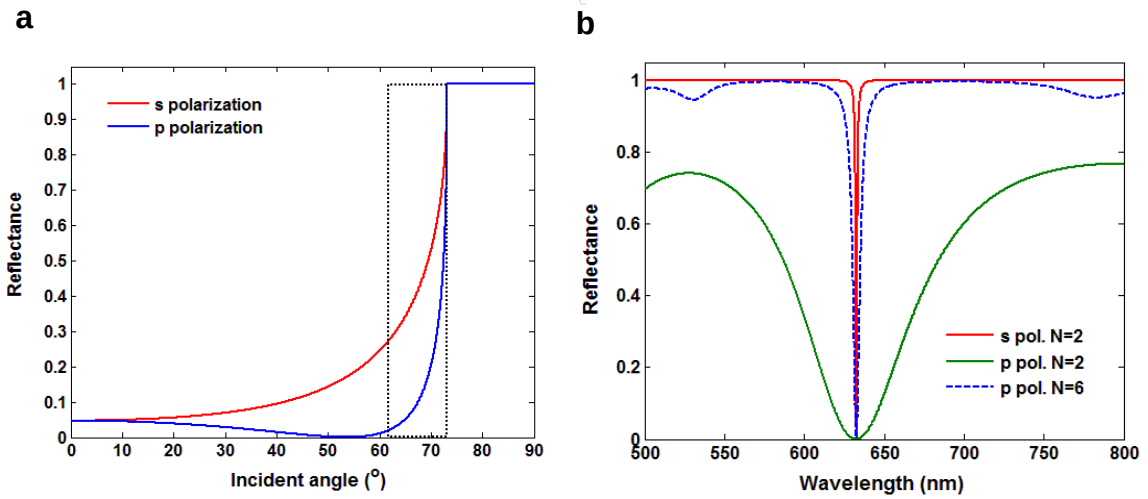

Figure 2.13 Comparison of s and p polarizations. (a) Reflectance on the interface between layer A and layer B and the dot rectangle shows the normal operation angle range for a PC-TIR structure; (b) reflectance spectrum of a PC-TIR structure with different polarizations and number of dielectric layers.

Moreover, with larger light confinement, s polarization has a higher field intensity on the sensing surface than p polarization and thus achieves a higher binding sensitivity B_s, as Table 2.1 shows. With these significant advantages, in this dissertation, s polarization is mainly considered in the PC-TIR sensor.

	N	d_a(nm)	d_b(nm)	d_x(nm)	k_x	$\Delta\lambda$(nm)	B_s(nm/nm)
s pol.	2	292.6	87.7	353.2	9×10^{-5}	1.0	1.32
p pol.	2	292.6	87.7	359.9	1.5×10^{-2}	70	0.72
	6	292.6	87.7	359.9	1×10^{-3}	4.9	0.57

Table 2.1 Comparison of s and p polarizations for the PC-TIR sensor.

2.5.2 Number of 1-D PC layers

Compared to a fixed broad resonance mode in an SPR-based sensor, one of the big advantages of the 1-D PC-based structure is that it can achieve a narrower resonance mode by simply increasing the number of alternating dielectric layers. That is due to a higher finesse of the Fabry-Pérot microcavity.

For example, with the same PC-TIR structure design for *s* polarization as Section 2.5.1, when the number of alternating dielectric layers (*N*) increases from 1 to 2 to 3, the resonance dip width $\Delta\lambda$ becomes dramatically narrower from 10.5 nm to 1.0 nm to 0.08 nm, but the shift due to biomolecular adsorption (assume $n_{ad} = 1.45, d_{ad} = 5nm$) just slightly decreases. Meanwhile, the extinction coefficient k_x of the defect layer needed to achieve optimal minimum reflectance decreases from 1×10^{-3} to 9×10^{-5} to 8×10^{-6}. However, we cannot infinitely narrow down the resonance width by increasing the number of PC layers because the optimal k_x becomes too little to be obtained due to unavoidable scattering loss on the interface. We are going to discuss the experimental limitations in Chapter 3.

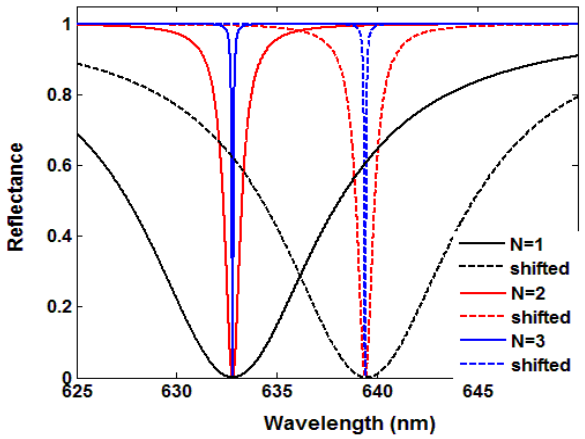

Figure 2.14 Effect of the number of 1-D PC layers on resonance width and binding shift.

2.5.3 Refractive index contrast of 1-D PC layers

It is easy to understand that high-index-contrast dielectric layers are preferred in fabricating a 1-D PC structure, as they can achieve high reflectivity, thus forming a high finesse Fabry-Pérot microcavity in the defect layer. Moreover, with the same number of PC layers, high-index-contrast materials produce higher field intensity on the sensing surface and, thus, larger binding sensitivity.

We compare two sets of dielectric materials: 1) $n_a = 1.45$, $n_b = 2.25$ and 2) $n_a = 1.45, n_b = 2.00$. All the other parameters of the PC-TIR structure are the same as in Section 2.5.1 ($N = 2$). As shown in Figure 2.15, the first set has a narrower resonance

width ($\Delta\lambda = 1.0$ nm) and larger binding sensitivity ($B_s = 1.32$ nm/nm) than the second one ($\Delta\lambda = 2.8$ nm, $B_s = 1.22$ nm/nm). At the same time, the optimal absorption of the first one ($k_x = 9 \times 10^{-5}$) is smaller than the second one ($k_x = 3 \times 10^{-4}$).

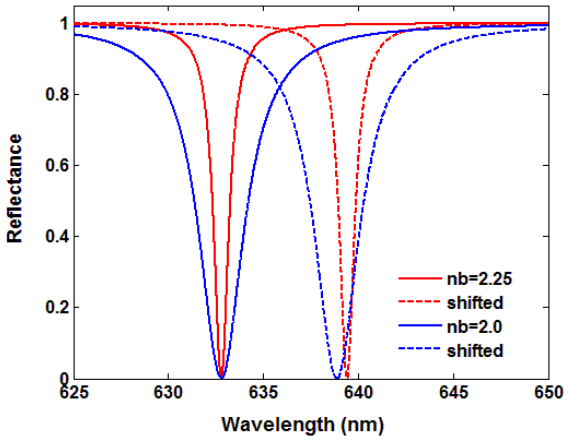

Figure 2.15 Effect of the index-contrast of dielectric layer materials on resonance width and binding shift (assume $n_{ad} = 1.45$, $d_{ad} = 5nm$).

2.5.4 Incident angle

The operating incident angle θ_i is a very important parameter of the PC-TIR structure. On one side, it should be large enough that TIR occurs between the defect layer and the surrounding medium, but smaller than the critical angles for the dielectric layers; on the other side, the thicknesses of all the PC-TIR structure layers are decided by the designed incident angle. A larger incident angle produces larger light confinement, thus a narrower resonance mode. However, a smaller incident angle, which is easier to achieve TIR and also produces less confinement, was preferred in the experiments.

We still follow the same design as Section 2.5.1 except that light is *s*-polarized, $N = 2$, and θ_i (in the substrate) is to be set; clearly, the incident angle range is $\sin^{-1}(\mathrm{n_t}/\mathrm{n_s}) < \theta_i < \sin^{-1}(\mathrm{n_a}/\mathrm{n_s})$, that is $61.98^{\mathrm{o}} < \theta_i < 73.79^{\mathrm{o}}$. We chose θ_i to be $63^{\mathrm{o}}, 64^{\mathrm{o}}$ for comparison, and the results are shown in Figure 2.16 and listed in Table 2.2.

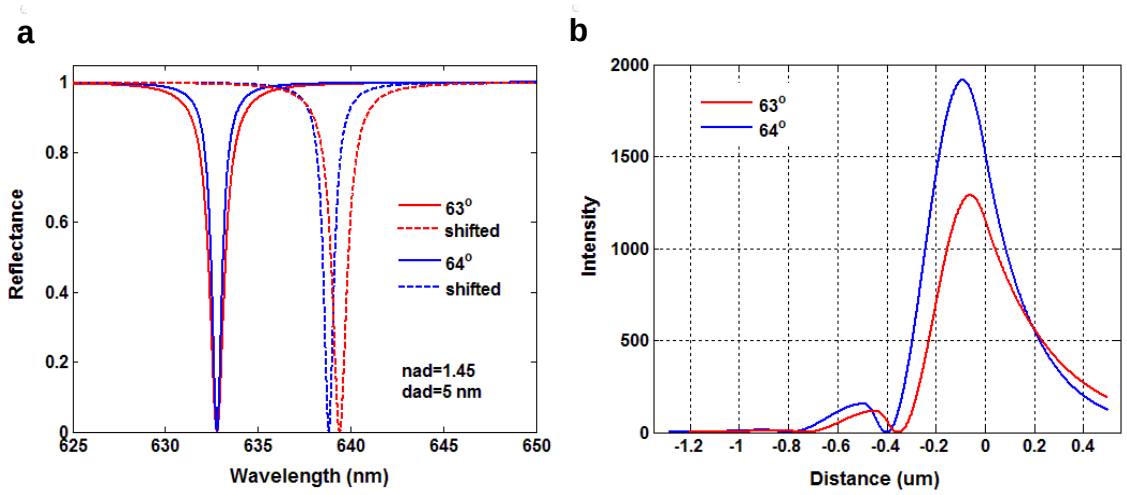

Figure 2.16 Effect of the incident angle on (a) resonance width and binding shift; (b) intensity enhancement.

θ_i	d_a(nm)	d_b(nm)	d_x(nm)	k_x	$\Delta\lambda$(nm)	B_s(nm/nm)	I_{sur}	L_{de} (nm)
63°	292.6	87.7	353.2	9×10^{-5}	1.00	1.32	1160	276.8
64°	309.9	88.2	401.3	5×10^{-5}	0.65	1.21	1533	197.3

Table 2.2 Effect of incident angle on the PC-TIR sensor.

It was found that a larger operating angle achieved a narrower resonance dip, larger sensing surface intensity I_{sur}, smaller optimal absorption, but smaller binding sensitivity and shorter decay length L_{de}. The smaller binding sensitivity could be explained as a smaller portion of the resonance mode interacting with biomolecules in the evanescent region.

Compared to a Fabry-Pérot resonator operating at normal incidence, the PC-TIR structure operating at an incident angle larger than the critical angle has a much wider photonic bandgap, which broadens the sensor's detection range.

In addition, the propagation length L_P along the sensing surface can be approximately determined from the resonance width $\Delta\theta$ of the resonance curve [75]:

$$L_P \approx \left(\frac{2\pi}{\lambda} n_s \cos\theta_{res} \Delta\theta \right)^{-1} \qquad (2.29).$$

For an SPR-based sensor consisting of 50-nm gold film on a glass slide, the resonance angle is 72.2° at 632.8 nm and the resonance angle width is 5.5°. Its decay length is 91.5 nm and the plasmon propagation length is 2.3 μm; in contrast, for the PC-TIR sensor described here ($\theta_i = 63^o$), the decay length is 276.8 nm, 3 times larger than that of the SPR-based sensor. The resonance angle width of the PC-TIR sensor is 0.014°; therefore, the propagation length is 620 μm, over 300 times longer than that of the SPR sensor. The longer decay length and propagation length can greatly increase the detection area for biomolecular interactions and thus the detection sensitivity, which may be a big advantage compared to an SPR-based sensor, especially for detecting large molecules or for imaging applications.

2.5.5 Defect layer thickness, index and absorption

The defect layer *X* plays an extremely important role in the PC-TIR structure. The Fabry-Pérot microcavity forms in this layer, which also provides the sensing surface interacting with biomolecules in the evanescent field. In the following, we will discuss the effect of its index, thickness, and absorption on the performance of the PC-TIR sensor (resonance mode and detection sensitivity), separately.

(a) We still follow the same design as Section 2.5.1 except that light is *s*-polarized, $N = 2$, $\theta_i = 63^o$, and n_x is variable; since the biological molecules normally have refractive indices around 1.45, we tested three n_x values: 1.42, 1.45, 1.49 for comparison, and the results are listed in Table 2.3 and shown in Figure 2.17.

n_x	d_x(nm)	k_x	$\Delta\lambda$ (nm)	B_s(nm/nm)	I_{sur}	l_{de} (nm)
1.42	433.0	5×10^{-5}	0.79	1.54	1642	276.8
1.45	353.2	9×10^{-5}	1.00	1.32	1160	276.8
1.49	290.7	1.5×10^{-4}	1.07	1.12	859	276.8

Table 2.3 Effect of refractive index of the defect layer on the PC-TIR sensor.

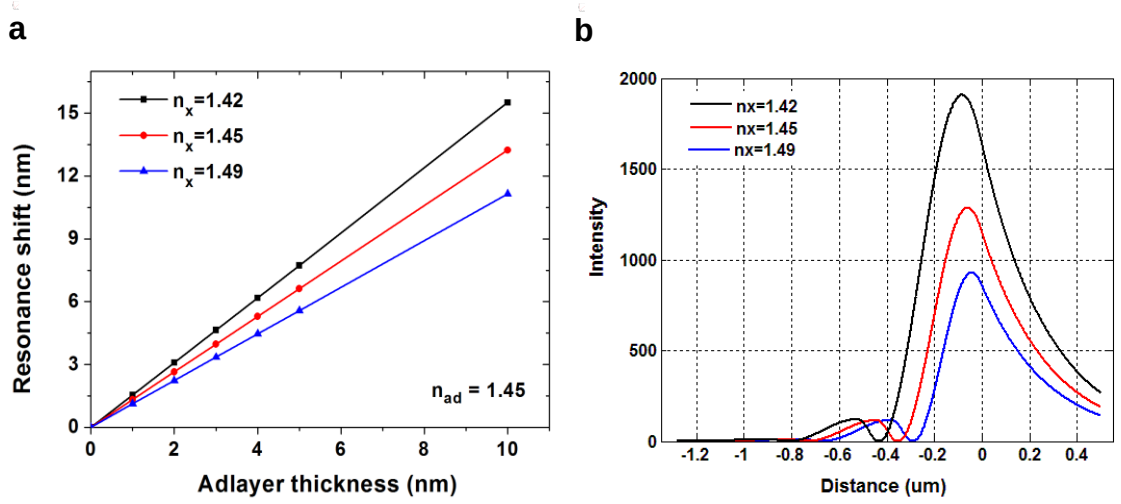

Figure 2.17 Effect of the refractive index of the defect layer on (a) binding sensitivity; (b) intensity enhancement.

It was found that the smaller n_x is preferred for the PC-TIR structure. First, the resonance shift is linearly proportional to the bound adlayer thickness, as Equation 2.27 predicted that the binding sensitivity is a constant and decided by n_x. A smaller n_x brought larger binding sensitivity, which can be explained by the effective change Δd_{eff} of the defect layer thickness. With the same adlayer index and thickness, the Δd_{eff} was larger for a smaller n_x and thus brought a large binding shift. Moreover, with a smaller n_x, the defect layer thickness d_x needed for resonance was thicker, thus the resonance width became smaller and the intensity enhancement on the sensing surface was larger, although the decay length remained the same for the same incident angle.

(b) The thickness of the defect layer is designed according to Equations 2.20 and 2.21. However, in experiments, the actual deposition thickness may change, which will affect the operative incident angle (of intensity measurement). If it is too thick, the operative incident angle has to be adjusted to be larger; if it is too thin, the operative angle will become smaller. In either case, the effect of the incident angle will be the same, as Table 2.2 shows. One point worth mentioning is that a larger incident angle produced higher light confinement so that the optimal absorption became less.

In addition, Equation 2.20 implies that multiple resonance modes can be achieved with a thicker thickness of the defect layer. However, although the resonance dip width

was narrower with a larger m, the binding sensitivity decreased and the optimal absorption became less, as Figure 2.18 (a) shows. For biosensing application, it is preferable to use $m = 0$ due to larger binding sensitivity and simpler fabrication to enable a more uniform layer.

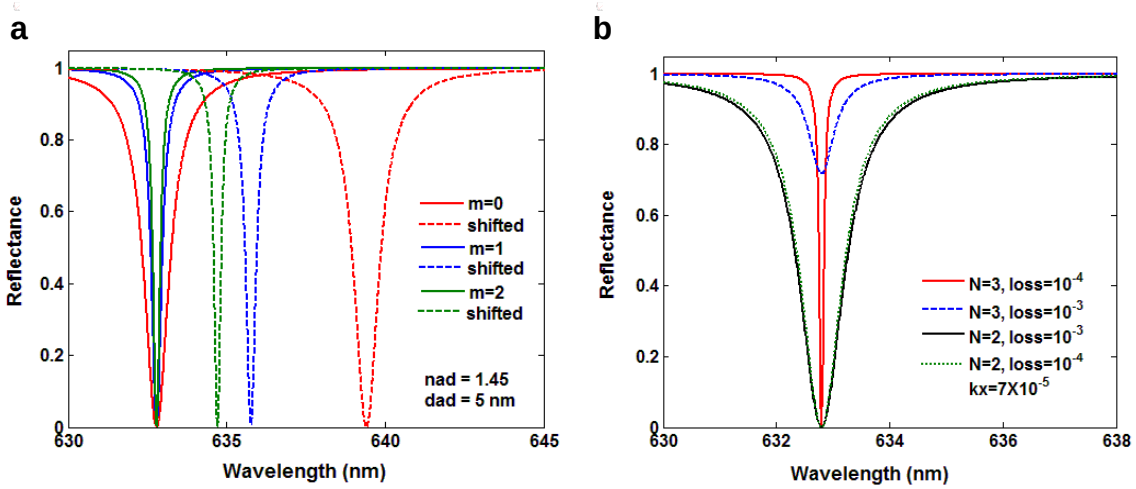

Figure 2.18 Resonance modes and binding sensitivity are affected by (a) the thickness of the defect layer; (b) the scattering loss and absorption in the defect layer.

(c) The absorption of the defect layer is a critical parameter for the PC-TIR structure. As Figure 2.10(a) shows, too much or too little absorption won't achieve a sharp resonance dip, and there exists an optimal absorption to achieve minimum reflectance R_{min} and thus high sensitivity (see previous examples). However, as we mentioned above, scattering loss also contributes to the absorption. The effect can be considered as adding one more scattering loss matrix to the transfer matrix calculation.

$$M_{loss} = \begin{bmatrix} \exp(-\alpha) & 0 \\ 0 & \exp(\alpha) \end{bmatrix} \qquad (2.30)$$

where α represents the scattering loss on the interface between two media.

When the structure exhibits very strong light confinement, the extinction coefficient k_x of the defect layer needed to achieve optimal minimum reflectance is very little and the scattering loss between different media may be beyond this value and dominate the achievable R_{min}. For example, we follow the same design as section 2.5.1 except that N and k_x are variable; if the scattering loss on the interface between the defect layer and the surrounding medium is $\alpha = 10^{-3}$, without absorption in the defect layer, it makes R_{min}=0

for $N = 2$; but it is too much (R_{min}= 0.72) for $N = 3$. If $\alpha = 10^{-4}$, it makes R_{min}= 0 for $N = 3$ and needs more absorption ($k_x = 7 \times 10^{-5}$ for the defect layer) to get R_{min}= 0 for $N = 2$, which is preferable in our design because the scattering loss α is uncontrollable. The PC-TIR structure should have a reasonable light confinement to obtain narrow $\Delta\lambda$, and also to keep the absorption in the defect layer larger than the scattering loss so that we can control the total absorption well in order to achieve minimum reflectance R_{min} on resonance.

2.5.6 Probe beam size

In all the previous simulations, the probe light was assumed to be a collimated plane wave, and the incident angle was a specific value. However, a Gaussian beam is more accurate to describe the input laser beam. When the beam size becomes smaller, close to the laser wavelength, the collimated laser beam (Gaussian beam) will have a divergence angle as follows:

$$\theta \approx \frac{\lambda}{\pi w_0} \tag{2.31}$$

where λ is the incident laser wavelength and w_0 is the waist of the Gaussian beam.

Since the PC-TIR sensor has a very narrow resonance mode, the divergent beam including a range of incident angles will broaden the resonance dip and thus decrease the detection sensitivity, as Figure 2.19 shows. Therefore, there is a trade-off between the beam size and the detection sensitivity.

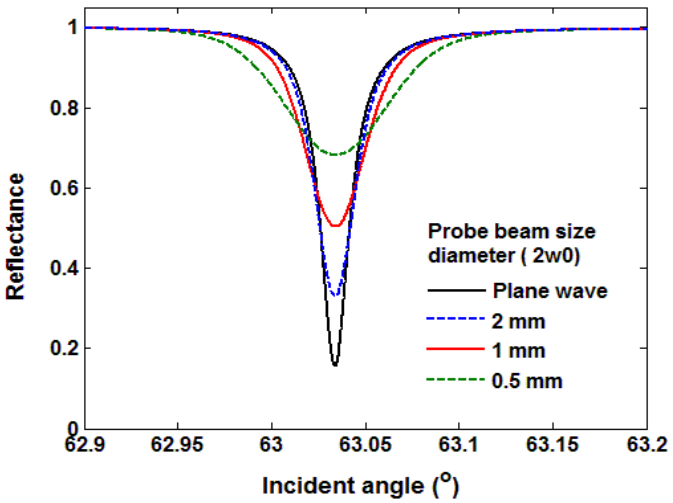

Figure 2.19 The resonance dip changes with the probe beam size.

2.6 Conclusion

In this chapter, I first introduced the transfer matrix method for calculating the transmission and reflection of multilayer structures and explored the operating principle of the PC-TIR structure. I also discussed effective methods for monitoring the resonance mode shift and deriving the detection sensitivity. Finally I made a comprehensive simulation, discussing the effects of each parameter of the PC-TIR structure and the properties of the incident angle on the sensor's performance.

	pol.	θ_i	w_0	N	n_b/n_a	n_x	d_x	k_x
$\Delta\lambda$	*s*	large	large	large	large	small	large	small
B_s	*s*	small	none	small	large	small	small	none

Table 2.4 Effects of the structure parameters and the incident light properties on the performance of the PC-TIR sensor.

As Table 2.4 shows, the preference of each parameter is given according to its effect on resonance dip width and binding sensitivity. There is no doubt that the PC-TIR structure benefits from *s* polarization, high-index-contrast dielectric layers, and a small refractive index of the defect layer. Moreover, it is easy to achieve a narrow resonance width and thus detection sensitivity by increasing the number of 1-D PC layers or the incident angle, although the binding sensitivity may decrease. However, they also produce large light confinement and need a small amount of absorption to optimize the minimum reflectance at resonance wavelength. To get a small value of minimum reflectance R_{min} is also very important to improve the detection sensitivity. There is a trade-off between the resonant dip width $\Delta\lambda$ and the minimum reflectance R_{min}. I will discuss how to balance them to make a suitable PC-TIR sensor structure in Chapter 3. In addition, small probe beam size can reduce the flow cell size and thus reduce sample volume (detailed discussion referring to section 6.2.1.1), but may broaden the resonance dip width and worsen the sensitivity. Thus there also exists a trade-off between these two. As a result, the probe beam size is set to be 1 mm in this dissertation work.

Chapter 3

Fabrication of a PC-TIR Structure

3.1 Introduction

The photonic crystal-total internal reflection (PC-TIR) sensor we are dealing with in this dissertation is actually a multilayer dielectric structure. It can be easily fabricated by mature thin film fabrication methods [76], including electron-beam physical vapor deposition (EBPVD), ion-beam assistant deposition (IBAD), molecular beam epitaxy (MBE), chemical vapor deposition (CVD), etc.

However, as we discussed in Chapter 2, in order to get high sensitivity, we need to carefully choose the parameters of the PC-TIR structure: the refractive indices and thicknesses of the two dielectric constituents; the number of alternating multilayers; and the refractive index, thickness and absorption of the defect layer. In this chapter, with consideration to experimental conditions, we discuss how to design and fabricate a suitable PC-TIR structure.

3.2 Design of a PC-TIR Structure

The PC-TIR sensor can be designed to operate at any wavelength by choosing suitable materials. In this dissertation, we explore its operation in visible wavelengths. The optical sources used here are a Helium-Neon (HeNe) laser (632.8 nm) for intensity measurement and a broadband incandescent lamp for spectrometer measurement. The operative wavelength is set to be $\lambda_0 = 632.8nm$. In addition, the surrounding medium is de-ionized (DI) water ($n_t = 1.333$), which is close to the solvent or buffer used in biological research.

First, for the dielectric materials in the 1-D PC structure, we chose titanium dioxide (TiO_2) and silicon dioxide (SiO_2) as the high and low refractive index materials (*B* and *A*), respectively. They are high-index-contrast in visible range and are also easily amenable to accurate fabrication by EBPVD. Their physical thicknesses are mainly decided by Equation 2.18. They also can be tuned a little away from the ideal values to reduce the large confinement of the PC-TIR structure, so that it is more flexible in managing suitable absorption in the defect layer. A comparison of PC structures with different light confinements is shown in Section 3.3.3.

Second, increasing the number of dielectric layers *N* can greatly narrow the resonance dip width $\Delta\lambda$, which is a pronounced advantage of the PC-TIR structure. As we discussed in Chapter 2, it also causes a large light confinement so that the need for an optimal absorption to achieve minimum reflectance is reduced. Based on the experimental results we got, we adjusted the thicknesses of the PC layers a little away from the ideal thicknesses and used a suitable *N* value ($N = 3$) to get a narrow resonance mode for the PC-TIR structure: $substrate / B / (AB)^N / X$. Since the substrate we normally use is BK7 glass that has a refractive index close to SiO_2, the first TiO_2 layer together with the substrate actually forms an additional high-index-contrast pair.

Third, the operative angle θ_i is also an important parameter for the PC-TIR structure, as discussed in Chapter 2. For an SPR-based sensor, the operative angle is limited due to a phase-matching condition, and a large incident angle ($> 70^o$) is needed to run at short wavelength (like 632.8 nm). For the PC-TIR sensor, we can design a smaller operative angle, which makes it easier to achieve TIR and also produces less confinement. Here the operative angle θ_i is designed to be 63^o.

Fourth, the defect layer *X* plays an extremely important role, as section 2.5.5 showed–especially the absorption in the defect layer. In previous fluorescence enhancement experiments [57], a dye-doped polymer film was spin-coated on the PC structure as the absorptive defect layer, but it was very hard to get a stable, uniform layer with accurate thickness and precise absorption, which was critical for further biomolecular detection. In our study, we chose pure silicon (Si) as a separate absorptive layer, as it has small absorption in the visible range and is also much easier to obtain a

uniform and accurate thickness film on the 1-D PC structure by EBPVD than dye doped polymer by spin coating. One more silica layer was deposited on top of the silicon layer as the final component of the defect layer. The silica surface is commonly used in biomolecular studies and there are established methods for surface functionalization for molecular binding measurements. Another reason we put silicon as the bottom of the defect layer instead of the top layer is that the field at the bottom is much smaller than at the top (as Figure 3.1 shows), which allows greater flexibility to control the absorption. Therefore, the thickness of the absorptive silicon layer is designed to get minimum reflectance at resonance wavelength, and the thickness of the silica layer is designed by the transfer matrix method to get a resonance mode at a wavelength with a suitable operative angle.

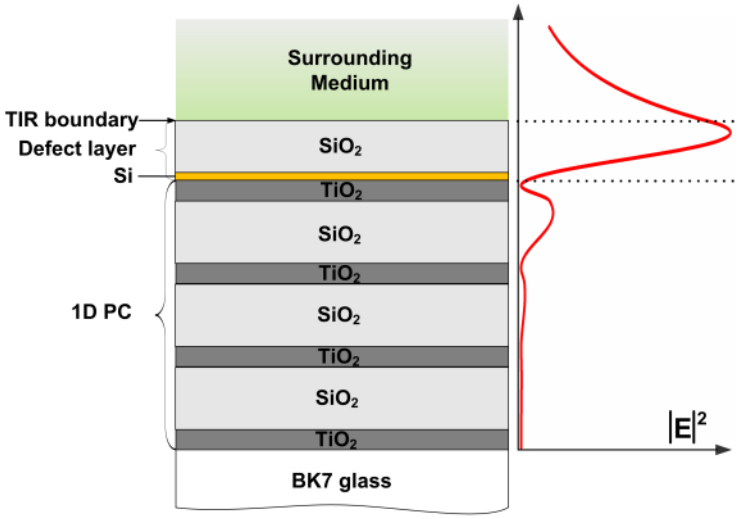

Figure 3.1 Schematic of a PC-TIR sensor structure. The left part is the schematic structure of the 1-D PC-TIR structure, and the right shows electric field intensity distribution when light is resonant with the structure. The dotted lines show the two boundaries of the defect layer.

In all, the procedure of the PC-TIR structure design and fabrication is:

1) Determine the conditions ($\lambda_0 = 632.8nm, n_t = 1.333, \theta_i = 63^o$) and the structure:

   $substrate / TiO_2 / (SiO_2 / TiO_2)^3 / Si / SiO_2$;

2) Design the thicknesses of the 1-D PC structure (d_a, d_b);

3) Fabricate and measure the actual thicknesses and refractive indices of the 1-D PC layers (by ellipsometry);

4) Determine the silicon thickness d_{xSi} and the top silica thickness d_{xSiO_2};
5) Fabricate the defect layer (silicon and silica layers) and test the resonance dip of the completed structure in experiments;
6) If needed, adjust the silicon thickness or the silica thickness (which also changes the actual operative angle) until attainment of a suitable resonance dip for use.

3.3 Fabrication of a PC-TIR Structure

3.3.1 Fabrication method

All the dielectric materials used (SiO_2, TiO_2, Si) can be fabricated by electron-beam physical vapor deposition (EBPVD). It is a typical physical vapor deposition (PVD) process that is performed in a vacuum chamber ($10^{-6} \sim 10^{-7}$ torr), as shown in Figure 3.2.

The deposition process is described thus: a high *dc* voltage is applied to a tungsten filament that causes electrons to be discharged. The stream of electrons emitted excites the targeted solid materials and turns them into vapor, which travels to the substrate. As it reaches the surface, it condenses and forms a thin film coating. The deposition rate in this process can be as low as 1 nm per minute, which enables us to make uniform dielectric layers. In addition, the EBPVD system can be equipped with ion sources to do ion beam assisted deposition (IBAD), which makes more uniform deposition layers.

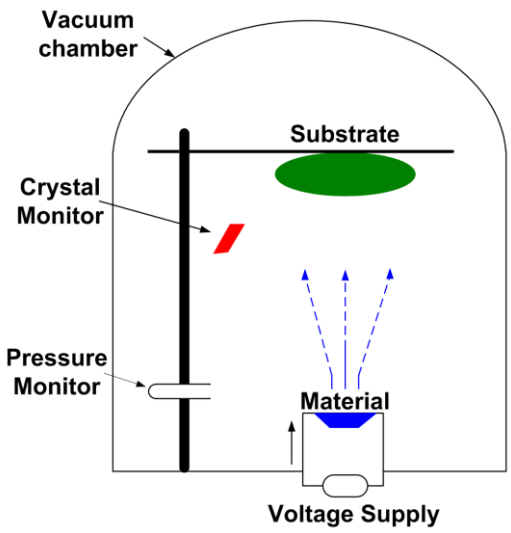

Figure 3.2 Schematic diagram of electron beam physical vapor deposition

3.3.2 Refractive indices of dielectric materials

It is important to know all the refractive indices of the materials of which the PC-TIR structure consists, as this determines the properties of the structure.

The substrate material BK7 glass has been well studied, and its refractive index can be approximated by the Sellmeier equation, which is an empirical relationship between the refractive index and the wavelength for a particular transparent medium. The usual form of the equation for glasses is [77]:

$$n^2(\lambda) = 1 + \frac{B_1\lambda^2}{\lambda^2 - C_1} + \frac{B_2\lambda^2}{\lambda^2 - C_2} + \frac{B_3\lambda^2}{\lambda^2 - C_3} \tag{3.1}$$

where n is the refractive index, λ is the vacuum wavelength (expressed in μm), and B_1, B_2, B_3 and C_1, C_2, C_3 are experimentally determined Sellmeier coefficients. Table 3.1 lists the coefficients for BK7 and fused silica [77]. Then we get the dispersion curve of BK7 glass as Figure 3.3 shows, and it has a refractive index of 1.515 at wavelength 632.8 nm.

Material	B_1	B_2	B_3	C_1(μm^2)	C_2(μm^2)	C_3(μm^2)
BK7	1.03961212	0.231792344	1.01046945	6.00069867×10^{-3}	2.00179144×10^{-2}	1.03560653×10^{2}
Fused silica	0.696166300	0.407942600	0.897479400	4.67914826×10^{-3}	1.35120631×10^{-2}	97.9340025

Table 3.1 Coefficients of the Sellmeier equation for BK7 and fused silica.

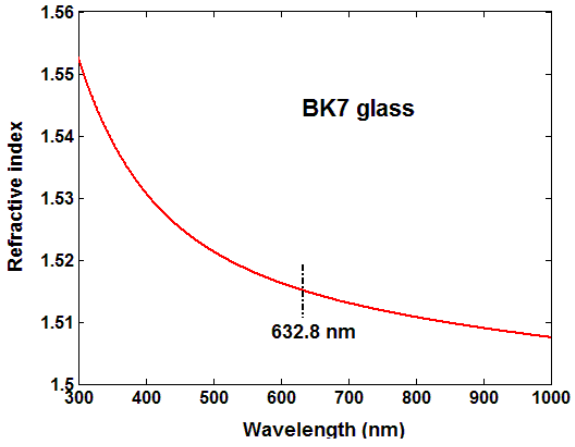

Figure 3.3 Dispersion data of BK7 glass.

For the SiO_2, we normally use fused silica as the deposition material, and its optical dispersion can also be approximated by the Sellmeier equation shown above. However, the actual deposited SiO_2 layer sometimes may have a different refractive index from the approximated value due to deposition conditions, so it is better to use the measured refractive index of the deposited SiO_2 layer to calculate the PC-TIR structure. As Figure 3.4 (a) shows, the dispersion properties of the SiO_2 material is stable for different coatings, and the refractive indices at other wavelengths can be derived using the dispersion data (i.e., interpolation). It has a refractive index of 1.451 at wavelength 632.8 nm (i.e., $n_{SiO_2} = 1.451$), a little different from the value of 1.457 calculated by Equation 3.1.

For the TiO_2, there are also some empirical equations to calculate its dispersion; however, its optical properties are very sensitive to deposition conditions (chamber pressure, substrate temperature, deposition rate, etc.)[78]. As Figure 3.4 (b) shows, the deposited TiO_2 materials have different refractive indices for three different coating samples. Its refractive indices at other wavelengths can be derived using available experimental data. Its refractive index n_{TiO_2} at wavelength 632.8nm is 2.211, 2.251, and 2.232 for the first, second and third coating, respectively.

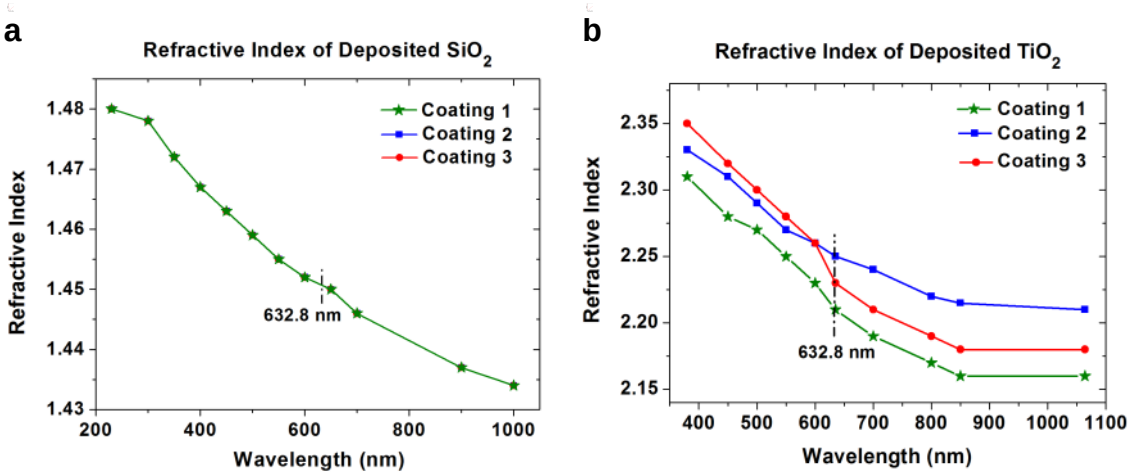

Figure 3.4 Dispersion data of three coating samples for (a) SiO_2, (b) TiO_2

For Si, we use amorphous silicon material, which is the non-crystalline allotropic form of silicon and can be deposited in thin films at low temperatures onto a variety of

substrates. Its optical properties have been well studied, and we get its dispersion and absorption properties from the experimental data in reference [79], as Figure 3.5 shows. Refractive index (RI) and absorption are the real and imaginary part of the more general complex RI constant and are related to each other via the Kronig-Kramers relations. Its RI constant at wavelength 632.8 nm is $n = n_{Si} - i \cdot k_{Si} = 3.873 - i \cdot 0.015$.

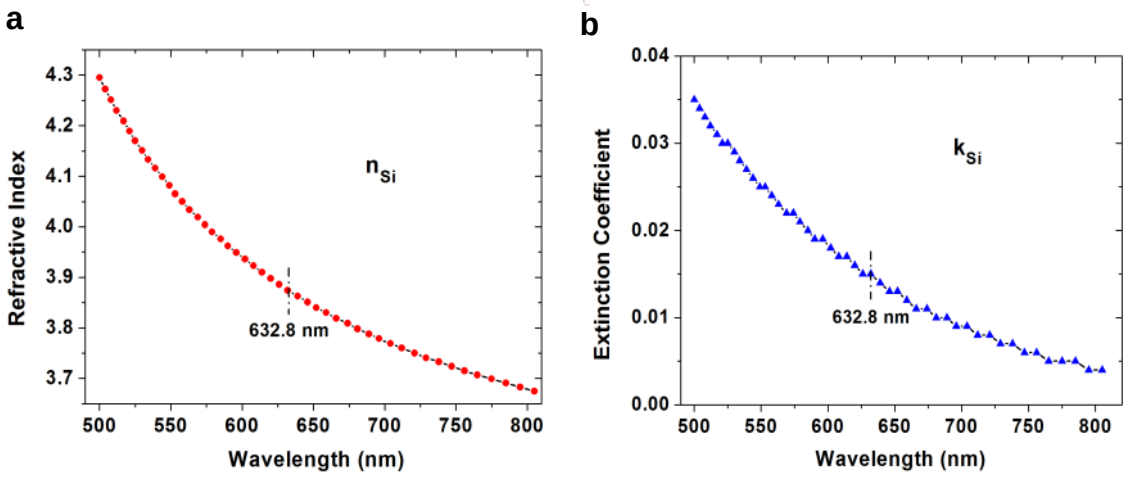

Figure 3.5 Dispersion data of pure silicon (a) refractive index (real part); (b) extinction coefficient (imaginary part).

3.3.3 Fabrication of the 1-D PC structures

According to the design in section 3.2, if we set $n_a = 1.451$ and $n_b = 2.231$, the thicknesses of the SiO_2 and TiO_2 layers should be $d_a = 297.3nm$ and $d_b = 89.1nm$. Three batches of 1-D PC structures, that is, $substrate(BK7)/TiO_2/(SiO_2/TiO_2)^3$, were fabricated by Rainbow Research Optics, Inc. The refractive indices of the three coating samples are shown in Figure 3.4, and the measured thicknesses are listed in Table 3.2, as well as the refractive indices at the wavelength of 632.8 nm.

Sample	n_a	n_b	d_a (nm)	d_b (nm)
Coating 1	1.451	2.211	287	87
Coating 2	1.451	2.251	334	106
Coating 3	1.451	2.232	330	107

Table 3.2 Structure parameters of three coating 1-D PC structures.

In order to further verify the parameters of these PC structures, we measured their transmission spectra at normal incidence. For example, as Figure 3.6 shows, the third coating sample is in good agreement with the simulated result.

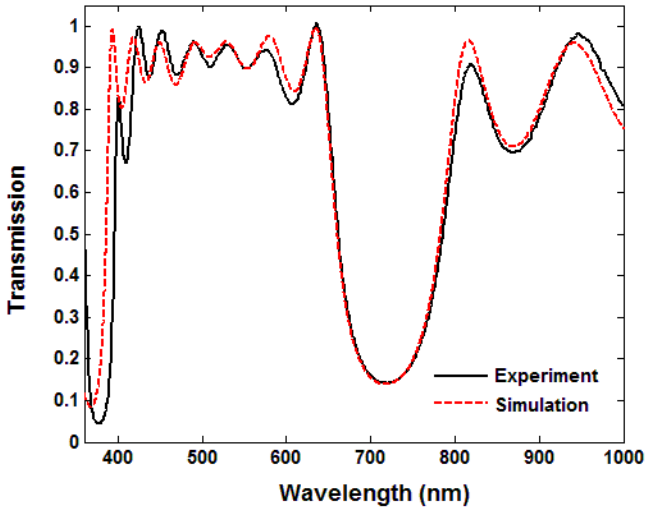

Figure 3.6 Experimental and simulated transmission spectra of the third coating sample (1-D PC structure) at normal incidence.

Obviously, the thicknesses of the three 1-D PC structures are not identical to the ideal thicknesses calculated by Equation 2.18. However, as we discussed above, in this case, the PC structure with less light confinement is more flexible in managing suitable absorption in the defect layer to get a sharp resonance dip. In order to quantitatively compare the confinement abilities (i.e., intensity enhancement), as Figure 3.7 shows, we calculated the intensity distribution of these PC structures with corresponding defect layers (pure silica layers with suitable thicknesses, as Table 3.3 shows), which were resonant at wavelength 632.8 nm with the same resonance angle 63^{o} in the substrate.

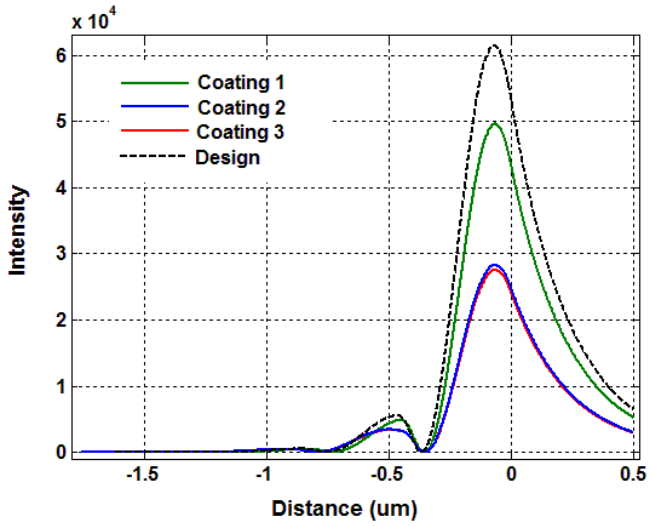

Figure 3.7 Intensity distributions of different PC structures with suitable defect layers on resonance.

	d_x (nm)	I_{sur}
Design	369.2	5.31×10^4
Coating 1	361.5	4.31×10^4
Coating 2	331.7	2.46×10^4
Coating 3	332.3	2.39×10^4

Table 3.3 Defect layer thickness and surface intensity of different 1-D PC structures on resonance.

It was found that the designed 1-D PC structure had the largest intensity enhancement on the sensing surface (i.e., $x=0$), thus the highest confinement ability; the first coating had a reduced but still high surface intensity; the second and the third coatings had almost the same surface intensity–less than one-half of the designed one–which gave them larger flexibility in managing absorption to get a sharp resonance dip. Meanwhile, the large intensity enhancement on the sensing surface ($I_{sur}>2\times10^4$) also enabled them to get narrow resonance modes.

3.3.4 Fabrication of suitable PC-TIR structures

Fabrication of 1-D PC structures is only the first step, and it is more critical to make a suitable defect layer for good performance. We need to manage the absorption in the defect layer very well, with considerations to uncontrollable scattering loss. Since we are using the silicon film for the intentional absorption of the defect layer, a good way is to try different silicon layer thicknesses d_{xSi} and determine which is the suitable one. In addition, the top silica layer thickness d_{xSiO_2} is also important and needs to be engineered well because it decides the operative incident angle that also has a large effect on light confinement, as discussed in Section 2.5.4.

A. PC-TIR structure based on the first coating

First, we tested the large-confinement PC structures–the first coating samples, marked as CBA71. According to the simulation, the minimum reflectance $R_{\min}$ can be 0 if the extinction coefficient of the defect layer is $k_x \approx 10^{-5}$ or the scattering loss between the defect layer and the surrounding medium (water) is $\alpha_{opt} \approx 10^{-4}$.

We fabricated a PC-TIR structure with an 18-nm silicon layer and a 350-nm silica layer on top of the first coating PC structure and then measured its reflectance spectra in the experimental system (shown in Chapter 4). When the surrounding medium was DI-water, as Figure 3.8 (a) shows, there appeared a narrow resonance dip, which shifted with the change of the incident angle θ_i. However, the resonance dip was very shallow with $R_{\min} = 0.84$ when $\theta_i = 63.15^o$. Obviously, this PC-TIR structure did not have the optimal absorption. Assuming that there was some scattering loss α on the interface between the top silica layer and the DI-water, we did some simulation and found out that the experimental dip could be fitted with $\alpha_{water} = 2\times10^{-3}$, as Figure 3.8 (b) shows. Compared to the optimal scattering loss $\alpha_{opt} \approx 10^{-4}$, there was too much scattering loss and absorption loss in the experiments for the PC-TIR structure using the high confinement CBA71 structure.

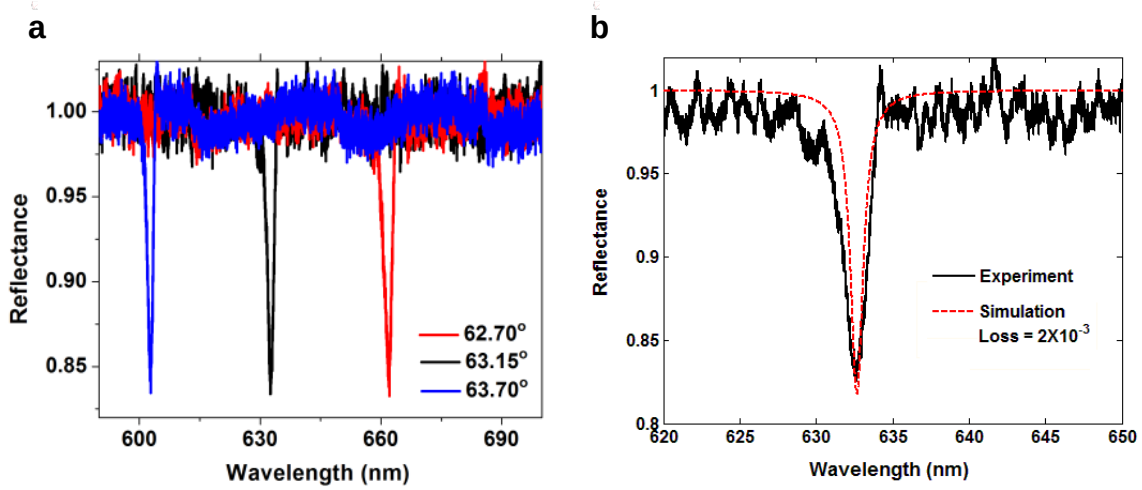

Figure 3.8 (a).Experimental reflectance spectra of PC-TIR structure at different incident angles with DI-water on top; (b) experimental and simulated spectra of the PC-TIR structure.

We also measured the reflectance spectra when the surrounding medium was changed from DI-water ($n_t = 1.333$) to air ($n_t = 1.000$). As Figure 3.9 shows, when the incident angle $\theta_i = 58.95^o$, the PC-TIR structure had a resonance dip at the wavelength of 632.8 nm with a narrow resonance width $\Delta\lambda$ of 1.20 nm and a small minimum reflectance R_{min} of 0.23, which shifted with the incident angle. We estimated the scattering loss using simulation and discovered that $\alpha_{air} = 1.4 \times 10^{-3}$.

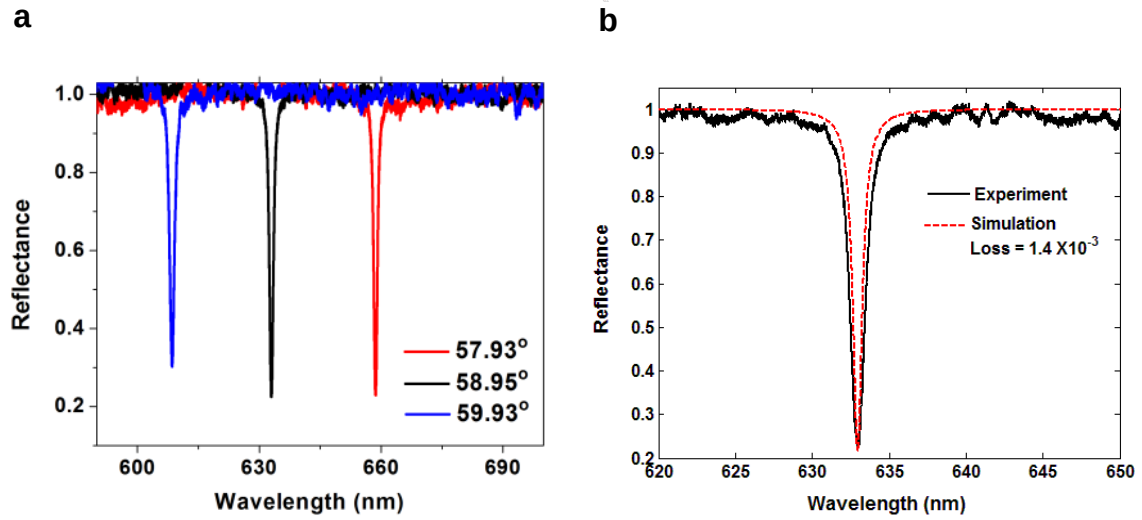

Figure 3.9 (a) Experimental reflectance spectra of the PC-TIR structure at different incident angles with air; (b) experimental and simulated spectra of the PC-TIR structure.

The much smaller R_{min} for air could be explained in that the smaller incident angle greatly reduced the light confinement of the PC structure so that the absorption loss and the scattering loss were close to the optimal absorption. That is to say, for the 1-D PC structure CBA71 with large confinement, at the resonance wavelength of 632.8 nm, the scattering loss dominates the value of R_{min} for DI-water ($n_t = 1.333$) but affects R_{min} for air ($n_t = 1.000$) together with the absorption loss from the silicon layer.

In order to verify the explanation, we fabricated several PC-TIR samples with different silicon thickness and silica thickness. Then we measured their reflectance spectra and listed the incident angles for air or water and the R_{min} values when the resonance dip lies at the wavelength of 632.8 nm, as Table 3.4 shows. We found that the R_{min} (for water) is always larger than 0.80, but R_{min} (for air) varies within a large range (0.23 ~ 0.74) for different silicon and silica thicknesses as the defect layers. The results show that the "first coating" PC structures have too strong light confinement so that it is impossible to get a narrow and deep resonance dip at the wavelength of 632.8 nm with the surrounding medium DI-water ($n_t = 1.333$), which is our operative condition of interest for biomolecular detection.

Samples	d_{xSi} (nm)	d_{xSiO_2} (nm)	Air	Air	Water	Water
			θ_i	R_{min}	θ_i	R_{min}
CBA7101	6	290	55.45^o	0.74	61.80^o	0.85
CBA7102	6	336	57.68^o	0.43	62.59^o	0.80
CBA7103	12	380	59.89^o	0.59	63.66	0.86
CBA7104	18	350	58.95^o	0.23	63.15^o	0.84
CBA7105	24	310	57.65^o	0.52	62.46^o	0.81
CBA7106	48	330	60.71^o	0.61	63.77^o	0.84

Table 3.4 Effects of silicon and silica thicknesses on the properties of the PC-TIR sensor using the first coating CBA71 structure.

B. PC-TIR structure based on the second coating

As Figure 3.7 shows above, the "second coating" PC structure has less confinement ability so that it should be more flexible in making a suitable resonance dip than the first coating.

The "second coating" PC structure (marked as CBA72) was composed of pairs of alternating 106-nm TiO_2 and 334-nm SiO_2 layers. We fabricated a PC-TIR structure with a 24-nm Si thin layer as the absorptive layer and a 320-nm SiO_2 layer as the defect layer. Then we measured the reflectance spectrum of the PC-TIR structure when the incident angle in the substrate θ_i was 60.50° and the surrounding medium was air (n_t = 1.0). Figure 3.10 shows a resonant dip *A* at 632.80 nm with $\Delta\lambda$ = 3.20 nm and $R_{\min} = 0.05$. Compared to the result shown in Figure 9 (b), the CBA72 structure with less confinement achieved near zero minimum reflectance but a wider resonance dip width at an even larger incident angle.

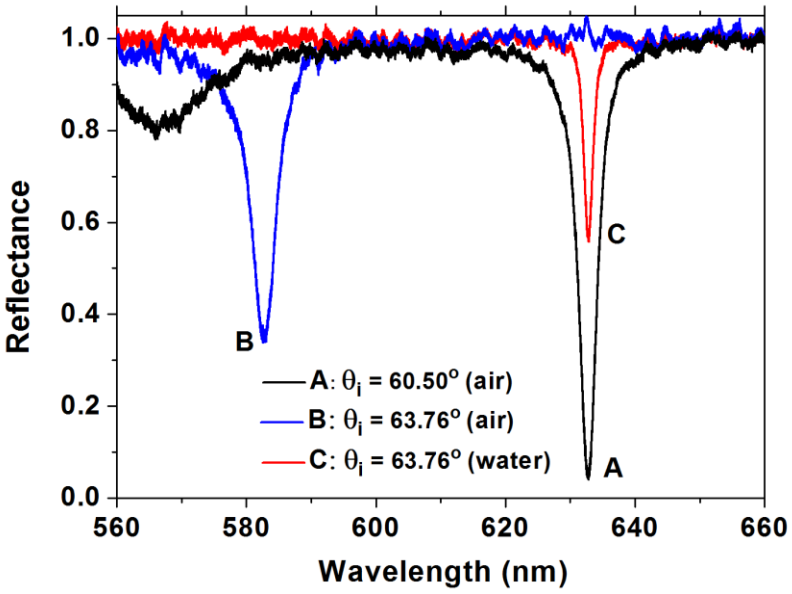

Figure 3.10 Experimental reflectance spectra of the PC-TIR structure with different surrounding medium (air, water) and different incident angles.

When the incident angle θ_i was tuned to 63.76°, the resonance dip (with n_t = 1.0) shifted to the shorter wavelength 582.73 nm, where the PC-TIR structure did not have the optimal absorption any longer and the R_{min} became larger. When the top sensing surface was covered by water instead of air, the resonance dip moved back to the wavelength of 632.8 nm with $\Delta\lambda$=1.60 nm and R_{min} = 0.56. Comparing the resonance dips *A* and *C* in Figure 3.10, clearly, the same PC-TIR structure did not maintain the optimal absorption for n_t = 1.333 but achieved a narrower $\Delta\lambda$ with larger θ_i (i.e., larger light confinement).

In addition, we defined a parameter $\Delta\lambda_{shift}$: the distance between the resonance dip for air and that for water, at the same incident angle for the same PC-TIR structure, e.g., the distance between resonance dips *B* and *C* in Figure 3.10 and a $\Delta\lambda_{shift}$ = 50.07 nm. This parameter can be used to make a simple comparison of the sensitivity of the PC-TIR sensor structure. More accurate characterization methods for the sensitivity of the PC-TIR sensors will be shown in Chapter 4.

With the CBA72 structures, we fabricated several PC-TIR samples with different silicon thickness and silica thickness. Then we measured their reflectance spectra with water on the top sensing surface. Table 3.5 listed the incident angles θ_i, resonance dip width $\Delta\lambda$, minimum reflectance R_{min}, and sensitivity $\Delta\lambda_{shift}$ when the resonance dip was at the wavelength of 632.8 nm. We found that CBA7203 has the narrowest resonance dip and the largest sensitivity with a thinner silicon layer and thicker silica layer; CBA7206 has the broadest resonance dip width and the smallest sensitivity with a thicker silicon layer and thin silica layer. It can be explained by several reasons: 1) the effective refractive index of the defect layer increases so that the sensor sensitivity decreases (as Section 2.5.5 discussed); 2) the incident angle decreases so that the light confinement becomes smaller and thus the resonance dip width broader. As discussed above, the minimum reflectance R_{min} is around 0.50 because the same PC-TIR structure did not have the optimal absorption for n_t = 1.333.

Samples	d_{xSi} (nm)	d_{xSiO_2} (nm)	θ_i	$\Delta\lambda$ (nm)	R_{min}	$\Delta\lambda_{shift}$ (nm)
CBA7201	18	290	62.83°	2.38	0.48	52.97
CBA7202	20	310	63.32°	1.52	0.47	54.78
CBA7203	20	330	63.72°	1.35	0.58	61.22
CBA7204	21	300	63.19°	1.75	0.50	49.78
CBA7205	24	320	63.76°	1.60	0.56	50.07
CBA7206	27	230	62.41°	3.60	0.45	38.72

Table 3.5 Effects of silicon and silica thicknesses on the properties of the PC-TIR sensor using the second coating CBA72 structure.

C. PC-TIR structure based on the third coating

The simulation in Figure 3.7 shows that the third coating (marked as CBA73) has almost the same confinement ability as the second coating. However, we found in experiments that the confinement of the third coating was actually between that of the first coating and that of the second coating. The possible reason might be due to the inaccurate determination of refractive indices and thicknesses of the 1-D PC structures. This is also the reason that we need to test a series of silicon and silica thicknesses (that is, the incident angles) to find out suitable combinations.

As table 3.6 shows, there is no resonance dip for the thick silicon layer ($d_{xSi} = 16nm$), and a thin silicon layer (< 10 nm) is preferred for CBA73 structures. Therefore, the effective refractive index of the defect layer is increased with a thinner silicon layer. In table 3.6, CBA7301 with the thinnest Si layer and the thickest SiO_2 layer achieves the narrowest resonance dip width (~ 1 nm) and the largest sensitivity. In addition, the PC-TIR structure CBA7304 (its reflectance spectrum is shown in Chapter 5) achieves a narrow resonance dip (~ 1.23 nm) with the smallest R_{min} (~ 0.27), which may be due to the low scattering loss in this sample.

Samples	d_{xSi} (nm)	d_{xSiO_2} (nm)	θ_i	$\Delta\lambda$ (nm)	R_{min}	$\Delta\lambda_{\text{shift}}$ (nm)
CBA7301	3	335	63.14^o	1.00	0.56	86.02
CBA7302	4	305	62.56^o	1.64	0.52	69.70
CBA7303	5	330	63.10^o	1.32	0.56	78.64
CBA7304	6	310	62.72^o	1.23	0.27	73.70
CBA7305	10	320	63.06^o	1.77	0.60	74.69
CBA7306	16	310	no dip			

Table 3.6 Effects of silicon and silica thicknesses on the properties of the PC-TIR sensor using the third coating CBA73 structure.

Figure 3.11 shows a typical reflectance spectrum using the "third coating" PC structure. It is surprising to discover that there is an oscillation part on the right side of the resonance dip with $R > 1$. As a matter of fact, the reflectance spectrum was obtained

by normalizing the reflected spectrum of water (as the signal) with that of air (as the source).

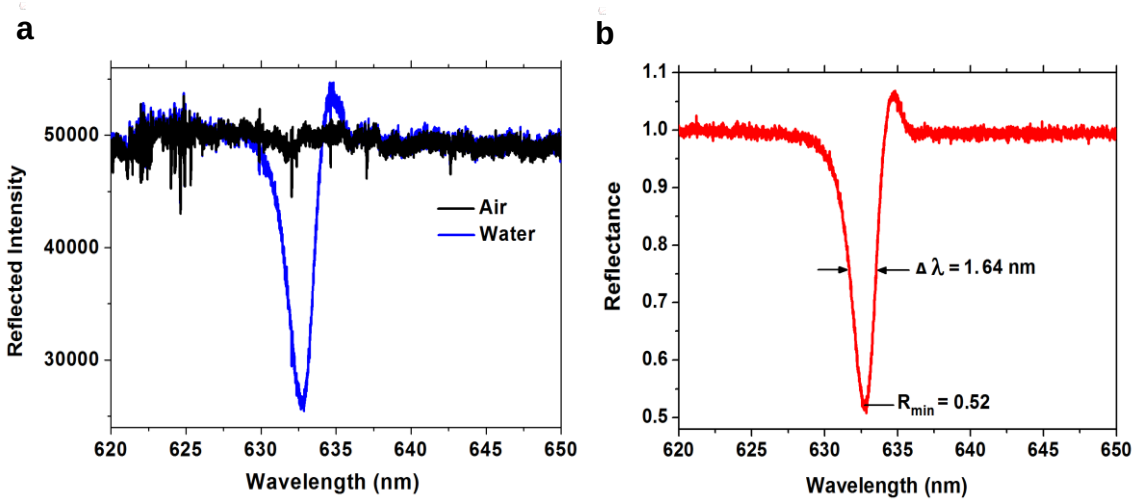

Figure 3.11 Typical experimental spectra using a CBA73 structure: (a) original reflected spectra; (b) normalized reflectance spectrum.

The origin of the oscillation observed was explained by Chuck Divin using the propagation of a leaky mode in the defect layer [80]. As we discussed in Chapter 2, the defect layer functions as a Fabry-Pérot microresonator in the total internal reflection configuration, and the incident light at the resonance wavelength gets trapped in the defect layer, which propagates along one side (as Figure 3.12 shows). This creates a non-symmetric reflected beam profile. After propagating this profile for a certain distance, the oscillation appears on one side.

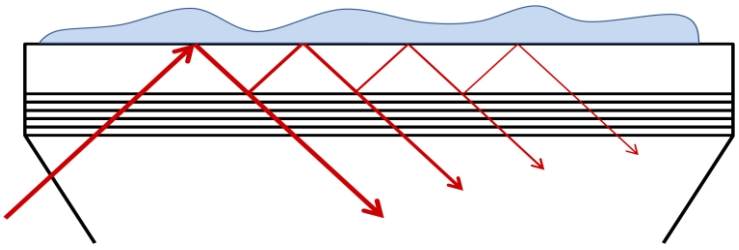

Figure 3.12 Schematic diagram of the trapped light propagating in the defect layer.

This oscillation can be further simulated as the following. In a previous simulation, the incident light was assumed to be a plane wave. However, a Gaussian beam is more accurate to describe the input field, as Figure 3.13 (a) shows. Just after the beam leaves

the PC-TIR sensor structure, the reflected field can be described with the following expression [80]:

$$E_r(x,z) = \int \underbrace{r(k_x)}_{\substack{\text{planewave} \\ \text{reflectivity}}} \underbrace{E_{inc}(k_x)\exp[ik_x x - ik_z z]}_{\text{incident gaussian beam}} dk_x \qquad (3.1)$$

where E_{inc} and E_r present the incident and reflected field; r is the reflectivity of a plane wave; and k_x and k_z are the propagation constants along the *x* and *z* axis.

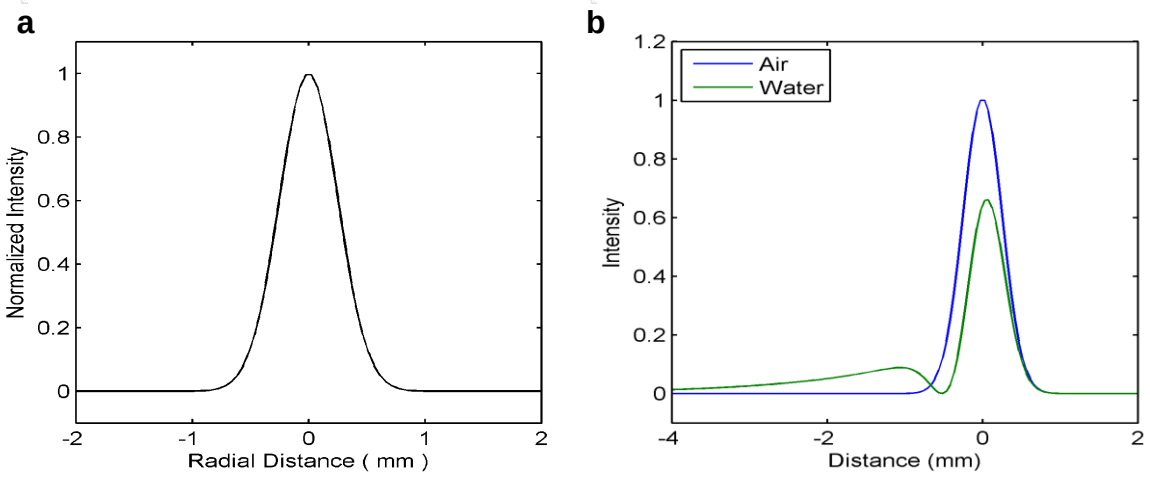

Figure 3.13 The beam profile: (a) just before entering the PC-TIR structure; (b) just after leaving the PC-TIR structure with air or water as the surrounding medium.

Since the incident light gets resonance for water, not for air, only the beam profile of water is modulated by the reflectivity *r*, as Figure 3.13 (b) shows. After propagating a certain distance, the beam profile becomes as Figure 3.14 (a) shows, where the profile is simulated using Fresnel-Kirchoff diffraction (via FFT in Matlab). The reflectivity is obtained by normalizing the beam profile of the water and the air. If we further simulate the reflectance with several wavelengths at the same incident angle, we can get the reflectance spectrum as Figure 3.14 (b) shows. It is very similar to our experimental result shown in Figure 3.11 (b).

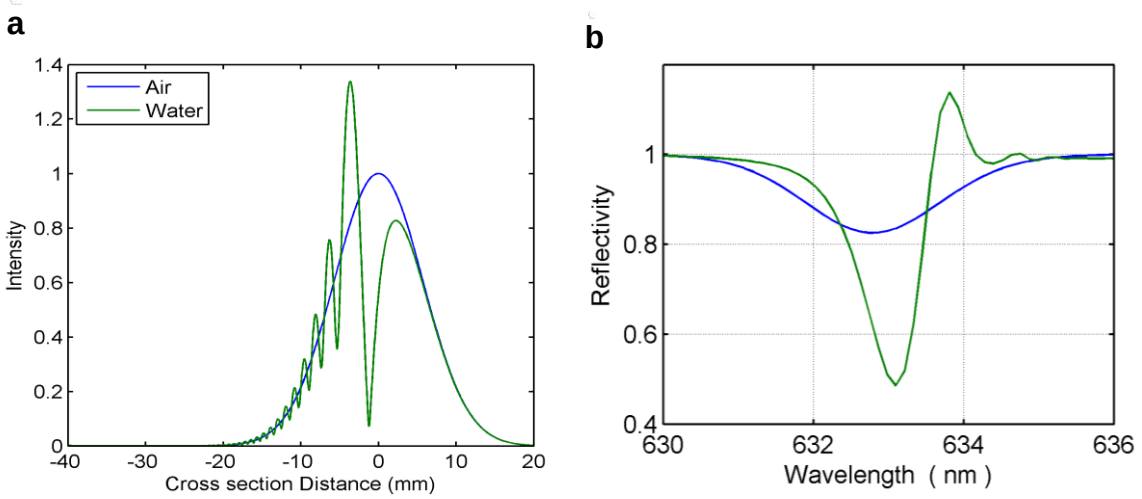

Figure 3.14 (a) The beam profile; (b) the simulated reflectivity, after propagating a certain distance.

However, we didn't observe the oscillation in Figure 3.10 (that is, the second coating samples). The reason may be due to less confinement of the second coating PC structure and larger absorption in the defect layer (thicker silicon film) of the PC-TIR samples, which greatly reduced the propagating distance of the reflected light and thus eliminated the oscillation in the final reflectance spectrum.

3.4 Conclusion

The fabrication of the PC-TIR sensor (that is, the multilayer dielectric structure) is simple, which is one of the big advantages of this technology. However, it is complicated to design and fabricate a suitable structure so that the PC-TIR sensor can achieve a narrow and deep resonance dip for large detection sensitivity. A thorough understanding of the structure parameters is of great help.

In this chapter, I investigated all the parameters of a PC-TIR structure and discussed their effects on the structure properties, both in simulations and in experiments. I proposed a design criterion and fabricated, tested and analyzed three kinds of 1-D PC structures. Due to the effect of scattering loss, the PC structure with less light confinement is preferred in making the PC-TIR sensor, as this provides a larger flexibility in engineering the absorption in the defect layer. In addition, testing a series of absorptions in the defect layer combination of different silicon and silica thicknesses is

very helpful in finding a suitable resonance dip, including small minimum reflectance, narrow resonance dip width, and large sensitivity. If the effective refractive index of the defect layer is smaller (i.e., has less silicon and more silica), the sensitivity will be larger; if the incident angle is larger and the silicon thickness is thinner, the resonance dip width will be narrower. Experimentally, we got the resonance dips with the smallest R_{min} ~ 0 for air and R_{min} ~ 0.23 for water and the narrowest dip width $\Delta\lambda$ ~ 1.00 nm for water.

What is more, we observed an oscillation part in the resonance dip when the light confinement of the PC-TIR structure was large and kept the resonance light propagating as a leaky mode in the defect layer for a certain distance. This phenomenon was well explained by the theoretical analysis and the simulated results.

Chapter 4

Experimental Setup and Sensor Characterization

4.1 Introduction

A photonic crystal-total internal reflection (PC-TIR) biosensor consists of a PC-TIR structure and an optical platform in which an optical resonance mode is formed and interrogated and the biomolecular binding between the ligand immobilized on the sensing surface of the structure and the target analyte in a liquid solution is measured. The PC-TIR biosensor also incorporates a fluidic system that usually consists of a flow cell confining the sample solution on the sensing surface.

In previous chapters, we have discussed the design and fabrication of a suitable photonic PC-TIR sensor structure to get a deep and narrow resonance mode for high detection sensitivity. In this chapter, we discuss building an integrated optical platform and analyzing the system noise. Moreover, we explore the optical properties of the PC-TIR biosensor and experimentally characterize its sensitivity regarding bulk solvent refractive index change, thin molecular films adsorption, and real-time analyte binding. Finally we compare the performance of the PC-TIR biosensor with that of a state-of-the-art surface-plasmon-resonance (SPR)-based biosensor.

4.2 Experimental Setup and System Noise

4.2.1 Experimental setup

As we discussed in Chapter 2, section 2.4, spectroscopy (angular or wavelength) modulation and intensity modulation are usually employed to monitor the resonance mode shift. The former provides a large detection range but limited detection resolution; the latter provides high detection resolution but a limited detection range. Considering the

unique properties of the PC-TIR sensor (broad bandgap for resonance shift and narrow resonance dip), we constructed an integrated optical system which combined both white light spectral measurement and normalized laser intensity measurement. In addition, there are several ways to couple light into biosensors [18], including prism coupling, grating coupling, fiber coupling, waveguide coupling, and more. Here we chose prism coupling, which is convenient and can be realized with simple and conventional optical elements.

Briefly, for normalized intensity measurements, a collimated *s*-polarized HeNe laser beam with a wavelength of 632.8 nm was apodized with a 1-mm pinhole to set the size of the probe beam. After that, the laser beam was split into two by a non-polarized beam splitter, propagating in parallel and hitting two different areas on the surface of the PC-TIR sensor. Using simple optical mounts, the incident angle of these two beams was adjusted until the laser wavelength lay at the steepest portion of the resonance dip. Dual flow channels formed in polydimethylsiloxane (PDMS) were used to isolate the two areas on the sensor surface, so that one area was used for binding of the analytes, while the other contained only flowing buffer to serve as a reference. The intensity of the signal and reference beams was detected with two identical photodiode detectors (DET36A) from Thorlabs (Newton, NJ) and recorded with an 18-bit data acquisition card (PCI-6281) from National Instruments (Austin, TX). The intensity ratio was obtained by directly normalizing these two reflected intensities of the signal and reference beams at a 1-Hz rate. A corresponding LabVIEW control program was developed to retrieve and record the data by Chuck Divin.

For spectral measurements, a broadband incandescent lamp was used as a white light source. The beam was coupled with an objective lens into a single-mode optical fiber to obtain a good spatial beam profile and was collimated with another objective lens. The collimated white light travelled the same path as the laser beam except that the reflected light was directly detected using a spectrometer (model number iHR 550) from HORIBA Jobin Yvon Inc. (Edison, NJ).

These two measurements could be switched easily by moving a mirror (i.e., M2), which enabled us to monitor the binding events by measuring resonance wavelength shift directly with the spectrometer or using a normalized intensity ratio with high precision.

The PC-TIR sensor was mounted on a prism (made of BK7 glass) via refractive index matching liquid from Cargille Labs (Cedar Grove, NJ) and was stabilized, and the top surface was attached to a fluidics cell with two parallel flow channels made of PDMS; the solutions were introduced by withdrawing syringes through a pump from KD Scientific Inc. (Holliston, MA), and the flow rate could be adjusted over a large range (1 nL/min to 1.00 mL/min).

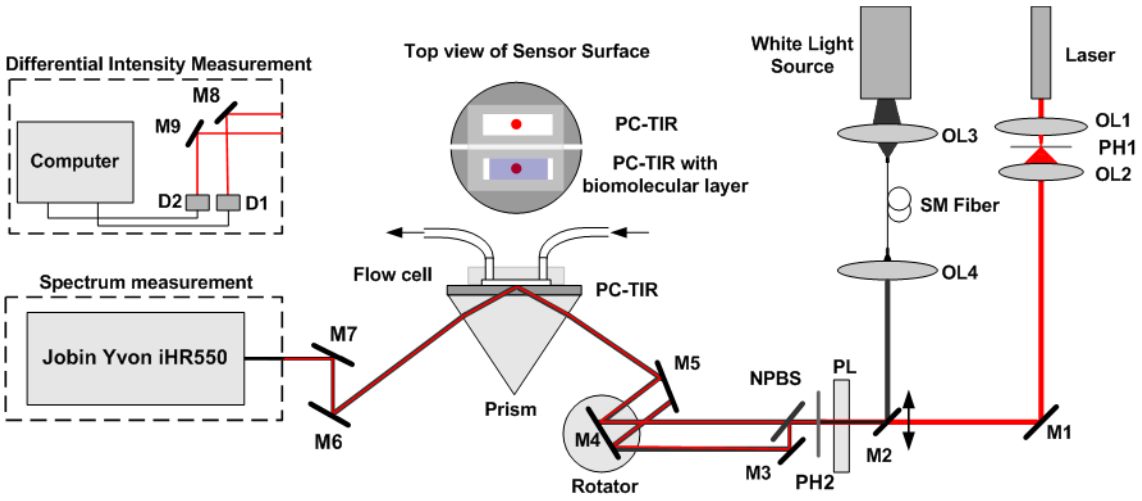

Figure 4.1 Experimental setup for spectral and normalized intensity measurements. OL1-OL4: objective lenses; SM fiber: single mode fiber; PH1-PH2: pinhole; PL: polarizer; NPBS: Non-polarizing beam splitter; M1-M9: reflecting mirrors; D1-D2: photodiode detectors.

4.2.2 System noise

Similar to SPR-based systems, our present experimental setup is characterized by a short-term noise floor and a long-term drift limited by the mechanical stability of the system, respectively. As Figure 4.2 shows, the fluctuation of the signal channel was 2.9×10^{-3} (1.9×10^{-3} over 0.66660), about 400 times larger than that of the intensity ratio 7.3×10^{-6} (5.7×10^{-6} over 0.781782). It means that the normalized intensity measurement can greatly suppress the noise floor. Over a typical molecular binding period (~ 5 minutes), with a 1-Hz signal bandwidth, both the normalized reflectance noise floor (i.e., standard deviation) and long-term drift are below 7.3×10^{-6}. The resonance wavelength shift can be derived from the intensity ratio change with a Lorentz equation (as discussed in section 4.4.2). Figure 4.2 (c) shows that the baseline fluctuation of the corresponding

resonance wavelength shift was 1.6×10^{-5} nm, which could be considered as the minimum detectable signal (i.e., detection resolution) of the PC-TIR biosensor.

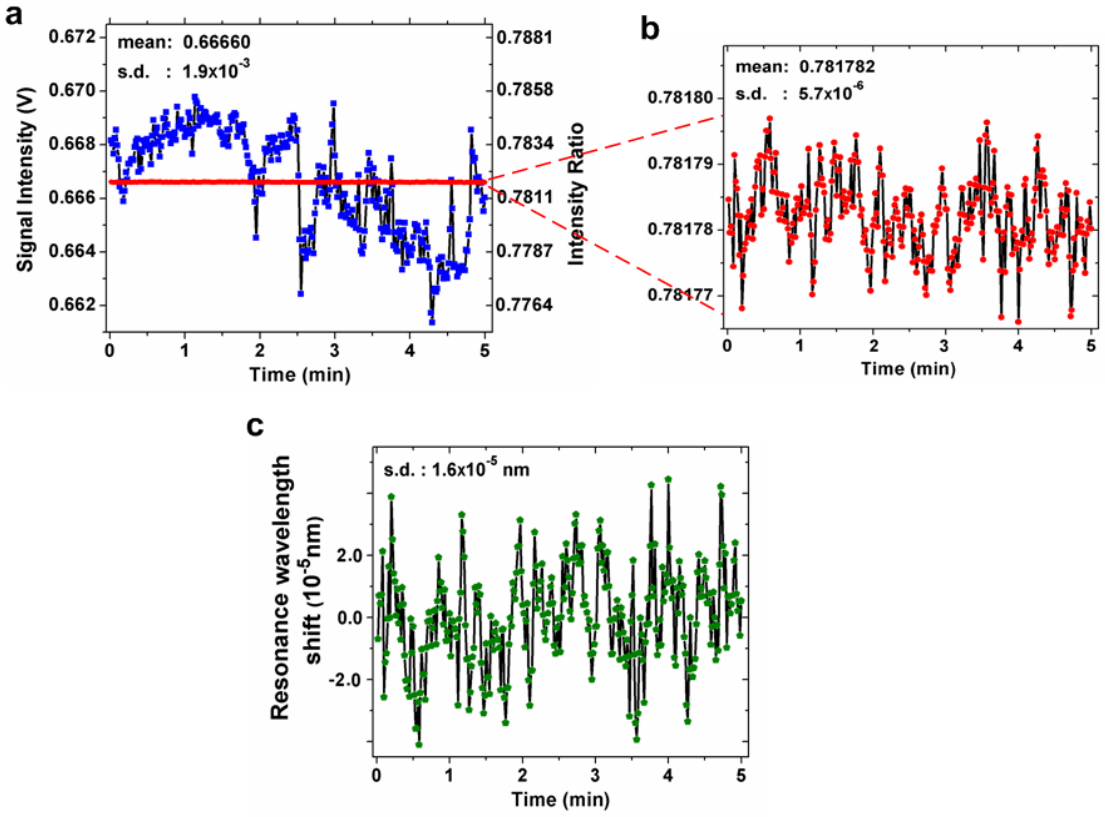

Figure 4.2 Baseline noise floor of the PC-TIR sensor. (a) Baseline fluctuations of the signal channel intensity and of the intensity ratio between signal and reference channels; (b) baseline fluctuation of the intensity ratio; (c) the corresponding resonance wavelength shift of the noise floor.

As we discussed in section 1.2.2, the detection limit of label-free biosensors depends on the sensor sensitivity and the level of uncertainty of the sensor output (i.e., the baseline noise floor). If we could lower down the sensor noise, the detection limit can be significantly improved. In order to achieve this, we analyzed the noise sources of the presented system as follows.

The PC-TIR sensor output is the intensity ratio *r(t)* between the reflected intensity from the signal channel I_{sig} *(t)* and that from the reference channel I_{ref} *(t)*, which can be expressed as:

$$r(t) = \frac{I_{sig}(t)}{I_{ref}(t)} = \frac{I_{sig0}(1+\delta I_{sig})}{I_{ref0}(1+\delta I_{ref})} \bullet \frac{1+\frac{\partial I_{sig}}{\partial \lambda_{sig}}\delta\lambda_{sig}}{1+\frac{\partial I_{ref}}{\partial \lambda_{ref}}\delta\lambda_{ref}} \qquad (4.1)$$

where I_{sig0} and I_{ref0} are the steady-state reflected intensities from the signal and the reference channels; δI_{sig} and δI_{ref} are the fluctuations due to laser intensity, light scattering, etc.; $\delta\lambda_{sig}$ and $\delta\lambda_{ref}$ are the fluctuations of resonance wavelength shifts of the signal and reference channel; and $\partial I_{sig} / \partial \lambda_{sig}$ and $\partial I_{ref} / \partial \lambda_{ref}$ present the slopes of the resonance dips of the signal and reference channels at the wavelength of the input laser light.

Obviously, the normalized intensity ratio *r(t)* is affected by several noise sources, including fluctuation of the laser intensity, the drift of the resonance wavelength (due to temperature fluctuations, etc.), the different optical paths of the two reflected beams, the non-uniformity of the sensing surface of the signal and reference channels, the statistical properties of light (shot noise), and noise generated in the electronic circuitry of the detectors, etc.

Normally the fluctuation of the intensity from a HeNe laser source is > 1%. A high intensity-stabilized single wavelength laser will definitely improve the performance of the PC-TIR sensor. In addition, a spatial filter can also be used to get a high-quality laser mode and may reduce the intensity fluctuation to be below 10^{-3}.

Temperature fluctuation is the most commonly seen noise for a refractive index (RI)-based label-free biosensor. It results in a thermo-optic effect (i.e., temperature-dependent RI changes) in both the sensor substrate and the buffer solution. The refractive index of water is known to decrease by ~ 1×10^{-4} *RIU/K* near room temperature [63], and the fused silica is 6.4×10^{-6} *RIU/K* [81]. Ignoring the relatively small changes associated with temperature effects on the sensor structure, the slope of the resonance wavelength shift of the PC-TIR sensor (with a bulk solvent refractive index sensitivity ~ 1500 *nm/RIU*) due to the temperature fluctuation is 0.15 *nm/K*. In order to achieve the level of 1.6×10^{-5} nm shown in Figure 4.2 (c), the temperature of the liquid must be controlled to better than 10^{-4} *K* over the time scale of measurements if without a reference channel. A

general approach to reducing the thermally induced noise is to implement a temperature control system to stabilize temperature.

Besides the methods mentioned above, the most efficient way is to use a reference [74]. Here we normalized the reflected intensity between the signal and reference channel, which dramatically reduced the noise from the laser intensity instability or the temperature fluctuation. However, it requires a uniform sensing surface. If the surface is not uniform, the signal and the reference part may have different resonance dips and may respond differently to the fluctuations of the resonance wavelength, as Equation 3.1 shows.

In addition, besides one channel with ligand adsorption as the signal channel and the other with buffer as the reference channel, if there is a third one with a blocking agent as the control channel, we can get a real control for the analyte solution when we follow the same analyte solution over two signal and control channels simultaneously. The reflected intensities from both the signal and the control channels are normalized by that from a third reference channel. Subtracting the binding curve from the control channel from that from the signal channel, we will obtain the real-time curve for the analyte binding to the ligand and additionally the kinetic constants, which also can further improve the quality of the biomolecular detection by correcting for artifacts such as bulk refractive index changes, nonspecific binding, injection noise, and baseline drift [74].

Therefore, the noise floor of the presented PC-TIR system could be further decreased by improving the quality and uniformity of the sensor structure, by adding one more control channel for double reference, by controlling temperature stabilization, and by decreasing the laser fluctuation.

4.3 Characterization of the PC-TIR Sensor

In order to demonstrate the operation of the PC-TIR sensor system, we measured the optical properties of the PC-TIR sensor and performed a series of experiments to characterize its detection sensitivity: bulk solvent refractive index changing, thin molecular layer adsorption, and real-time analyte binding.

4.3.1 Resonance dip

The PC-TIR structure tested here was composed of the second coating of the 1-D structure (that is, pairs of alternating 106-nm TiO_2 and 334-nm SiO_2 layers). An 18-nm Si thin layer was used as the absorptive layer and formed the defect layer with a 320-nm SiO_2 layer.

Figure 4.3 (a) shows the reflectance spectra of the PC-TIR sensor when the incident angle in the substrate was 63.52° and the top sensing surface was covered by de-ionized (DI) water. The reflectance dip is in reasonable agreement with a simulation using a transfer matrix calculation; it has a resonance wavelength λ_r of 632.80 nm, a width $\Delta\lambda_r$ of 1.35 nm, and a small minimum reflectance R_{min} of 0.50. Although the resonance width is slightly larger than the simulated value of 0.60 nm due to the non-uniformity of the deposited thin films and the nonzero divergence of the probe beam, it is much narrower than that of a typical SPR resonance (a few tens of nm) and allows more sensitive detection of resonance shifts. Moreover, the reflectance spectrum near the resonance can be reasonably well fit by a Lorentzian lineshape, similar to a Fabry-Pérot mode.

Of course, a better resonance dip (with narrower $\Delta\lambda_r$ and smaller R_{min}) can be achieved by further optimizing the parameters of the PC-TIR structure and improving the uniformity and quality of the deposited dielectric layers.

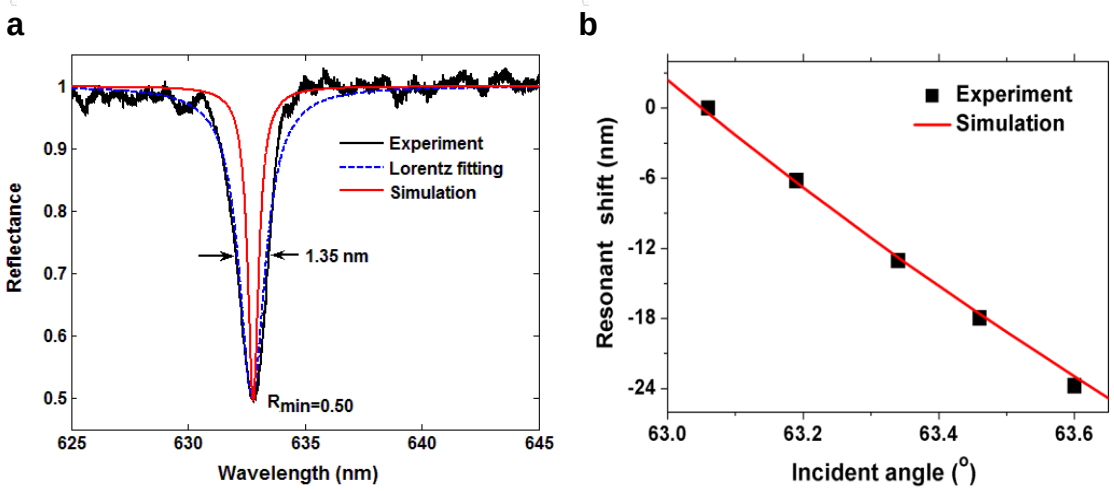

Figure 4.3 (a) Experimental, simulated and Lorentz fitting reflectance spectra of the PC-TIR sensor; (b) the resonant wavelength shifts with incident angle changing.

4.3.2 Angular sensitivity

When the incident angle changes, the resonant wavelength shifts in order to satisfy the resonant condition (Equation 2.20). Figure 4.3 (b) shows that the experimental data has a good agreement with the transfer matrix simulated results, and the angular sensitivity of the PC-TIR sensor is −43.9 nm per degree, which can be further increased by improving the sensitivity of the PC-TIR sensor (for example, reducing the effective refractive index of the defect layer). By adjusting the incident angle, we can tune the resonance mode to the desired wavelength. For the experiments reported in this dissertation, the incident angle is usually adjusted to shift the steep portion of the resonance dip to the HeNe laser line at 632.80 nm.

4.3.3 Bulk solvent refractive index sensitivity

In Section 2.4.4, we derived the sensitivity expression for biomolecular binding. As a matter of fact, the PC-TIR sensor is an evanescent wave-based sensor and is also sensitive to the bulk solvent refractive index change. Its sensitivity is determined by the fraction of light in the solution or the light intensity at the sensor, which can be used to roughly compare the sensing capability among different optical technologies and structures (as mentioned in section 1.2.1).

From the resonant condition of the PC-TIR sensor–Equations (2.20) and (2.21)–we can derive the relationship between the shift of the resonance wavelength and the change of the bulk solvent refractive index, and the sensitivity S_{sol} is expressed as

$$S_{sol} = \frac{\partial \lambda_R}{\partial n_t} = \frac{\partial \lambda_R}{\partial \alpha_S} \bullet \frac{\partial \alpha_S}{\partial n_t} = \frac{{\lambda_R}^2 n_t}{2\pi d_x ({n_x}^2 - {n_t}^2)\sqrt{n_S^2 \sin^2 \theta_S - n_t^2}} \qquad (4.2)$$

where the parameters are defined as the same as those in Chapter 2. This equation indicates: 1) the resonant wavelength shifts to a longer wavelength with larger n_t; 2) reducing the effective refractive index n_x can increase the sensitivity; 3) decreasing the incident angle also can increase the sensitivity.

In our experiments, the bulk solvent refractive index sensitivity (BRIS) S_{sol} is characterized by a series of different concentrations of ethylene glycol solution in de-

ionized (DI)-water. Progressively higher concentrations were flowed over the sensing surface. As Figure 4.4 shows, a shift to a longer resonance wavelength was observed in response to the refractive index increasing on the sensing surface, and the experimental data fit well with the simulation results. A sensitivity of 1490 *nm/RIU* was then obtained by measuring the slope of the resonant wavelength shift versus RI change.

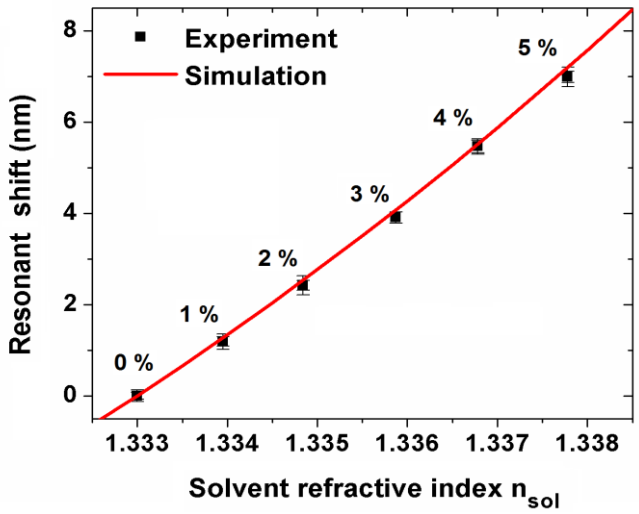

Figure 4.4 Resonance wavelength shifts with different concentrations (i. e., different refractive indices) of ethylene glycol solutions in DI-water (0% to 5%) on the sensing surface.

As we mentioned above, there are two detection methods. The spectrum measurement is limited by the available spectrometer resolution. For example, the spectrometer resolution is 0.025 nm, so the detection limit for the bulk solvent refractive index of our PC-TIR sensor is 1.7×10^{-5} RIU. Certainly, the detection resolution may be further improved a little bit by using Lorentz fitting or other data processing to find the position of the resonance wavelength. However, the normalized reflectance measurement can achieve a much higher sensitivity (thus a much lower detection limit).

In order to demonstrate this, we adjusted the incident angle so that the HeNe wavelength was at the long-wavelength, half-maximum point in the resonant dip, and then 0% to 1% ethylene glycol solutions were flowed over the sensing surface consecutively with a rinsing step between each new concentration to ensure the surface was cleaned before the next measurement. The real-time normalized intensity ratio was measured and a much larger signal change was obtained and shown in Figure 4.5 (a).

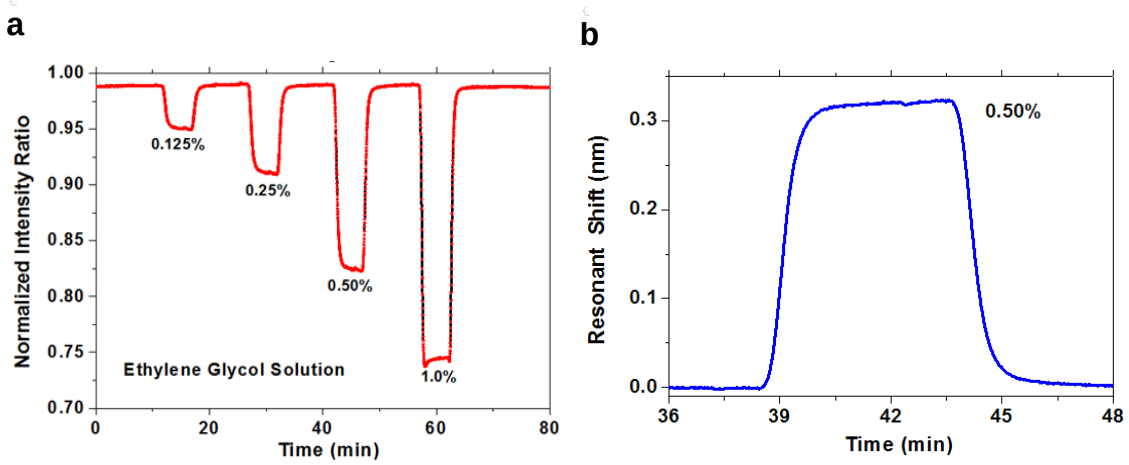

Figure 4.5 (a) Normalized differential ratio with different concentrations of ethylene glycol solution; (b) transformed resonant wavelength shift with flowing 0.50% ethylene glycol solution.

There are two ways to measure the resonant wavelength shift with the bulk solvent refractive index changing or with molecular binding. One is to make use of the linear region of the resonant dip [72, 73]. For example, the refractive index of 0.5% ethylene glycol solution is 5×10^{-4} RIU larger than that of DI-water, and the ratio change is 0.16439. Taking the noise floor 7.3×10^{-6} for the normalized intensity ratio as the smallest detectable signal, the detection limit (*DL*) for the bulk solvent refractive index is

$$DL_{sol} = \frac{\delta R}{\Delta R} \bullet \Delta n = \frac{7.3\times10^{-6}}{0.16439} \bullet 5\times10^{-4}\, RIU \approx 2.2\times10^{-8}\, RIU \qquad (4.3).$$

The other is to map the normalized intensity ratio change to the reflected intensity change and thus transform to the resonance wavelength shift directly by the reversed Lorentz formula (Equation 4.4), as the resonant dip can be well fitted by a Lorentzian lineshape (as shown in Figure 4.3a).

$$\Delta\lambda_{\text{Res.}} = \lambda_{\text{Res.}} - \lambda_0 = \left(\lambda_{Laser} \mp \frac{\Delta\lambda}{2}\sqrt{\frac{R-R_{\min}}{1-R}} \right) - \lambda_0 \quad (\lambda_{\text{Res.}} < \lambda_{Laser} \ \ or > \lambda_{Laser}) \qquad (4.4).$$

The latter makes it easier for us to determine the bulk solvent refractive index change or molecular binding in real time and also increases the detection range to both sides of the resonance dip, compared to the former, which is only able to monitor one side. Figure 4.5 (b) shows the data transformed into the resonant wavelength shift, and the final shift is 0.32271 nm for the bulk solvent refractive index change of 5×10^{-4} RIU.

Taking the noise floor 1.6×10^{-5} nm for the resonant wavelength shift as the smallest detectable signal (Figure 4.2c), the detection limit for the bulk solvent refractive index can be calculated to be

$$DL_{sol} = \frac{\delta\lambda}{\Delta\lambda} \bullet \Delta n = \frac{1.6\times10^{-5}}{0.32271} \bullet 5\times10^{-4}\, RIU \approx 2.5\times10^{-8}\, RIU \qquad (4.5),$$

which is almost the same as that obtained by Equation (4.3).

4.3.4 Thin molecular layer detection

In order to characterize the high sensitivity of the PC-TIR sensor for biomolecular binding, we used two coupling agents, aminopropyltriethoxysilane (APTES) and glutaraldehyde, which can form uniform thin layers on silica surfaces [31]. The sensing surface was first cleaned by a piranha solution (H_2SO_4 [95%] / H_2O_2 [30%] = 3:1) and then exposed to 5% APTES in a DI water and methanol (1:1) solution for 20 minutes, then rinsed with DI water and dried with air. After the silanization, a thin layer of APTES molecules formed on the sensing surface. Then the sensor was exposed to a 2.5% glutaraldehyde solution in 20 mM HEPES buffer (pH=7.4) for 30 minutes and rinsed with DI water and dried with air. A thin layer of glutaraldehyde molecules was adsorbed on the surface due to the reaction with the amino groups on the silanized surface.

We performed spectroscopic ellipsometry measurements on a separate substrate (a crystalline p-type silicon wafer with a thin, thermally oxidized layer of thickness 4.93 ± 0.02nm) to provide an independent determination of the layer thicknesses; we found the APTES monolayer and APTES/glutaraldehyde bilayer to be 0.55 ± 0.04 nm and 1.31 ± 0.04 nm, respectively, assuming the refractive indices of APTES and glutaraldehyde to be 1.46 [31].

The resonance shift of the PC-TIR sensor (CBA7203 shown in Table 3.5) as the layers were adsorbed was first observed by measuring the reflectance spectrum. The results, shown in Figure 4.6 (a), revealed resonant wavelength shifts of 0.52 and 1.18 nm, respectively, as the APTES monolayer and APTES/glutaraldehyde bilayer were formed. Their physical thicknesses adsorbed on the sensing surface were calculated to be 0.62 nm

and 1.39 nm from the transfer matrix simulation, which were in approximate agreement with the ellipsometry measurement.

In addition, the normalized intensity ratio change was observed. Taken as a reference point, the ratio for the bare PC-TIR sensor changed from 1.00000 to 0.77814 for the binding of an APTES monolayer (data in Figure 4.6 b). Similarly, taking the noise floor 7.3×10^{-6} as the smallest detectable signal, the detection limit of the PC-TIR sensor for analyte layer thickness is thus estimated to be 0.55 nm $\times(7.3\times10^{-6}/0.22186) \sim 2\times10^{-5}$ nm. This thickness detection limit corresponds to a 10^{-4} monolayer [63].

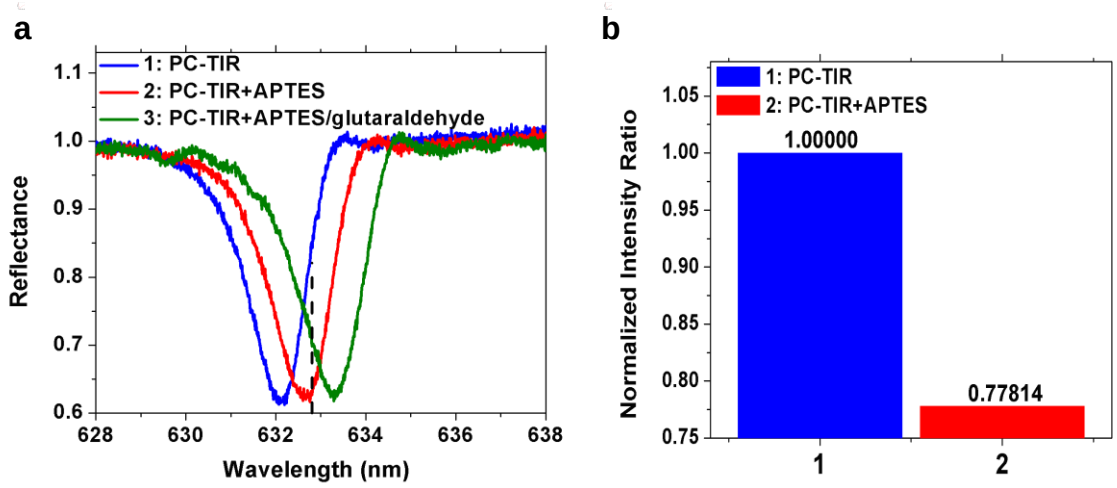

Figure 4.6 (a) Resonance dip wavelength shifts with the binding of an adlayer; (b) normalized intensity ratios at 632.8 nm from normalized intensity measurement for a PC-TIR sensor without treatments and with an APTES monolayer.

4.3.5 Real-time analyte binding

We have evaluated the performance of the PC-TIR sensor with bulk solvent refractive index sensitivity and thin film adsorption. However, the most important application of label-free biosensors is biomolecular binding detection, where the surface mass density (or total mass) in units of pg/mm^2 (or pg) is actually measured.

Here the well-studied biotin-streptavidin system with its extremely high binding affinity ($K_d \sim10^{-15}$ M) was chosen to illustrate the attributes of the PC-TIR sensor. The biotin-streptavidin system has been studied in great detail and serves as an excellent model system for biomolecular recognition.

Figure 4.7 (a) shows the schematic diagram of surface functionalization. To create a biotinylated surface for capturing streptavidin (SA), the sensing surface (silica) was first cleaned and oxidized by the piranha solution (H_2SO_4 (95%) / H_2O_2 (30%)=3:1), then silanized with 5% APTES solution in methanol/ water (1:1). Next, Sulfo-NHS-LC-LC-Biotin (1 mg/mL in PBS) was slowly flowed over the silanized sensing surface for several hours so that the NHS-activated biotin reacted efficiently with the primary amino groups to form stable amide bonds. After that, 0.5 mg/mL bovine serum albumin (BSA) in PBS was flowed to block the non-specific binding sites of the streptavidin protein with the silica sensing surface.

After surface functionalization, PBS buffer was flowed continually over the sensing surface for a sufficient time to get a stable baseline. At time zero, 1 μg/mL streptavidin solution in PBS was injected into the flow cell with a flow rate of 100 μL/min, and then washed by PBS. This procedure was monitored in real time. In Figure 4.7 (b), one can see that the resonant wavelength shift was increasing with more and more streptavidin molecules binding to the biotinlyated sensing surface. After flowing the streptavidin solution for 10 minutes, we changed to PBS buffer, which removed the remaining streptavidin solution from the sensing surface. Only a small bulk solvent effect was observed and there was no dissociation, which indicated that the streptavidin was tightly bound to the biotinylated sensing surface due to their high affinity. The difference between the original baseline and the new baseline was 0.54 nm, which was entirely due to the streptavidin's adsorption onto the sensing surface via specific binding.

Assuming that the refractive index of the streptavidin is 1.45, its effective physical thickness adsorbed on the sensing surface is 0.60 nm by a transfer matrix simulation, which is about 10% of that of the streptavidin monolayer [73, 82]. This corresponds to 10% of the typical streptavidin saturation coverage, or an average packing density of 2.4×10^{9} molecules/mm^2 [73, 82]. Since the PC-TIR sensor can resolve a resonant wavelength shift down to 1.6×10^{-5} nm, the 0.54-nm streptavidin layer in the experiment was detected with an ultimate signal-to-noise ratio of 3.4×10^{4}. Therefore the minimal density that can be measured by the PC-TIR sensor is 7×10^{4} molecules/mm^2, which corresponds to a mass density detection limit of 6 *fg/mm*^{2} for streptavidin molecules (MW ~ 52,000 Da).

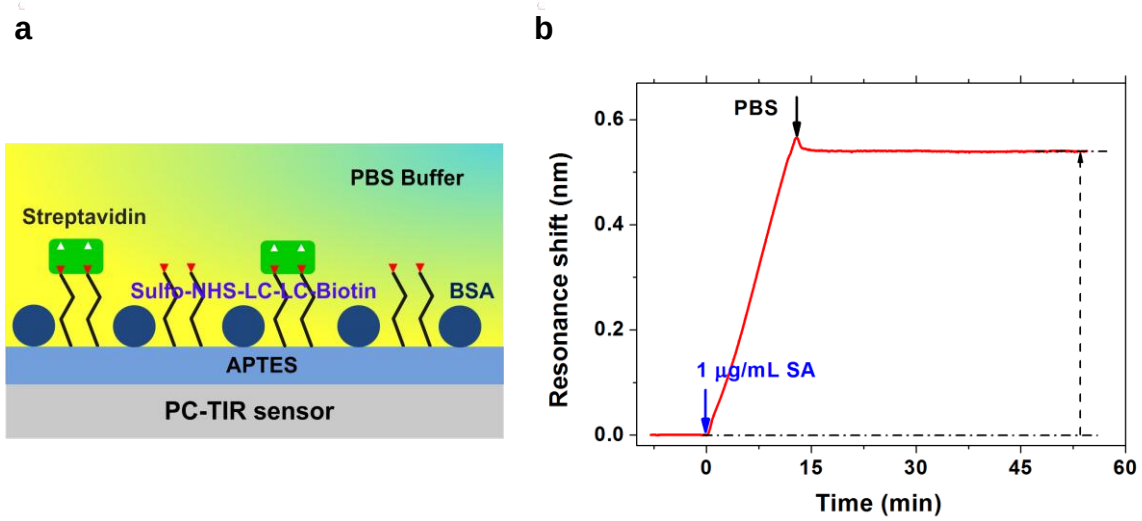

Figure 4.7 (a) Schematic diagram of surface functionalization and biomolecular interaction; (b) real–time streptavidin binding to biotinlyated sensing surface.

4.4 Conclusion

As introduced in Chapter 1, SPR-based biosensors have become the dominant optical tools for biomolecular interaction studies. Although sophisticated engineering has improved the performance of commercial SPR-based systems, inherently improving the sensor's sensitivity is still the key to further advances.

The sensitivity of an optical biosensor can be characterized in a number of ways, depending on the applications. However, an important and inherent comparative parameter of sensing devices is the figure of merit (FOM), as defined in section 1.2.1. For conventional SPR-based sensors, FOM = 23; for localized surface plasmons, FOM = 8 [83]. The newly-developed sensor system based on plasmonic nanorod metamaterials benefits from both an increase in the bulk refractive-index change and the larger sensing area of the nanorod metamaterials matrix and achieves an order of magnitude higher sensitivity (30,000 nm/RIU) than conventional SPR sensors [16]. Its figure of merit reaches 330. In contrast, the PC-TIR sensor in Figure 4.3 (a) achieved 1490 nm/ RIU sensitivity and 1.35 nm resonance width, thus its FOM is ~ 1100. The FOM value of the PC-TIR sensor can be further improved by optimizing the parameters of the structure. The sensor shown in Figures 5.1 and 5.2 achieved a FOM value of ~ 1500. This

comparison shows that the PC-TIR sensor is inherently much more sensitive than SPR-based sensors.

With a much narrower resonance mode, the PC-TIR sensor can greatly benefit from the normalized intensity measurement instead of the spectroscopy modulation that is widely adopted in SPR-based systems. We have successfully built an integrated experimental setup and characterized its high sensitivity: a bulk solvent refractive index sensitivity of ~10^{-8} RIU (refer to Figure 5.2), a thin molecule layer adsorption sensitivity of 2×10^{-5} nm, and a surface mass density sensitivity of 6 fg/mm^2, which are several orders of magnitude higher than those of an SPR-based system (Table 4.1).

Sensor	FWHM	Detection limits		
		Solvent RI	Thickness	Mass density
PC-TIR	$\Delta\lambda \sim 1$ nm	~10^{-8} RIU	2×10^{-5} nm	6 fg/mm^2
SPR	$\Delta\lambda \sim 40$ nm[17]	5×10^{-7} RIU [84]	3×10^{-3} nm [63]	0.5 pg/mm^2 [20]

Table 4.1 Comparison between PC-TIR and SPR sensors

In the following Chapter 5, we further demonstrate the capability of the PC-TIR sensor for biomolecular binding detection–especially for small molecule detection–and show its great potential to be a highly sensitive analytical system for biomedical and pharmaceutical research.

Chapter 5

Highly Sensitive Biomolecular Binding Detection

5.1 Introduction

The study of biomolecular binding affinity and kinetics, such as protein-protein binding, the binding of small molecules and drugs to biological targets, or evaluations of DNA hybridization, provides insights into fundamental biological processes and serves as the basis for diagnostic and drug discovery applications. For measurements of very small molecules (with molecular weights of 500 *Da* or below) and/or at very low concentrations (within the *fM ~ nM* range), biomolecular detection usually requires labeling (such as fluorescent tags); however, the conjugation of these tags may alter or inhibit the functionality of the target molecules. In contrast, label-free based detection provides more accurate quantitative and kinetic measurements by monitoring the binding of analytes in their natural forms. A number of sensing technologies [11], including interferometry, plasmon sensing, nanowires [85], waveguides, microcavity resonators and photonic crystals, have been developed, but the direct detection of small molecule binding still remains challenging.

In previous chapters, I have shown the development of a novel photonic crystal-total internal reflection (PC-TIR) biosensor including the principle, design, fabrication, and experimental setup, and have demonstrated its ultrahigh sensitivity with normalized intensity measurement, more than one order of magnitude higher than SPR-based systems. In this chapter, I will step by step explore the capability of the PC-TIR sensor for making highly sensitive measurements of biomolecular interactions, especially for small molecule detection, which is an inherently difficult application for label-free optical sensors.

I first characterize the sensitivity of a PC-TIR sensor with bulk solvent refractive index change and then use the well-studied biotin-streptavidin system to calibrate the detection limits for molecules with different molecular weights (MWs). Methods for effective immobilization of a binding layer of streptavidin on the silica sensing surface are discussed. The specific binding of biotinylated analyte molecules ranging over three orders of magnitude in molecular weight, including very small molecules, DNA oligonucleotides, proteins, and antibodies, is monitored in real time. Finally, I document the sensor efficiency for multilayered molecular interactions.

5.2 PC-TIR Sensor and Sensitivity

The detection system performance is greatly dependent on the PC-TIR sensor structure, so it is necessary to choose and characterize the sensor sensitivity before running any biomolecular detection experiments on it. In the following experiments, the PC-TIR sensors were made on the third batch of 1-D PC structures: substrate/TiO_2 /$(SiO_2/TiO_2)^3$, where the TiO_2 layer thickness was 107 nm and the SiO_2 layer was 330 nm. As discussed in Chapter 3.3.4 (c), this coating of 1-D PC structures had large light confinement, so the absorption needed to achieve a deep resonance dip was small. Here I chose 6-nm Si thin layer as the absorptive layer, which formed the defect layer with another 310-nm SiO_2 layer on top of the structure. Figure 5.1 shows the PC-TIR sensor structure and reflectance spectra when the incident angle in the substrate was 62.72^o and the top sensing surface was covered by DI water. The reflectance dip was in reasonable agreement with a simulation using a transfer matrix calculation. It had a resonance wavelength of 632.8 nm and a narrow resonance width $\Delta\lambda$ of 1.23 nm and small minimum reflectance R_{min} of 0.27. Moreover, the reflectance spectrum near the resonance can also be well fit by a Lorentzian lineshape.

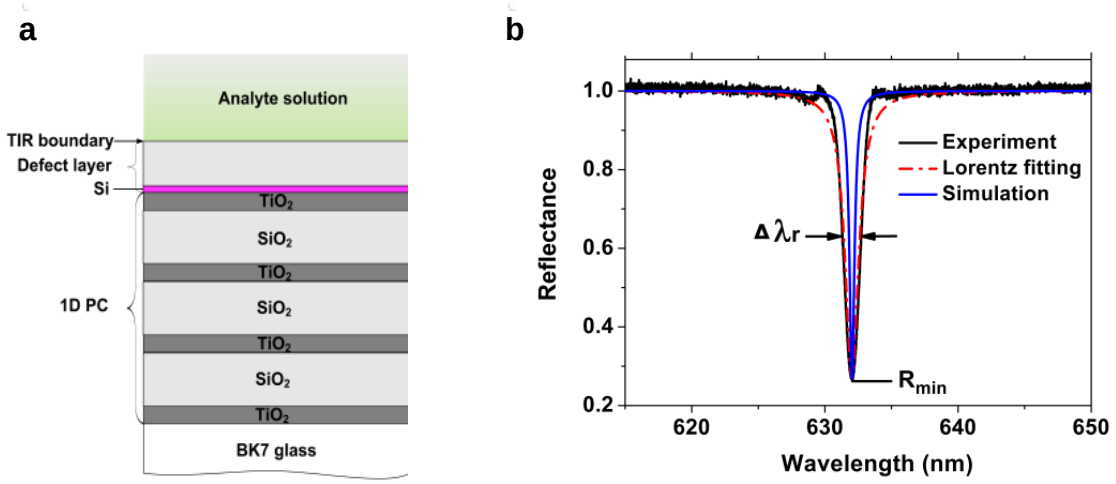

Figure 5.1 PC-TIR sensor structure and reflectance spectrum. (a) The schematic structure of the 1-D PC-TIR sensor; (b) the experimental, Lorentzian fitting, and simulated reflectance spectra of the PC-TIR sensor.

Prior to the biomolecular detection experiments, we calibrated the PC-TIR sensor's sensitivity following the methods described in Chapter 4: white light spectral measurement and normalized laser intensity measurement. A shift to a longer resonance wavelength in response to an increasing solvent refractive index was observed by both the reflectance spectrum measurement and the real-time normalized intensity measurement.

The sensitivity to the bulk refractive index was determined to be 1840 nm/ RIU by wavelength modulation, as Figure 5.2(a) shows. Real-time measurement with much higher detection sensitivity was achieved by normalized intensity measurement, as Figure 5.2(b) shows. Given that 0.125% ethylene glycol solution with an RI larger by 1.25×10^{-4} than the baseline yielded a 0.182-nm wavelength shift, and the resolution of this PC-TIR biosensor could be 1.6×10^{-5} nm; the detection limit of this sensor for the bulk refractive index was determined to be 1×10^{-8} RIU. The larger sensitivity for the present sensor relative to Figure 4.10 was due to a smaller amount of silicon within the defect layer, which decreased the effective refractive index of the defect layer and thus improved the sensitivity to the RI change of the surrounding medium.

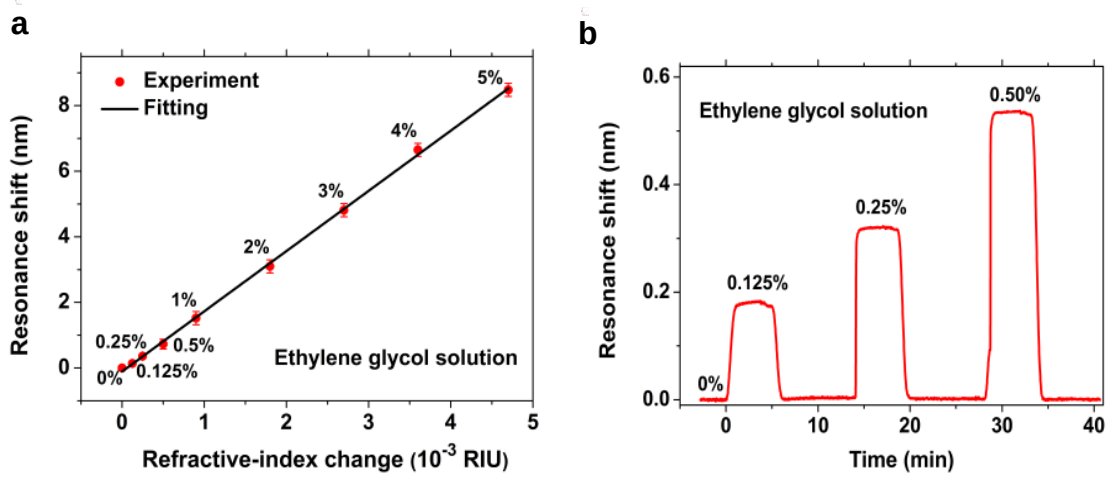

Figure 5.2 (a) Wavelength measurement with different refractive indices solution on the sensing surface; (b) normalized intensity modulation measuring the real-time bulk solvent refractive index change.

5.3 Molecules

The molecular pair of streptavidin-biotin has an extremely high binding affinity and serves as an excellent model for biomolecular recognition [86]. Streptavidin is a tetrameric protein which can bind up to four biotin molecules with minimal impact on its biological activity and therefore allows for extending the analyte accessibility of the biosensor. Moreover, biotin is a small molecule, and it can be chemically attached to a number of molecules of interest (e.g., proteins, antibodies), which will not change the natural properties of the targeted molecules but will greatly increase the binding affinity with streptavidin molecules.

In order to test the capability and sensitivity of the PC-TIR sensor for biomolecular detections, we chose streptavidin as the ligand immobilized on the sensing surface and measured the specific binding of different types and sizes of biotin molecules, including free D-Biotin, biotinylated DNA oligonucleotides, biotinylated proteins (Protein A and BSA), and biotinylated antibodies (anti-mouse immunoglobulin G–IgG–produced in goats). The molecular weights of these biotin molecules have a wide range of over three orders of magnitude, as listed in Table 5.1. In addition, the biotin molar ratio shows how many biotin molecules or biotin binding sites are in one analyte molecule. For example, streptavidin has four biotin binding sites, so *n* is 4. A single-strand DNA oligonucleotide

can be easily conjugated with one biotin molecule at one end, like biotin-10T with the sequence 5'-Biotin-TTT TTT TTT T-3', so we designed a series of lengths of T bases with the same biotin molar ratio (n = 1) for checking the PC-TIR sensor's response to the biomolecular sizes. The biotin molar ratio is usually large for large molecules like proteins and antibodies, which have complicated binding behaviors with streptavidin, as shown below.

Name	MW (Da)	Biotin molar ratio *n*
Streptavidin	~ 52,000	4:1
Very small molecule		
D-Biotin	244.13	1:1
DNA oligonucleotides *		
Biotin-10T	3,385.3	1:1
Biotin-20T	6,427.1	1:1
Biotin-30T	9,468.9	1:1
Biotin-40T	12,510.7	1:1
Biotin-50T	15,552.5	1:1
Biotin-60T	18,594.3	1:1
20A	6,202.2	none
20C	5,721.6	none
Proteins		
Biotin-Protein A	~ 41,000	~ 6:1
Biotin-BSA	~ 66,000	~ 9:1
Antibodies		
Biotin-IgG	~ 150,000	unknown
IgG	~ 150,000	none

Table 5.1 Detail information on molecules in experiments.

* Biotin-10T means that single-strand DNA oligonucleotide with 10-T bases was biotinylated (sequence 5'-Biotin-TTT TTT TTT T-3'), the same as other T bases. All the DNA oligomers used RP1 purification.

~ means approximate values, obtained from Vendors.

5.4 Streptavidin Immobilization on a Silica Surface

For measuring the ligand-analyte interaction, the analyte binding capacity of the sensing surface depends on the amount of immobilized ligand, or more accurately, the density of available binding sites. The theoretical maximum response R_{max} can be calculated using the formula below [87]:

$$R_{\max} = \frac{M_{\text{analyte}}}{M_{\text{ligand}}} \bullet R_{ads} \bullet n \qquad (5.1)$$

where $M_{analyte}$ and M_{ligand} are the molecular weights of the analyte and the ligand, respectively; R_{ads} is the sensor response of the ligand adsorbed on the sensing surface; and n is the molar ratio of the binding sites in the ligand. Obviously, in order to get the large response for binding of biotinylated molecules, the density of free biotin-binding sites on the streptavidin bound to the sensing surface should be large.

There are typically three methods to immobilize streptavidin molecules on a silica surface. One is direct adsorption. Although monolayer streptavidin can be obtained [88], it is not stable because of the weak adhesion between streptavidin and a silica surface, which is not suitable for further biotin molecules' binding. The second one is specific non-covalent binding described in Chapter 4.3.5. The silica surface is functionalized with biotin molecules, then streptavidin can be tightly and largely bound to the surface. As Figure 5.3 (a) shows, a large amount of streptavidin molecules was bound on the biotin-functionalized surface that produced a 5.24-nm resonance wavelength shift. However, the problem with this approach is that, although streptavidin has four biotin-binding sites, most of the sites were occupied by previous biotin molecules on the surface, thus there were few sites for further biotin-conjugated molecule binding. As Figure 5.3 (b) shows, I tested the available biotin binding sites left on the sensing surface by flowing 10 μg/mL biotinylated IgG (biotin-IgG) in PBS solution, which only caused a 0.40-nm resonance wavelength shift. It meant that only a few biotin-binding sites were left on the sensing surface after streptavidin adsorption via specific non-covalent binding.

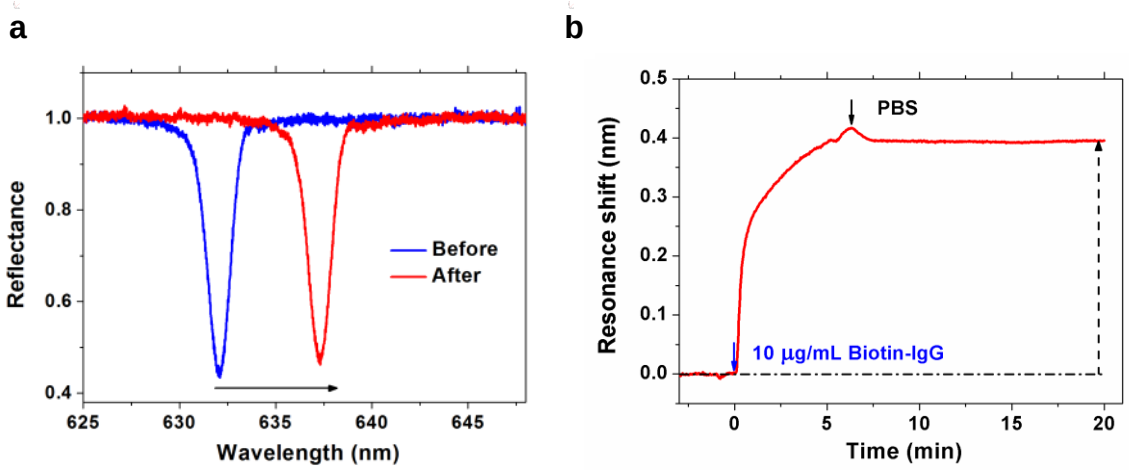

Figure 5.3 (a) Detection of SA binding to biotinylated surface; (b) large-size molecule biotin-IgG binding to streptavidin adsorbed on the surface via specific non-covalent binding.

In order to optimize the available biotin-binding sites in streptavidin molecules bound to the sensing surface (and therefore increase the sensitivity of the sensor), another method (that is, covalent binding) not employing biotin was adopted to immobilize the streptavidin. In this case, the streptavidin was coupled to the silica sensing surface covalently through the primary amino groups ($-NH_2$) in the molecules (shown in Figure 5.4) [89]. Therefore, all four-biotin-binding sites in the streptavidin molecules could be available for biotin molecule binding.

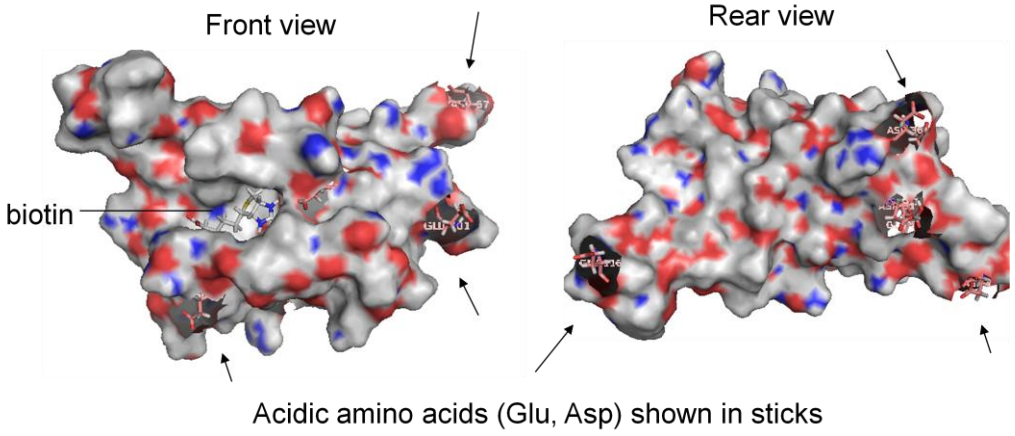

Figure 5.4 Structure of streptavidin molecules in complex with biotin created from an x-ray crystal structure (PDB 2rtl) (Courtesy of Dr. Choi, Seok Ki, University of Michigan).

Figure 5.5 shows the schematic process of the surface treatment I employed: the silica surface was first meticulously cleaned by a highly oxidative piranha solution, a mixture (3:1) of sulfuric acid (H_2SO_4, 98%) and hydrogen peroxide solution (H_2O_2, 30%) for up to 10 minutes. *Caution! Piranha solution is extremely corrosive, reactive, and potentially explosive, and should be handled with consideration for safety*.

After the cleaning procedure, all surface groups on the silica surface were transformed into hydrophilic silanol functionalities (-OH). Then the OH-terminated SiO_2 surface was converted to an NH_2-terminated (amino group) one by flowing 3% (3-Aminopropyl) triethoxysilane (3-APTES) solution in methanol/water (1:1) over the surface for 20 minutes. Next, succinic anhydride was used to convert amino groups on a silanized silica surface to carboxylic groups (-COOH). This chemical reaction is slow; therefore, in the experiments, 0.2 M succinic anhydride solution in acetonitrile was flowed with a low rate of 5 μL/minutes over the surface for a long time (more than 12 hours). *Caution! Acetonitrile is an organic solvent and can resolve or soften some polymer materials. Highly chemical-resistant polymer (like Teflon) is recommended for fluidic tubes*.

Subsequently, fresh 0.4 M 1-ethyl-3-(3-dimethylaminopropyl) carbodiimide (EDC) and 0.1M N-hydroxysuccinimide (NHS) solutions in DI-water were mixed (1:1) and used to activate the surface for a certain time (normally 15 minutes), further converting the carboxylic groups to amine-reactive succinimide esters (Sulfo-NHS) that can covalently bind streptavidin to the sensor surface. *Caution! Succinimide esters have a short period of effectivity, and streptavidin solution should be immediately flowed after EDC/NHS activation to achieve maximum covalent immobilization.*

Finally, 25 μg/mL streptavidin solution was immediately flowed over the functionalized sensing surface until saturation. After that, a 500-μg/mL high concentration of Bovine serum albumin (BSA) solution in PBS was flowed with sufficient time to block nonspecific binding sites on the surface and to get a stable baseline.

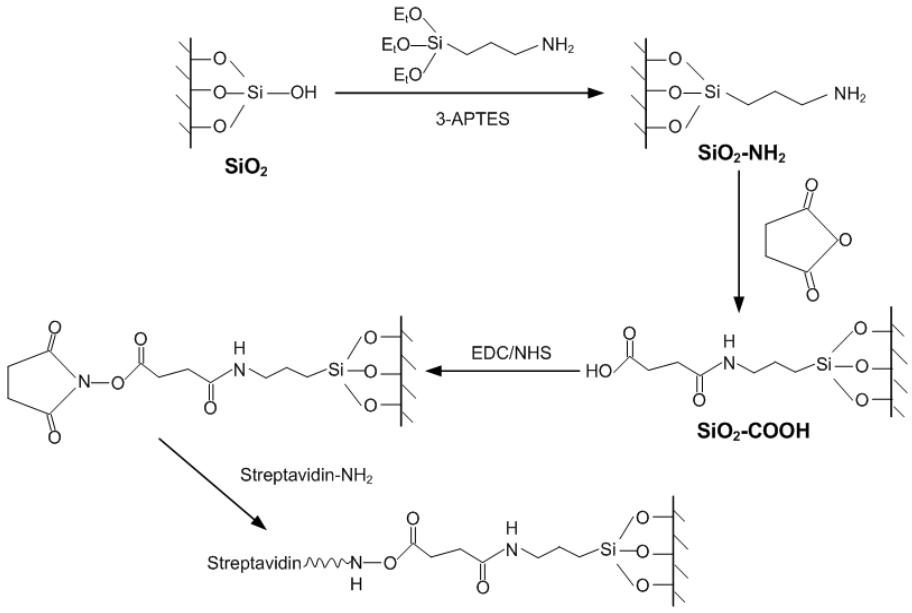

Figure 5.5 Surface functionalization for streptavidin covalently binding to a silica-sensing surface.

Due to electrostatic interactions between the ligand and the surface, the buffer used to prepare the ligand solution may affect the ligand immobilization level [87, 90]. For streptavidin, its isoelectronic point (pI) is ~5.0, so it is negatively charged at a buffer pH of > 5.0 and positively charged at a buffer pH of < 5.0. Considering that a carboxylic group has a net negative charge at pH > 3.5, the suitable pH value of buffer for streptavidin immobilization would be 3.5 < pH < 5.0 so that positively charged streptavidin molecules are more easily bound to the negatively charged carboxylic groups. However, amine coupling is less efficient at low pH buffer. Therefore the entire immobilization procedure has to be performed in order to optimize the conditions and verify the choice of buffer. Figure 5.6 shows the observed streptavidin immobilization level using different pH and/or buffer, and it is found that a 100-mM morpholinoethanesulfonic acid (MES) buffer at pH 5.0 provides the maximum observed resonance wavelength shift of 5.04 nm due to streptavidin adsorption on the sensing surface. This represents an effective 4.38-nm layer thickness, assuming the streptavidin has the same refractive index as the silica. In addition, the level of streptavidin immobilization in the MES buffer may also vary with experimental conditions, including MES buffer pH change, EDC/NHS activation time, etc.

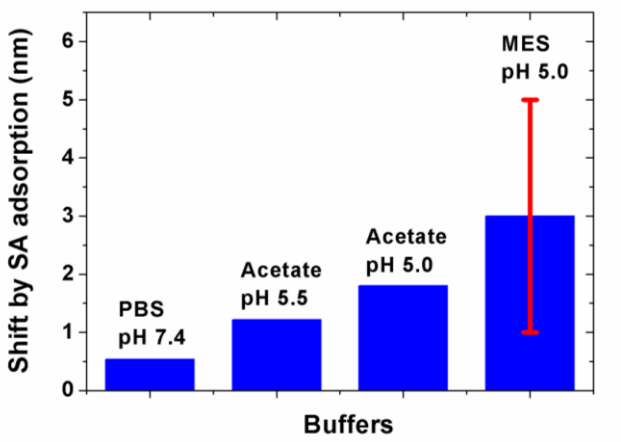

Figure 5.6 The effect of buffer and pH on streptavidin immobilization level.

5.5 Real-Time, Label-free Detection of Molecule Binding

5.5.1 Control experiments

To quantify the specific binding between biotinylated molecules and streptavidin, it was crucial to characterize and further minimize the nonspecific binding between the biotin molecules and the sensing surface. Independent control experiments were performed where all the surface functionalization procedures were the same as the section above except that the streptavidin was replaced by BSA. The results show that there was no observable nonspecific binding between the biotin molecules in this study and the functionalized sensing surface. Two examples (10 μg/mL biotin-IgG and 1 μM D-Biotin) are given in Figure 5.7. Notice that the sensor response to those biotin molecule solutions in PBS are not related to their molecular sizes but rather to the difference of their bulk solvent refractive indices from that of the PBS buffer.

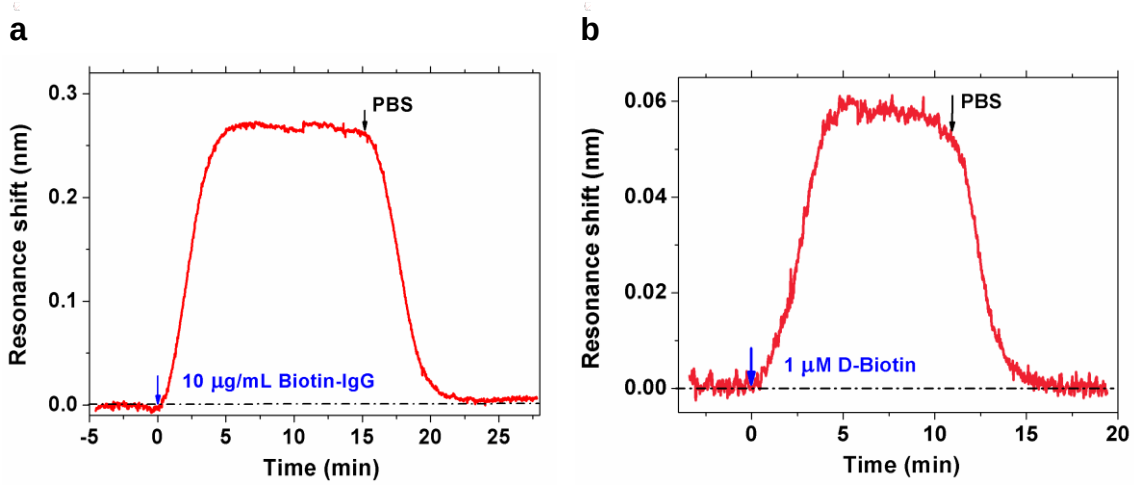

Figure 5.7 Control experiments for biotin molecules flowing over BSA-adsorbed surfaces: (a) 10 µg/mL biotin-IgG; (b) 1 µM D-Biotin.

5.5.2 Procedure and evaluation of biotin molecule binding

After streptavidin was covalently attached to the sensing surface, the biotin-analyte solution was directed through a flow channel to the sensor surface to evaluate the specific interaction between the biotin and streptavidin. Before the injection, PBS buffer was flowed over the sensing surface for a time sufficient to obtain a stable baseline. This was followed by the biotinylated analyte solution in PBS, which was introduced onto the sensor surface at a rate of 50 µL/minute. After equilibrium was achieved, PBS buffer was again used to remove unbound or weakly attached analytes until a new, stable baseline was achieved. The difference between the final baseline and the initial baseline was the amount of the resonance wavelength shift caused by biotin molecules bound to the sensing surface, and the result was compared to an independently performed control experiment. The sensor response to the specific binding between the biotin and the streptavidin was related to the size (molecular weight) of the biotin molecule, the immobilized amount of streptavidin on the sensing surface, and the biotin binding sites occupied by the biotin molecule.

In order to compare the binding events among different molecules, we derived the effective occupied sites n_{eff} from Equation 5.1, as the following shows:

$$n_{eff} = \frac{R_{analyte} / \mathrm{M}_{\mathrm{analyte}}}{\mathrm{R}_{\mathrm{ligand}} / \mathrm{M}_{\mathrm{ligand}}} \qquad (5.2)$$

where $R_{analyte}$ and R_{ligand} are the actual immobilized amounts (i.e., sensor response) of analyte and ligand molecules; $M_{analyte}$ and M_{ligand} are defined as above; and n_{eff} shows the molar ratio of one bound analyte molecule to one ligand molecule adsorbed on the sensing surface.

5.5.3 Detection of very large molecule: antibody

We first analyzed the binding of the largest molecule biotinylated antibody, IgG (MW ~ 150,000 Da). As Figure 5.8 (a) shows, a 10 μg/mL biotin-IgG solution in PBS was flowed twice until it saturated the sensing surface where streptavidin adsorption produced a 3.45-nm resonance wavelength shift. Clearly the second biotin-IgG injection showed no further specific binding and demonstrated only a small resonance shift due to a bulk solvent refractive index effect. Given that there was no observable nonspecific binding between the biotin-IgG and the sensing surface, it was proven that the final 2.54-nm resonance shift was entirely due to specific binding between the biotin-IgG and the streptavidin.

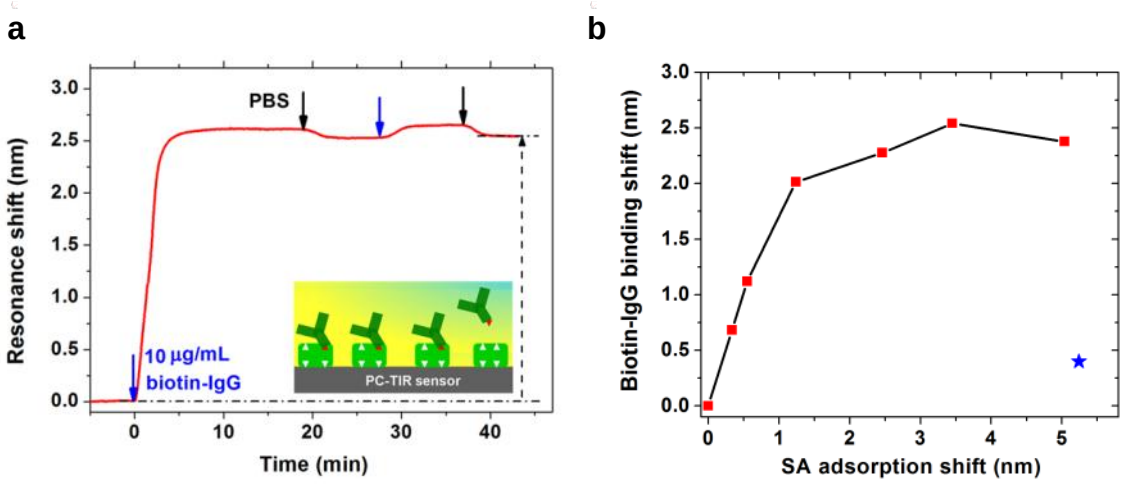

Figure 5.8 (a) Real-time biotin-IgG molecules binding to streptavidin-adsorbed sensing surface. The blue arrow stands for the starting point of injecting analyte solution, and the black arrow for injecting PBS buffer; inset diagrams show the schematic of the dynamic biomolecular interactions (same for all the following figures). (b) Biotin-IgG binding shift dependence on streptavidin (SA) adsorption.

We also measured the biotin-IgG binding with different streptavidin adsorption on the sensing surface, as Figure 5.8 (b) shows. When the adsorption was small (below 1.5-nm shift), the biotin-IgG binding shift was almost linearly proportional to the SA adsorption shift (i.e., the amount of streptavidin adsorbed on the sensing surface); however, as the adsorption became larger, the biotin-IgG binding saturated and eventually decreased. This can be understood as a pro-zone effect, where crowding the streptavidin sensing surface prevented additional large molecules of biotin-IgG from accessing biotin-binding sites [30, 82]. In addition, the blue star in Figure 5.8 (b) is the experimental result (shown in Figure 5.3) using the specific non-covalent binding method to immobilize streptavidin on the silica sensing surface. Compared with the results using the covalent binding method, it is clear that the covalent binding method is much more efficient and provides many more available sites for biotin binding.

5.5.4 Detection of large molecules: proteins

The covalent streptavidin immobilization method also enhances the PC-TIR sensor's capability to detect smaller molecules, such as proteins. This was demonstrated using biotin-BSA (MW ~ 66,000 Da) and biotin-Protein A (MW ~ 41,000 Da).

After streptavidin was adsorbed on the sensing surface, a high concentration of BSA solution was flowed for enough time to block the nonspecific binding sites on the sensing surface. As shown in Figure 5.9 (a), the second BSA flowing showed that there were no more nonspecific binding sites left for the BSA molecules. In contrast, when 10 μg/mL biotin-BSA solution in PBS was flowed over the functionalized sensing surface afterward, a large 1.78-nm binding shift was observed. Clearly, it was due to the specific binding between the biotin-BSA in the solution and the streptavidin on the sensing surface (2.65-nm adsorption shift). It also demonstrates that the PC-TIR sensor can perform specificity experiments for biomolecular detection.

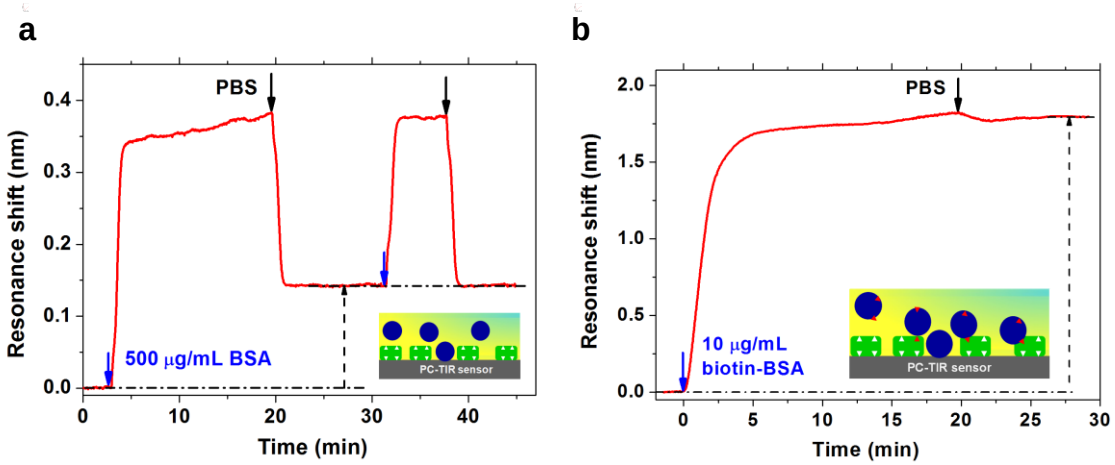

Figure 5.9 (a) Blocking streptavidin-adsorbed sensing surface with high-concentration BSA solution; (b) real-time biotin-BSA specifically binding to streptavidin-adsorbed sensing surface.

A significant resonance shift (1.14 nm) was also observed for the biotin-Protein A binding to the streptavidin (2.36-nm adsorption shift), as shown in Figure 5.10 (a). Furthermore, we tested the multilayered binding of streptavidin to biotinylated Protein A, followed by the binding of (non-biotinylated) goat IgG to protein A, where Protein A binds approximately 25% of the goat IgG subclasses. Ten μg/mL of IgG solution was flowed before and after Protein-A binding to the SA-adsorbed sensing surface (Figure 5.10 (b). The results showed no observable binding of the IgG to the sensing surface but a large specific interaction between the IgG and Protein A. Considering their molecular weights (150,000 Da for IgG and 41,000 Da for Protein A) and the amount of biomolecules bound on the sensing surface (1.18-nm and 1.33-nm shifts for the IgG and Protein A, respectively), the effective binding site n_{eff} was calculated to be 0.24; that is to say, the binding activity of the Protein A for goat IgG was 24%–very close to the ideal condition. This demonstrates the PC-TIR sensor's high efficiency for multilayered molecular interactions.

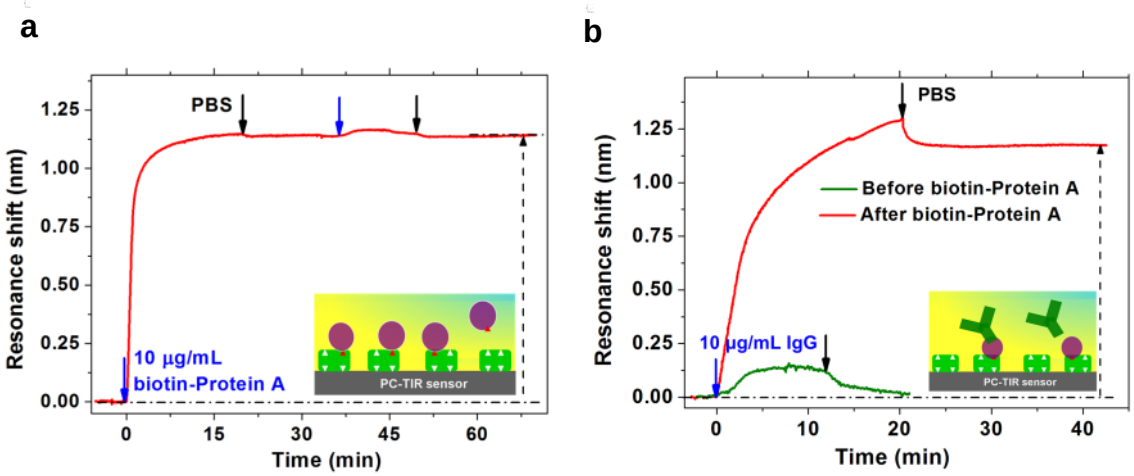

Figure 5.10 (a) Real-time biotinylated Protein A binding to streptavidin-adsorbed sensing surface; (b) biomolecular interactions between biotinylated Protein A and IgG.

5.5.5 Detection of medium and small molecules: DNA oligonucleotides

Quantitative analysis of high specific DNA detection is very important in many applications, including biomedical research, pharmaceutical discovery, and homeland security [91]. Currently, the most popular method is fluorescent microarray technology [92], but quantitative analysis is challenging due to the lack of the precise control of fluorescent labeling and the inability to acquire real-time signals. Label-free optical detection of analytes in their native form is in great need to address the limitations of microarrays in DNA detection. In order to demonstrate high performances of the PC-TIR sensor, we designed and executed a series of experiments for DNA oligonucleotide detection, including different lengths of single-strand DNA (ssDNA) oligonucleotides binding to protein, determination of concentration limits, and oligonucleotide hybridization studies.

A. Different lengths of DNA oligonucleotides binding detection

First, we tested the response (resonance wavelength shift) of the PC-TIR sensor to different lengths of biotinylated ssDNA oligonucleotides specifically binding to streptavidin, shown in Figure 5.11. The binding shifts of 1 µM biotin-40T, biotin-30T, biotin-20T and biotin-10T were 1.33 nm, 0.78 nm, 0.68 nm and 0.44 nm, with the corresponding streptavidin adsorption shifts of 3.38 nm, 2.14 nm, 2.52 nm and 2.04 nm, respectively. Taking into account the resolution the current PC-TIR sensor system can

achieve, i.e., 1.6×10^{-5} nm, there is no doubt that the PC-TIR sensor has very high sensitivity and is able to detect very short length ssDNA oligonucleotides (<< 10 bases).

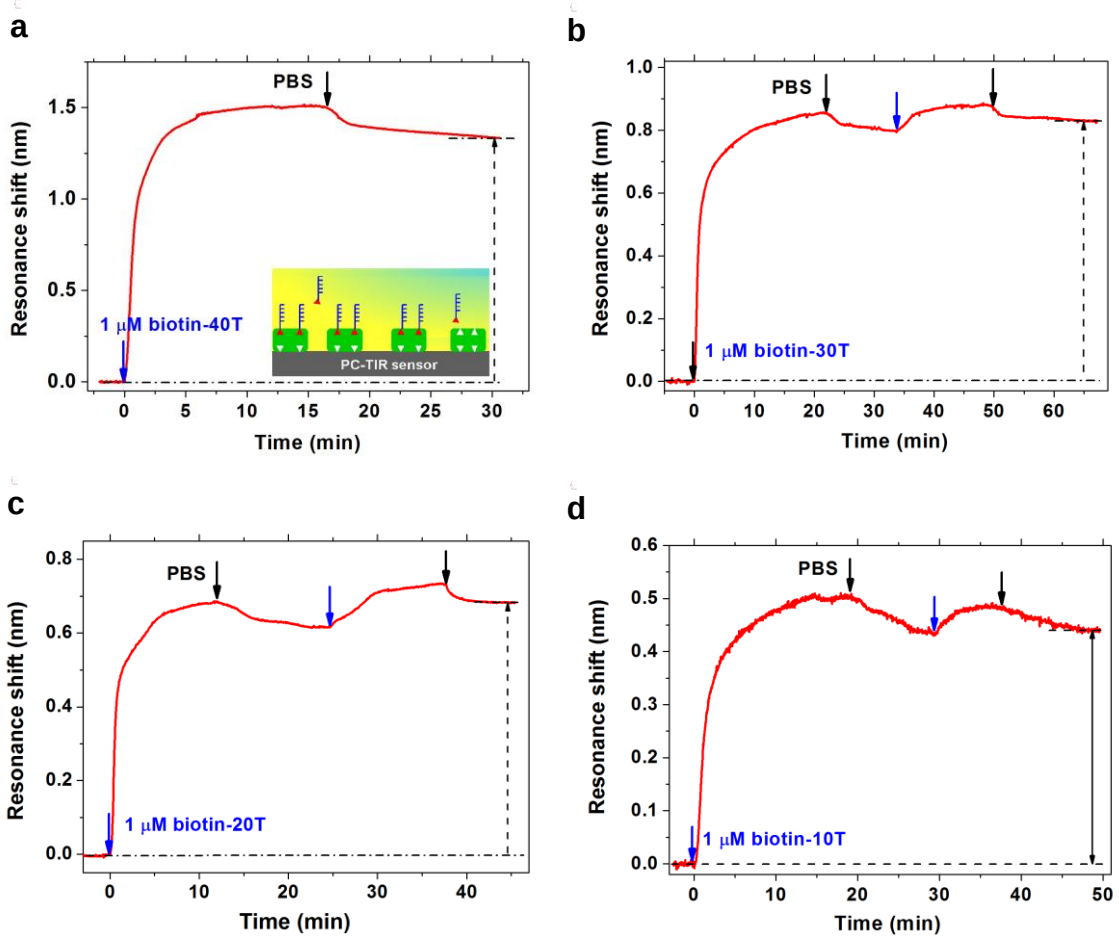

Figure 5.11 Real-time biotinylated single-strand DNA oligonucleotides binding to streptavidin-adsorbed sensing surfaces: (a) biotin-40T; (b) biotin-30T; (c) biotin-20T; (d) biotin-10T.

B. Low concentration DNA oligonucleotides binding

We further investigated the ability of the PC-TIR sensor to detect short DNA oligonucleotide binding to protein at low concentrations. As Figure 5.12 shows, a series of four concentrations (1 nM, 10 nM, 100 nM and 1 μM) of biotin-20T solution in PBS were flowed over the streptavidin-adsorbed sensing surface, which caused resonance wavelength shifts of 0.033 nm, 0.108 nm, 0.334 nm, and 0.166 nm, respectively. The accumulated shift increased monotonically as more and more biotin-20T molecules became tightly bound to the streptavidin until saturation.

With the 2.480-nm streptavidin adsorption shift, the overall biotin-20T binding shift of 0.641 nm was close to the prior result (Figure 5.11c), confirming the PC-TIR sensor's reproducibility. The lowest injected solution (1-nM biotin-20T) produced a 0.033-nm shift, thus the detection limit of the PC-TIR sensor for short (20-mer) ssDNA oligonucleotides is estimated to be less than 0.5 pM, which is approximately four orders of magnitude lower than the value that has been reported for the SPR-based system (10 nM for 18-mer unlabeled DNA oligonucleotide [93]). Of course, a further dose-response experiment [94] will be helpful to verify the statement here.

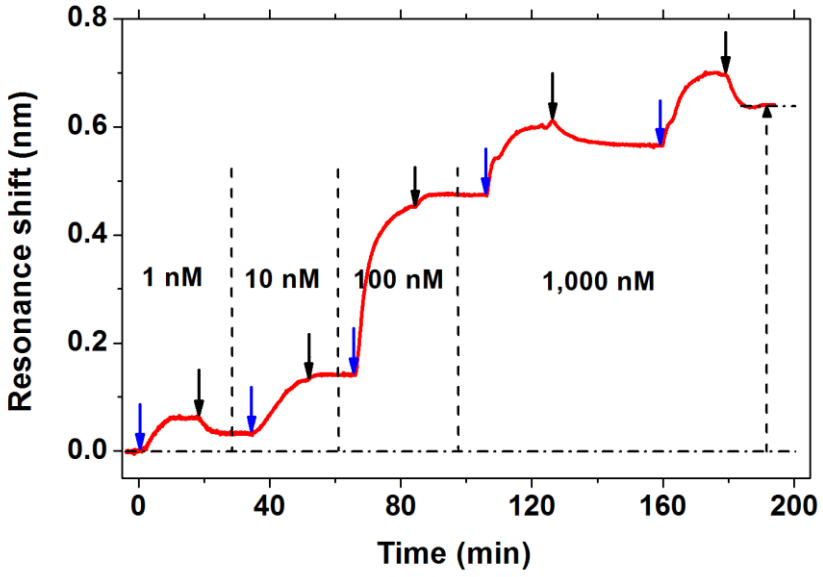

Figure 5.12 Sensorgram of low concentrations of biotinylated single-strand DNA oligonucleotides binding to streptavidin-adsorbed sensing surface.

C. DNA oligonucleotides hybridization

We also examined the binding of different base-mismatched DNA oligonucleotides (20A, 20C) hybridizing to biotinylated 20T that has been bound on the SA-adsorbed sensor surface as described above. As shown in Figure 5.12 (a), a control experiment in which the complementary oligonucleotide 20A was flowed before biotin-20T binding did not display any perceptible shift, while a very large specific binding was observed for totally matched 20A after biotin-20T bound on the surface. In contrast, the completely-mismatched oligonucleotide 20C displayed no binding to the sensing surface.

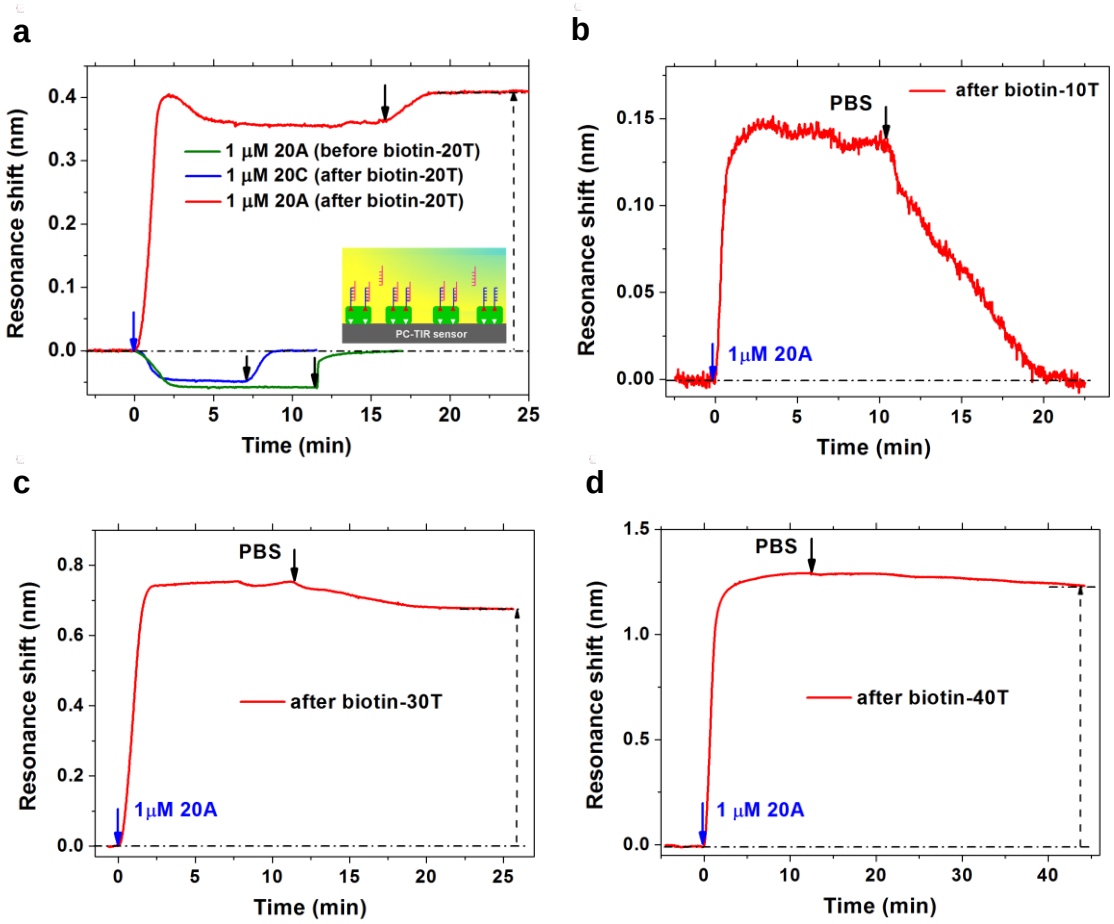

Figure 5.13 Oligonucleotides 20A hybridizing to biotinylated T bases bound on the sensing surface (a) biotin-20T; (b) biotin-10T; (c) biotin-30T; (d) biotin-40T.

Furthermore, we investigated the hybridization of DNA oligonucleotide 20A to different lengths of T bases (biotin-10T, biotin-30T and biotin-40T), as shown in Figure 5.13. Since A base is totally matched to T base, the hybridization was fast during association, and 20A was tightly bound on the T base-adsorbed surface during the dissociation period, except for the 10T-adsorbed one. This could be explained by two possible reasons: first, there were limited binding sites on the 10T-adsorbed surface and constant flowing might wash 20A away from the surface; second, the melting temperature for 10T is 22.2^{o}C. Compared to 52.2 ^{o}C, 62.7 ^{o}C and 68.0 ^{o}C for 20T, 30T and 40T, respectively, 10T was easier to melt at room temperature and then decreased its hybridization efficiency with 20A.

The final resonance shift due to hybridization between the 20A and the different-strand-length T bases (10T, 20T, 30T, 40T), shown in Figure 5.13, were 0, 0.41nm, 0.68nm, and 1.23nm, with the corresponding T-based binding shifts of 0.44 nm, 0.44 nm, 0.82 nm, and 1.33 nm, respectively. According to Equation 5.2, the effective binding sites n_{eff} were calculated to be 0, 0.96, 1.27, and 1.86; however, taking into account the total number of T bases in the ssDNA oligonucleotides available for the A base, the hybridization efficiencies were 0, 0.96, 0.85, and 0.93, instead. As shown in Figure 5.14, the hybridization efficiency was always high (near to 1) for completely matched DNA oligonucleotides.

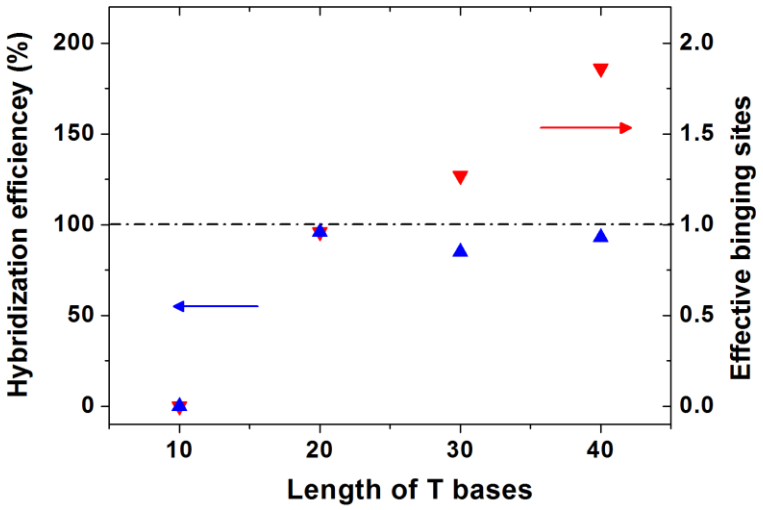

Figure 5.14 Oligonucleotide 20A's hybridization efficiency to different lengths of T bases.

The above experiments demonstrate that the PC-TIR sensor has enough sensitivity and capability to examine critical DNA binding and hybridization activities, which provides an effective tool for performing quantitative analysis on DNA studies.

5.5.6 Detection of very small molecule: D-Biotin

Small molecule interactions with protein molecules are of great importance in the therapeutic drug discovery process. Given that the proteins of interest are often very large and bind only a limited number of the molecules of interest, highly sensitive techniques are required to measure such interactions directly. Therefore, the ability of detecting

small molecules becomes the criterion for checking the sensitivity of label-free optical biosensors. In order to determine the minimum molecular weight detection limit of the PC-TIR sensor, we evaluated the binding of the smallest biotin molecule D-Biotin (MW 244 Da), as Figure 5.15 shows.

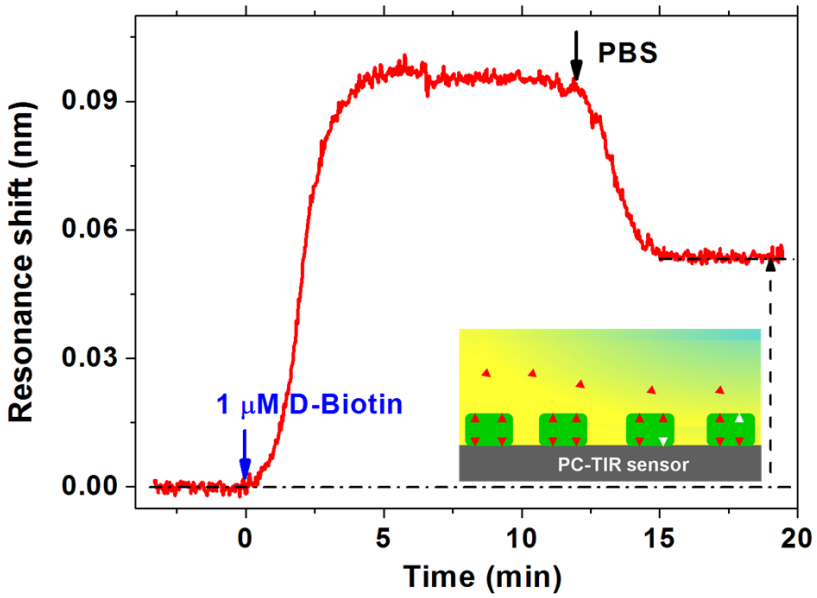

Figure 5.15 D-Biotin binding detection by the PC-TIR sensor.

In this experiment, the immobilization of streptavidin produced a 3.0-nm optical resonance shift. According to Equation 5.1, the maximum theoretical response of D-Biotin's binding to streptavidin is 0.056 nm, if all the biotin-binding sites in the streptavidin (4 per molecule) on the sensing surface are occupied. When 1 μM D-Biotin solution in PBS was flowed over the streptavidin sensing surface, the binding resonance wavelength shift was determined to be 0.053 nm (Figure 5.15), which is very close to the maximum theoretical result. Since there was no nonspecific binding between the D-Biotin and the functionalized surface, this implies that almost all four biotin-binding sites in the streptavidin were occupied by D-Biotin. Taking into account the resolution the current system can achieve, i.e., 1.6×10^{-5} nm, the signal-to-noise ratio for detecting 1 μM D-Biotin was up to 3,300, which indicates that the concentration detection limit of the PC-TIR sensor for D-Biotin detection can be as low as 300 pM; this also suggests that this sensor may be able to detect the binding of analytes with a molecular weight of less

than 100 Da. Similarly, a dose-response experiment [16] will be of great help to more accurately determine the detection limits for D-Biotin detection concentration and molecule size.

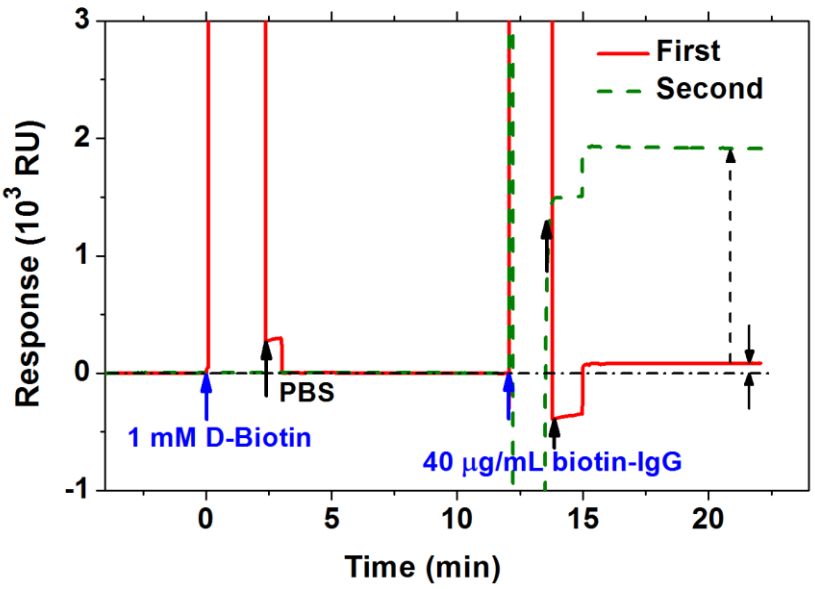

Figure 5.16 D-Biotin binding detection by Biacore X.

To obtain a direct comparison of the PC-TIR sensor with standard SPR-based measurements, we used a commercial SPR system (Biacore X) to measure D-Biotin binding to an SA chip (streptavidin-coated sensing chip) having a high surface density of 400-600 ng/cm^2 and all four biotin binding sites of the immobilized SA molecules available [95]. As Figure 5.16 shows, 1 mM D-Biotin solution in PBS (a concentration is 1,000 times larger than that used with our PC-TIR sensor), was first flowed over the SA chip, and no binding was observed. After continuous flowing of 40 μg/mL biotin-IgG solution in PBS over three minutes, an insignificant 85 resonance units (RU) of binding was observed, which is much less than the 1,915 RU response obtained by directly flowing the same concentration biotin-IgG solution over a new SA chip. Thus, the D-Biotin did bind to the SA chip, but the Biacore X did not have the sensitivity to resolve it. In contrast, the PC-TIR sensor can easily resolve small-molecule binding with ultrahigh SNR; a comparison of the detection limits for various label-free optical methods is given in Table 5-2. It was shown that the PC-TIR sensor had achieved several orders of magnitude higher detection sensitivity for very small molecule (D-Biotin) binding than

any other label-free optical biosensor reported to date, indicating the great potential of this biosensor for highly-sensitive biomolecular detection.

Technology platform	Optical structures	Detection limit	References
SPR	Conventional SPR	> 100 μM	[96]
	Plasmonic metamaterials	300 nM	[16]
Interferometry	Dual-polarization interferometry	30 nM ǂ	[97]
Waveguide	Waveguide with corrugated gratings	35 nM	[98]
Ring resonator	Ring on a chip	> 25 μM	[99]
Photonic crystals	1-D PC with grating surface	240 nM	[100]
	Surface wave 1-D PC	800 nM ǂ	[38]
	PC-TIR	**300 pM**	**This work**

Table 5.2 D-Biotin molecule detection limits of various optical biosensors.*

* In order to effectively compare the properties of optical biosensors, we only cited references which measured D-Biotin binding to streptavidin. Some detection limits not explicitly stated in the references were derived from the other data given.

ǂ The sensors detected the changes of both refractive index and physical thickness, and the latter was used to calculate detection limits.

5.5.7 Analysis of molecules binding

From the experiments above, it was easy to find that the analyte (biotin molecules) binding was greatly dependent on the ligand's (streptavidin) immobilization on the sensing surface. As Equation 5.1 shows, normally the maximum analyte binding response is linearly related to the density of the immobilized binding sites, but different sizes of biotinylated molecules may behave differently, especially since the number of biotins per molecule will vary. Here we evaluated the effect of streptavidin adsorption (i.e., the amount of streptavidin adsorbed on the sensing surface) on different sizes of biotin molecules' binding measurements, as shown in Figure 5.17.

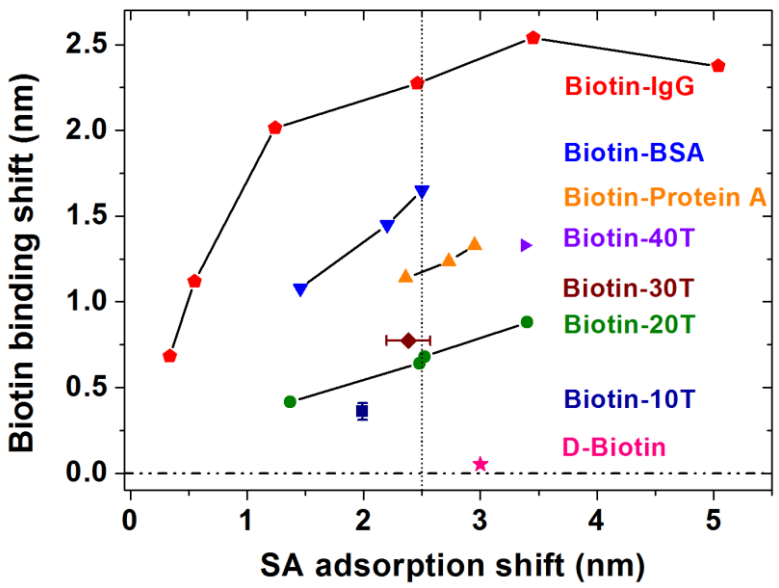

Figure 5.17 Response of the PC-TIR sensor (resonance wavelength shift) to the binding of different-sized biotin molecules with different amount of streptavidin adsorption on the sensing surface.

For very small molecules of D-Biotin, as shown in Section 5.5.6, each streptavidin molecule was occupied by almost four D-Biotin molecules.

For larger-sized molecules (biotin-20T, biotin-Protein A and biotin-BSA), as Figure 5.18 shows, the wavelength shift was linearly proportional to the SA surface adsorption, with the slopes 0.25 $\pm$ 0.01, 0.45 $\pm$ 0.02, and 0.66 $\pm$ 0.04. According to Equation 5(2), it is easy to find that each streptavidin molecule binds approximately 2.0 biotin-20T, 0.6 biotin-Protein A, and 0.5 biotin-BSA molecules, respectively. The lower binding ratios observed with larger-sized molecules could be the result of two factors: one is a crowding effect, where larger molecules had difficulty accessing all of the biotin binding sites; the other is that larger biotinylated molecules had several conjugated biotins (6 for biotin-Protein A and 9 for biotin-BSA), thereby occupying more than one biotin binding site in the streptavidin, which decreased their binding ratios to it.

For the largest molecule (biotin-IgG), as discussed in Section 5.5.3, the binding shift was almost linear when the SA adsorption was small. It saturated and eventually decreased when SA adsorption was large due to the steric or crowding effect.

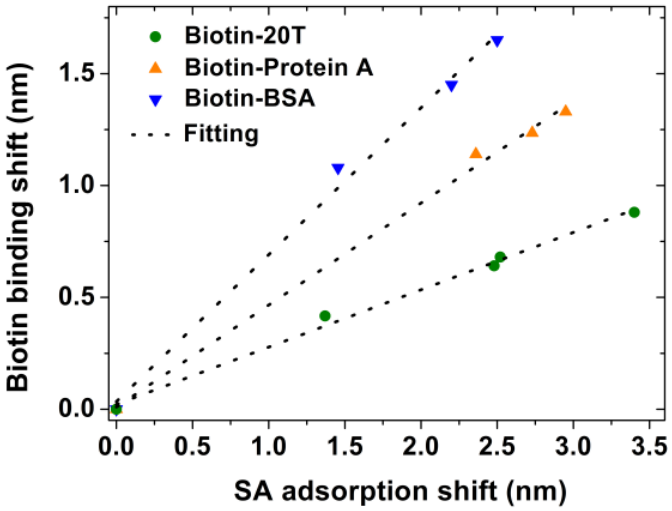

Figure 5.18 Experimental results and linear regression for biotin-BSA, biotin-Protein A, and biotin-20T, respectively, binding to the streptavidin-adsorbed sensing surface.

When the binding behavior of different-sized biotin molecules was further compared at the optimized streptavidin sensing surface concentration (2.50-nm adsorption shift), this PC-TIR sensor performed well and was able to distinguish a wide range of biological molecules, the responses (resonance wavelength shift) of which were increasing with larger molecule weights (Figure 5.19).

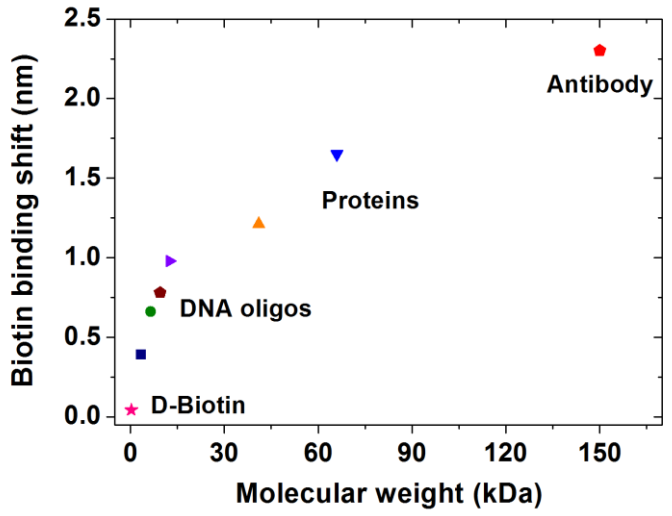

Figure 5.19 The biotin binding shift's dependence on molecule sizes for the same streptavidin adsorption (2.50-nm shift) on the sensing surface. Each symbol represents one molecule, and the binding shifts for smaller molecules (like biotin-Protein A, biotin-40T, biotin-10T, and D-Biotin) are reasonably derived by linear relation from the experimental results shown in Figure 5.17.

5.6 Conclusion

In this chapter, I have made a systematic investigation into the PC-TIR sensor's capability for label-free biomolecular detection, including sensitivity characterization of sensor structure, surface functionalization, binding experiments design and performance, and results analysis.

I have measured the binding of a wide range of molecules (molecular weight from 244 Da to 150,000 Da) with high sensitivity, and the detection limit of the smallest molecule investigated, D-Biotin, was estimated to be 300 pM. This value was several orders of magnitude lower than any previous report and showed the great potential of this biosensor for ultrasensitive biomolecular detection. Moreover, I demonstrated that this sensor was useful for performing quantitative analysis on DNA studies, including strand length measurement, low concentration DNA oligonucleotides binding, and DNA hybridization. It is also important to mention that this sensor allows the monitoring of biomolecular interactions in real time and hence has the ability to resolve kinetic constants and determine biomolecular binding affinity.

Further improvements are expected to yield even higher sensitivity. I am going to discuss it in the following chapter.

Chapter 6

Contributions and Further Developments

6.1 Contributions

Over the past two decades, label-free optical sensor development has been a fascinating and fast-paced area. Various optical structures have been investigated for sensitive label-free detection, the majority of which are: (1) surface plasmon resonance based biosensors; (2) interferometer-based biosensors; (3) optical waveguide based biosensors; (4) optical ring resonator based biosensors; (5) optical fiber based biosensors; and (6) photonic crystal based biosensors. A detailed review for these label-free biosensors could be found in reference [11]. The development of these biosensors also brings up many new commercial systems (see reference [6], [101] for details), such as Biacore from GE healthcare, AnaLight® system from Farfield group, BIND system from SRU Biosystems, Epic® system from Corning, Octet system from Fortebio, and SKi Pro™ system from Silicon kinetics.

Although a number of label-free techniques or systems for directly monitoring biomolecular binding exist, they are limited in their ability to measure the binding kinetics of very small molecules, to detect low concentrations of analyte molecules, or to detect low affinity interactions. The aim of this Ph.D. dissertation is to develop a new optical mechanism and corresponding system for label-free biomolecular interaction, which could fundamentally and significantly improve upon the detection sensitivity.

To this end, I have made a comprehensive study of a new photonic crystal technology PC-TIR (i.e., a one-dimensional photonic crystal structure in a total-internal-reflection geometry), including the theoretical analysis and simulated investigation of the principles (Chapter 2), the design and fabrication of the PC-TIR sensor structure (Chapter 3), the setup and performance characterization of the experimental system (Chapter 4),

and demonstrations of its high sensitivity for biomolecular detections (Chapter 5). The fully-developed PC-TIR sensor has achieved sensitivity that is several orders of magnitude higher than that which is achievable in SPR-based biosensors or other label-free optical biosensors in many important metrics – bulk solvent refractive index change, thin molecular layer adsorption, real-time protein binding, DNA hybridization, and small molecule detection, to name a few – which shows its great potential to be a high-sensitivity sensing platform for biological and medical research.

To illustrate the advance of the PC-TIR biosensor, I evaluated and compared the sensing performance of some label-free technologies that may continue to play an important role in the next five years (see Table 6.1).

Technology platform	Optical structures	Resonance width (nm)	Sensitivity (nm/RIU)	Detection limit	Ref.
SPR	Conventional SPR	~ 40	~ 3,000	5×10^{-7} RIU	[84]
				3×10^{-3} nm	[63]
				0.5 pg/mm^2	[20]
				10 nM for 18 bases	[93]
				> 100 μM for D-Biotin	[96]
	Plasmonic metamaterials	~ 100	3×10^{4}	300 nM for D-Biotin	[16]
Interferometry	Dual-polarization interferometry	---	---	0.01 nm	[97]
				0.1 pg/mm^2	
				30 nM for D-Biotin	
Waveguide	Corrugated gratings	---	---	0.3 pg/mm^2	[98]
				35 nM for D-Biotin	
Ring resonator	Capillary opto-fluidic ring	1×10^{-3}	31	6×10^{-7} RIU	[102]
				0.5 pg/mm^2	
Photonic crystal	1-D PC with grating surface	1.8	112	3×10^{-3} nm	[103]
				0.4 pg/mm^2	
				240 nM for D-Biotin	[100]
	1-D PC based on porous silicon	---	~ 550	50 pg/mm^2	[31]
	PC-TIR	~ 1	1840	~10^{-8} RIU	This work
				2×10^{-5} nm	
				6 fg/mm^2	
				0.5 pM for 20 T bases	
				300 pM for D-Biotin	

Table 6.1 Sensing performance of various label-free optical biosensors

Chapter summaries are presented below:

In **Chapter 2**, an effective transfer matrix method was introduced to simulate the PC-TIR structure at arbitrary angles and polarizations. The underlying and operating principles of the PC-TIR structure were investigated, and the structure was found to be a high-finesse Fabry-Pérot resonator with an open cavity layer. Intentional absorption in the cavity (defect) layer was adopted to characterize the resonance mode, and a normalized intensity measurement was developed to monitor the resonance shift due to biomolecular binding with the highest sensitivity. Then I derived the expression of the detection sensitivity and analyzed the effects of each structure parameter of the PC-TIR sensor or the incident light properties on the sensitivity via simulation; these effects include the polarization, the incident angle, the probe beam size, the number of alternating dielectric layers, the refractive indices and thicknesses of the dielectric layers, the absorption, the refractive index, and the thickness of the defect layer.

In **Chapter 3**, I investigated the parameters of a PC-TIR structure and discussed their effects on the structural properties in the experiments. Pure silicon film was used as the absorptive layer. I proposed a design criterion and fabricated, tested, and analyzed three kinds of 1-D PC structures with different light confinement abilities. It was found that the PC structure with less light confinement was preferable in making a suitable PC-TIR sensor that provided larger flexibility in engineering the absorption in the defect layer. Experimentally, I attained resonance dips of the PC-TIR sensor with the smallest reflectance minimum $R_{min} \sim 0$ for air and $R_{min} \sim 0.23$ for water and the narrowest dip width $\Delta\lambda \sim 1.00$ nm for water.

In **Chapter 4**, I described successfully building an integrated experimental system combining the white light spectra measurement for a large detection range and the normalized intensity measurement for high sensitivity. I also characterized the performance of the PC-TIR sensor: a bulk solvent refractive index sensitivity of $\sim 10^{-8}$ *RIU*, a thin molecule layer adsorption sensitivity of 2×10^{-5} *nm*, and a surface mass density sensitivity of 6 fg/mm^2, and I further compared it with SPR-based sensors.

In **Chapter 5**, I described making a systematic investigation into the PC-TIR sensor's capability for label-free biomolecular binding detection, including sensitivity characterization of the sensor structure, its surface functionalization, design and performance of binding experiments, and results analysis. I measured the binding of a wide range of molecules (molecular weight from 244 Da to 150,000 Da) with high sensitivity, and the detection limit of the smallest molecule investigated, D-Biotin, was estimated to be 300 pM. This value was several orders of magnitude lower than any previously reported. Moreover, I demonstrated that this sensor could perform quantitative analysis on DNA studies, including strand length measurement, low concentration DNA oligonucleotide binding, and DNA hybridization.

This dissertation work was funded with Federal funds from the National Cancer Institute, National Institutes of Health, under award 1 R21 RR021893. It has been turned into an issued U.S. patent and has been the foundation of a start-up company:

Ye, J. Y., **Guo**, **Y.**, Norris, T. B. and Baker, J. R. Photonic Crystal Sensor. *US Patent 7,639,362* (2009).

The work has also been published and presented at peer-review journals or conferences as follows:

Guo, **Y.**, Ye, J. Y., Divin, C., Huang, B., Thomas, T. P., Baker, J. R., and Norris, T. B. Real-time biomolecular binding detection using a sensitive photonic crystal biosensor. accepted by *Analytical Chemistry* (2010).

Guo, **Y.,** Ye, J. Y., Thomas, T. P., Baker, J. R., and Norris, T. B. Label-free measurement of DNA oligomer binding using a highly-sensitive photonic crystal biosensor. *CLEO*, paper CTuN5 (2010).

Guo, **Y.**, Ye, J. Y., Huang, B., McNerny, D., Thomas, T. P., Baker, J. R., and Norris, T. B. Real-time small molecule binding detection using a label-free photonic crystal biosensor. *Proc. SPIE* **7553**, 755303 (2010).

Guo, **Y.**, Ye, J. Y., Divin, C., Thomas, T. P., Myc, A., Begey, T., Baker, J. R., and Norris, T. B. Label-free biosensing using a photonic crystal structure in a total-internal-reflection geometry. *Proc. SPIE* **7188**, 71880B (2009).

Guo, **Y.**, Thomas, T. P., Ye, J. Y., Myc, A., Baker, J. R., and Norris, T. B. Real-time, label-free protein binding detection with a one dimensional photonic crystal sensor. *CLEO,* paper CTuCC6 (2009).

Guo, **Y.**, Ye, J. Y., Divin, C., Myc, A., Baker, J. R., and Norris, T. B. Optical biosensor based on one-dimensional photonic crystal in a total-internal-reflection geometry. *CLEO*, paper CThZ3 (2008).

Guo, **Y.**, Divin, C., Myc, A., Terry, F. L., Baker, J. R., Norris, T. B., and Ye, J. Y. Sensitive bioassay using a photonic crystal structure in total internal reflection. *Opt. Express* **16**, 11741 -11749 (2008).

6.2 Further Developments of the PC-TIR Sensor

6.2.1 Sensor system development

The PC-TIR sensor has a simple and unique configuration with an open sensing surface which can be easily implemented with other technologies for further advances. For example, the PC-TIR sensor could be fabricated with a nanostructure sensing surface, which will greatly increase the sensing area [16, 104] and give access to a size selectivity option for biomolecular analytes [104]. Also, this sensor may incorporate with molecular identification methods such as mass spectrometry [105] or Surface-Enhanced Raman Scattering [106] to provide comprehensive information on biomolecular interactions on the sensing surface. Moreover, by integrating with the current technologies of microfluidics, optical fibers or waveguides, micro-array laser sources or detectors, surface functionalization/patterning, nano-fabrication and many others [19], the PC-TIR sensor could develop into a high-sensitivity, high-throughput sensing platform for biomolecular analysis and medical diagnoses.

In the following, I discuss the developments of a fluidics system, a nanostructure sensing surface, and a compact system with angular modulation.

6.2.1.1 Fluidics system

Currently, the performance of the PC-TIR sensor is limited by the fluidics system, which is a very important component in real-time biomolecular binding measurement. The experimental setup shown in Figure 4.1 was integrated with a very simple fluidics system: a PDMS slab with two parallel flow channels. Considering the size of the collimated probe beam (1 mm in diameter), each channel was designed to be: 0.1 mm in height $\times$ 3 mm in width $\times$ 10 mm in length.

However, the large size of the flow channel caused some problems. First, it required a large sample volume; second, it caused large dispersion between the buffer and the solution, which caused the real binding events to be severely mixed with the bulk solvent effect, so that we could not accurately measure the binding kinetics and further determine the kinetics constants; third, it increased the flowing time. Normally it took at least 15 minutes for the current PC-TIR sensor to finish a binding experiment, while it took only 2 ~ 3 minutes for a well-engineered SPR-based system [20]. In addition, it also limited the

number of the flow channels on the sensor surface (25.4 mm in diameter). As discussed in Section 4.2.2, a third channel (as the control) could further improve the quality of the real-time biomolecular detection. A large number of flow channels also allows multiplex binding detection.

Therefore, the keys to improving the fluidics system are 1) a small-sized flow channel; 2) a fast transition between the buffer and the analyte solution. A small-sized flow channel can be achieved with a small probe beam size. However, as we discussed in section 2.5.6, when the beam size becomes smaller than a millimeter, close to the laser wavelength, the collimated laser beam (Gaussian beam) will have a divergence angle, which will broaden the narrow resonance dip of the PC-TIR sensor and then decrease the detection sensitivity. So there is a trade-off between the probe beam size (thus the flow channel) and the detection sensitivity.

For a fast transition between the buffer and the analyte solution, there are several ways to achieve it (refer to the flow cell of Biacore instruments [107]). Dr. Tom Bersano proposed one solution as Figure 6.1 shows.

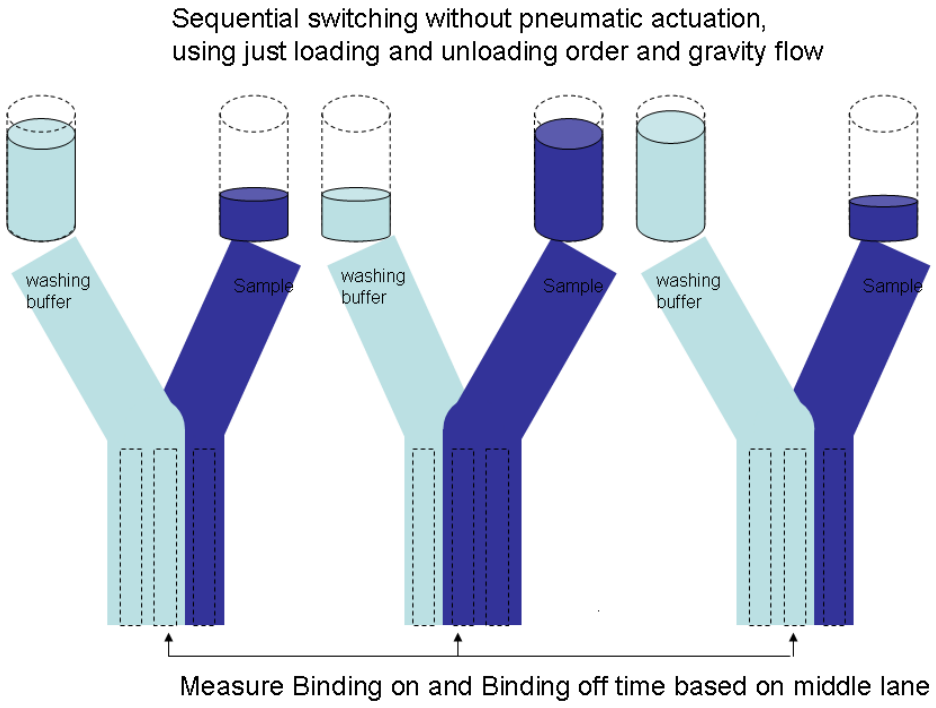

Figure 6.1 Schematic diagram of a flow cell using laminar and gravity flow.

It takes advantage of the laminar flow with different inlet pressures to get quick switching between the sample and the washing buffer, recording changes over time while having two fixed regions as the control and the middle area of the shifting laminar flow as the observable.

6.2.1.2 Nanostructure sensing surface

The response of a biosensor depends on the interaction of the analyte with the ligand immobilized on the sensing surface. Without modifying the detection scheme of the biosensor, increasing the available surface area for ligand adsorption and analyte binding is the most convenient way to improve the sensor sensitivity.

The sensing surface of the PC-TIR sensor is a planar one, which is a two-dimensional biosensing surface, as Figure 6.2 (a) shows. If we turn it into a three-dimensional biosensing surface like a porous [104] or a nanorod structure [108, 109], as Figure 6.2 (b) shows, the surface-to-volume ratio will be greatly increased, as well as the detection sensitivity of the sensor. The increasing amount depends on the parameters of the nanostructure. For example, in Figure 6.2 (b), each nanorod is cylindrical with height h and radius r, and the nanorod filling ratio is p. Therefore, within the same probing area S, the total sensing surface will be $(1+2ph/r)\,S$. That is to say, if p=1/2, h=100 nm, and r=20 nm, the sensing surface area for analyte binding is increased by 5-fold.

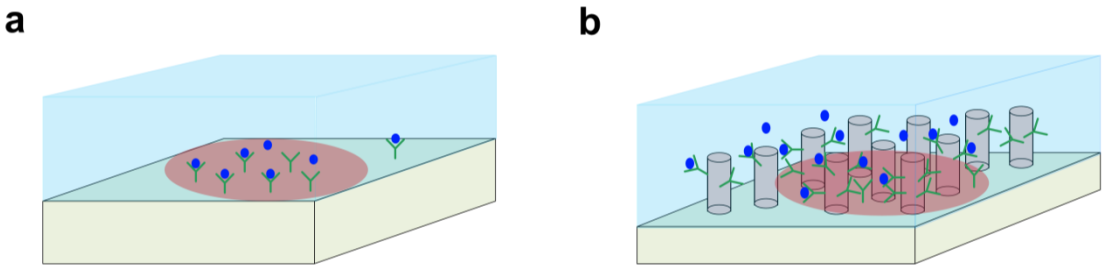

Figure 6.2 (a) A planar sensing surface; (b) a nanorod structure sensing surface. The red spot shows the area of the probe beam; the green *Ys* and the blue dots represent ligands and analytes.

If the nanorod size is smaller than the wavelength of the incident light, the features in this nanostructure do not scatter light, and the PC-TIR sensor still works well as a Fabry-Pérot resonator. In addition, the effective dielectric constant of the top layer ε_{eff} can be obtained from an effective medium theory of the Maxwell-Garnett type [110]:

$$\frac{\varepsilon_{eff}-\varepsilon_h}{\varepsilon_{eff}+\varepsilon_h}=f_i\frac{\varepsilon_i-\varepsilon_h}{\varepsilon_i+\varepsilon_h} \qquad (6.1)$$

where ε_i and ε_h are the dielectric constants of the inclusions (nanorods) and the host material (surrounding medium), respectively. The filling ratio of the inclusions satisfies the relation $f_i \in [0,1]$.

There are several methods to fabricate the nanostructure: nanoimprint lithography [111], electrochemical etching (for porous silicon-based structure) [104], chemical vapor deposition [112], glancing angle deposition (GLAD) [108], etc. Nanoimprint lithography is preferable due to its stability and reproducibility.

6.2.1.3 Compact system with angular modulation

In this dissertation work, I have built up an integrated system combining the white light spectra measurement for a large detection range and normalized intensity measurement for high detection resolution. It needs two light sources (white light source and single wavelength laser) and two detecting components (spectrometer and photodiode detectors). This system can be further optimized to a more compact one with angular modulation, which also provides a large range but uses the same laser as the normalized intensity measurement. It can be achieved with mechanical rotation and angular distribution. This work is being carried out by Chuck Divin.

As Figure 6.3 shows, we can use a rotator to change the incident angle of the collimated incident laser beam and to find the resonance dip.

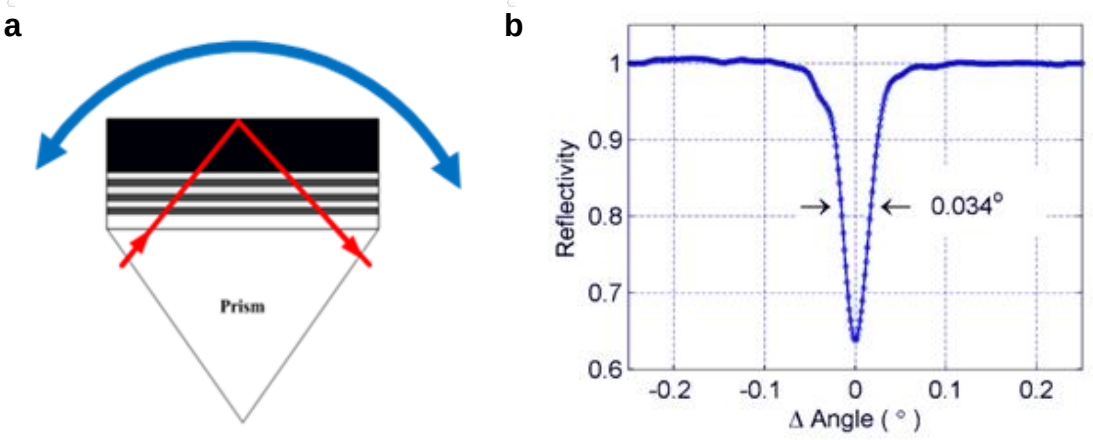

Figure 6.3 (a) Mechanical rotating the incident angle of the PC-TIR sensor; (b) the corresponding resonance dip.

We can also use a focused laser beam, including a wide range of angle distributions and a CCD camera to record the intensity of the reflected light, as Figure 6.4 shows. At the resonance angle, the light is absorbed most, so that the reflectivity spectrum appears as a narrow resonance dip (shown in Figure 6.4b). The ringing on one side could be explained by the propagation of the leaky mode (as discussed in Chapter 4).

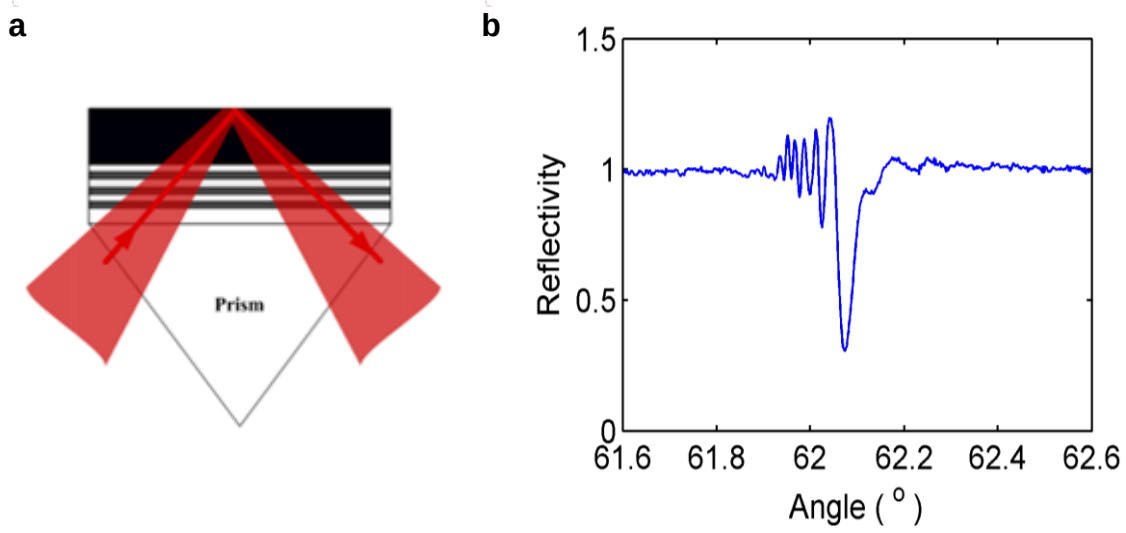

Figure 6.4 (a) A focused laser beam incident on PC-TIR sensor; (b) the corresponding resonance dip.

In addition, although it is convenient and easy to use a bulk prism to configure a total-internal-reflection geometry and to operate the PC-TIR sensor, it can also be equally well implemented in optical waveguide or fiber geometries (D-shaped fiber, cladding-off fiber, end-reflection mirror, angled fiber tip, tapped fiber, photonic crystal fiber, etc.), as in SPR-based sensors [113], which provides the advantages of miniaturization, compaction, a high degree of integration, and remote sensing capabilities.

6.2.2 Biological experiments

In most of the biological experiments of this dissertation, the high affinity streptavidin-biotin binding system was chosen since it is a standard model for biosensor characterization. However, transient and/or low affinity interactions are frequently the type that control cell function and thus are medically relevant and attractive targets for new drug development. The PC-TIR biosensor developed in this dissertation with its extraordinary sensitivity also opens up new possibilities in the characterization and study of these interactions, including the real-time characterization of low-affinity interactions,

transient complexes, small molecule drugs, and potentially greater affordability. With a well-developed fluidics system, the PC-TIR biosensor should be able to perform these studies. What we should do next is to choose suitable biological systems and perform experiments to validate its capability.

6.2.2.1 DNA base mismatch

In section 5.5.5, I investigated the hybridization of DNA oligonucleotide 20A to different lengths of T bases (biotin-10T, biotin-20T, biotin-30T and biotin-40T). In this case, the off rate was so low that it was not observed in the data shown in Figure 5.12. However, for low-affinity binding, the off rate will be such that it will be directly observable in real time. One interesting experiment worth conducting is to test different numbers of base mismatches while keeping the number of base pairs constant. For example, we can use 20T as the ligand adsorbed on the sensing surface (demonstrated before) and test the binding of the oligomer complements with base mismatches from 0 to 20 (for example, 20A, 19A1C, … 1A19C, 20C); this allows us to control precisely the binding affinity while keeping the molecular weight nearly constant. In addition, the binding affinity of specific combinations of base pairs can be calculated to validate the quantitative affinity obtained experimentally. Regenerating the ligand-immobilized surface between measurements will be helpful for a better comparison. It is also interesting to observe whether the PC-TIR biosensor has the ability to observe single-base-pair mismatches.

6.2.2.2 Measurements of small molecule, low affinity binding

In order to further evaluate the performance of the PC-TIR biosensor and highlight how it may be applied in a drug discovery setting, we could analyze the binding of a number of small molecule (sulfonamide-based) inhibitors interacting with the enzyme carbonic anhydrase II (CAII) [20]. The ligand CAII can be immobilized on the sensing surface via amine coupling, and the sulfonamide-based inhibitors are used as the analytes. As Table 6.2 shows, the molecular masses of the compounds varied from the highest mass of 341 Da for sulpiride to the lowest of 95 Da for methylsulfonamide, and their equilibrium constants K_D binding with CAII change from 19 nM for acetazolamide to 274 μM for methylsulfonamide.

Analytes	Molecular weight	Equilibrium constant K_D
Acetazolamide	222.2 Da	19 nM
Furosemide	330.7 Da	513 nM
Dansylamide	250.3 Da	760 nM
benzene-sulfonamide	157.2 Da	848 nM
carboxybenzene-sulfonamide	201.2 Da	893 nM
Sulfanilamide	172.2 Da	5.88 μM
Sulpiride	341.4 Da	186.2 μM
Methylsulfonamide	95.1 Da	274 μM

Table 6.2 Sulfonamide-based inhibitors' names, molecular weights and equilibrium binding constants with CAII.

This enzyme system has been commonly adopted to check the performance of commercial label-free optical instruments, such as the Biacore S51 [20], the Corning Epic$^{@}$ system [114], and the Fortebio Octet systems [115]. It is helpful for us to benchmark the performance of the PC-TIR sensor against these commercial systems.

At to this point, I have almost completed my Ph.D. dissertation. Starting from a new concept, I have fully developed an optical sensor system and demonstrated its extraordinary performances for label-free biosensing, especially for small molecule detection.

The proven power of the optical tools in biological research has inspired me to devote myself to the interdisciplinary research area and to discover more opportunities. In the following section, I will discuss a novel optical structure and its possible applications in several areas.

6.3 PC-metallic Structures and Applications

In this section, I propose and develop a novel photonic crystal-metallic structure, where a photonic crystal (PC) structure with an adjacent metallic structure is put in a total-internal-reflection (TIR) geometry. This unique configuration introduces a new plasmon excitation mechanism, and the excited plasmon modes satisfy the conditions for both resonance modes in the PC structure and plasmon modes in the metallic structure, which makes it possess many unique characteristics. Moreover, the incident light from a wavelength can be engineered to excite the plasmon modes and be greatly absorbed, reflected, and enhanced by the PC-metallic structure, which opens up a wide range of applications, including as an all-optical ultrasound transducer, for optical biosensing, and in enhanced total-internal-reflection fluorescence microscopy (TIRFM).

6.3.1 Introduction

Surface plasmons (SPs) have attracted tremendous interest in the past decade, both from a fundamental-physics perspective and as highly sensitive devices for optical detection of small biological or chemical entities [17, 18]. SPs are waves that propagate along the surface of a conductor, usually a metal film, and they are essentially *p* polarized light waves that are trapped on the surface because of their interaction with the free electrons of the metal. This part of light is further transferred into heat within the metal film and gets lost. This property is the basic mechanism of a surface plasmon resonance (SPR)-based biosensor. Normally the SPR sensor is made of a thin metal (gold or silver) film (~ 50 nm) on a glass substrate which is put on a total-internal-reflection geometry, as Figure 1 shows.

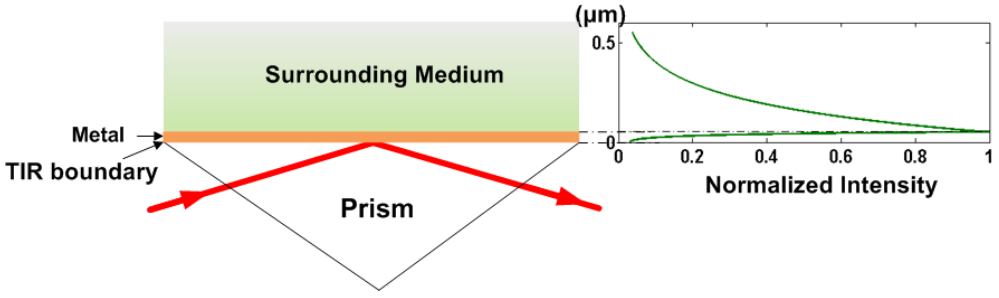

Figure 6.5 Schematic structure of an SPR sensor, and normalized field intensity distribution when light is resonant with the structure. The dash lines show the boundaries of the metal layer.

The surface plasmon modes can be excited in the configuration by phase matching. The field intensity is enhanced in the metal but decays both in the dielectric layer (substrate) and the surrounding medium. The excited surface plasmon mode can be characterized by a (very broad) resonance dip in the reflectance spectrum since this part of light is resonant and is absorbed in the very lossy metal film.

Besides bulk prism configuration in SPR sensors, optical waveguides, fibers, and gratings have also been developed to excite surface plasmon modes, and they offer the advantages of miniaturization, a high degree of integration, and remote sensing applications [113]. However, phase matching in these structures may be not easy to achieve. Skorobogatiy et al. proposed using a one-dimensional photonic crystal-based waveguide or photonic crystal fiber to get a Gaussian-like core mode [116] (as Figure 6.6 shows), which can be phase matched with a plasmon mode at any desired wavelength of operation (due to the property of the PC structure).

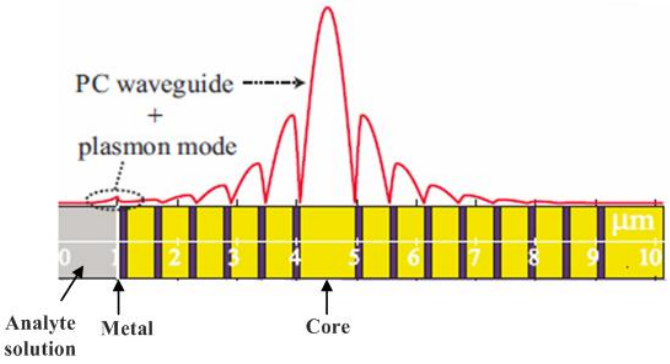

Figure 6.6 Schematic structure of a photonic crystal waveguide-based SPR sensor and the field intensity distribution. (from Skorobogatiy et al. [116]).

6.3.2 Novel plasmon excitation mechanism

Here I propose a novel plasmon excitation mechanism. Instead of sandwiching a core (defect) layer with two 1-D PC structures and putting the metal layer away from the defect layer, I use just one 1-D PC structure (with a non-absorbing defect layer) and an adjacent metallic structure on the top and put it in a total-internal-reflection geometry (Figure 6.7). The total internal reflection happens between the defect layer and the metallic structure, and a Fabry-Pérot microcavity forms in the defect layer due to the high

reflectivity provided by both the PC structure and the TIR boundary, of which some of the resonance mode could be used to excite the plasmon mode in the metallic structure. Either *s* polarized or *p* polarized light is possible for the excitation. However, the 1-D PC structure has a much larger light confinement for *s* polarization than *p* polarization, which makes the latter preferable since it makes it easier to choose a suitable thickness for the lossy metallic structure.

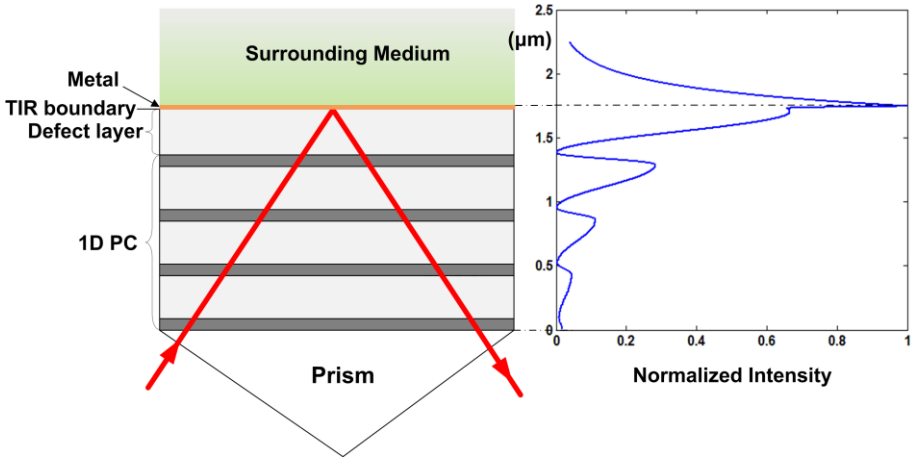

Figure 6.7 PC-metallic structure and normalized field intensity distribution when light is resonant with the structure. The dotted line shows the TIR boundary.

The excited plasmon mode has to satisfy the conditions for both the existence of the resonance mode in the Fabry-Pérot cavity and the plasmon mode in the metallic structure; therefore, its width can be much narrower than that of an SPR-based sensor. In addition, the simulation shows that the field intensity distribution of the mode meets these two conditions. Without the metallic structure, the field intensity in the PC-defect structure gets the largest enhancement in the defect layer and decays in the evanescent region (Figure 2.9); with only the metallic structure, the field intensity is enhanced within the metallic structure but decays on both sides (Figure 6.5); however, with the metallic structure adjacent to the PC-defect structure, the profile of the field intensity enhancement combines the properties of these two: the field intensity is first enhanced by the PC structure and gets a large enhancement in the defect layer, then is further enhanced in the metallic structure, and finally decays in the evanescent region (Figure 6.7). In this way, the PC-metallic structure can have a much larger enhancement on the

interface between the device and the surrounding medium than the structure in Figure 6.6, where the metal layer is away from the core (defect) layer.

The enhanced field intensity is attractive to intensity-related measurements, such as fluorescence or Surface-Enhanced-Raman-Scattering measurements, and others. Moreover, by choosing a suitable PC structure and the metal layer thickness, we can cause light from specific wavelengths to be totally absorbed by the PC-metallic structure. On one hand, the absorbed light (for example, a laser pulse) is further transferred into heat which can be used to generate an ultrasound signal in sensitive polymer materials such as polydimethylsiloxane (PDMS) by a thermo-elastic effect [117, 118]; on the other hand, a fundamental resonance dip appears in the reflectance spectrum corresponding to the excited mode (the absorbed part), which can be used for ultrasound detection [119, 120], such as etalon sensors, or be used as optical biosensors such as SPR-based sensors.

In addition, operating the PC-metallic structure in a total-internal-reflection geometry provides several other advantages compared to the devices operating at normal incidence: 1) the resonance wavelength of the PC-metallic structure can be easily adjusted by the incident angle; 2) fewer PC layers are required; 3) it provides an open surface that can be easily accessed by analytes or targets; 4) TIR configuration gets rid of unwanted transmitted light or noise.

6.3.3 Experimental demonstration

In order to experimentally prove this concept, I designed and fabricated the structure as follows: substrate / TiO_2 / $(SiO_2/TiO_2)^3$/ X / Ag. For a desired resonance wavelength to be 632.8 nm, the 1-D PC structure was made of alternating a 87-nm TiO_2 layer and a 286.5-nm SiO_2 layer; the "defect" layer X was composed of another 390-nm SiO_2 layer, and the metallic structure was a 20-nm Ag layer on the top. The whole structure was fabricated by electron beam deposition on a flat BK-7 glass substrate. The refractive indices of the substrate, TiO_2, SiO_2, Ag and de-ionized (DI) water at λ = 632.8 nm, were n_s = 1.515, $nTiO_2$ = 2.232, $nSiO_2$ = 1.451, nAg = 0.059 + i 4.279, and n_t = 1.333, respectively.

The PC-metallic structure was put on a prism (made of BK-7 glass) with index-matching liquid. A white light from a lamp was collimated first, passed through a polarizer to get *p* polarization light, and then injected on the prism. The reflected light was measured by a spectrometer. Figure 6.8 (a) shows the reflectance spectra of the PC-metallic structure when the incident angle in the substrate was 65° and the top sensing surface was covered by DI water. The reflectance dip was in good agreement with a simulation using a transfer matrix calculation. It has a resonance wavelength of 632.8 nm and a resonance width of $\Delta\lambda$ of 25.2 nm (smaller than the 40 nm of an SPR sensor using a pure Ag layer) and small minimum reflectance R_{min} of 0.05. Moreover, the reflectance spectrum near the resonance can be fit reasonably well by a Lorentzian lineshape, similar to a Fabry-Pérot mode. In addition, when the incident angle changes, the resonant wavelength shifts in order to satisfy the resonance conditions, as Figure 6.8 (b) shows.

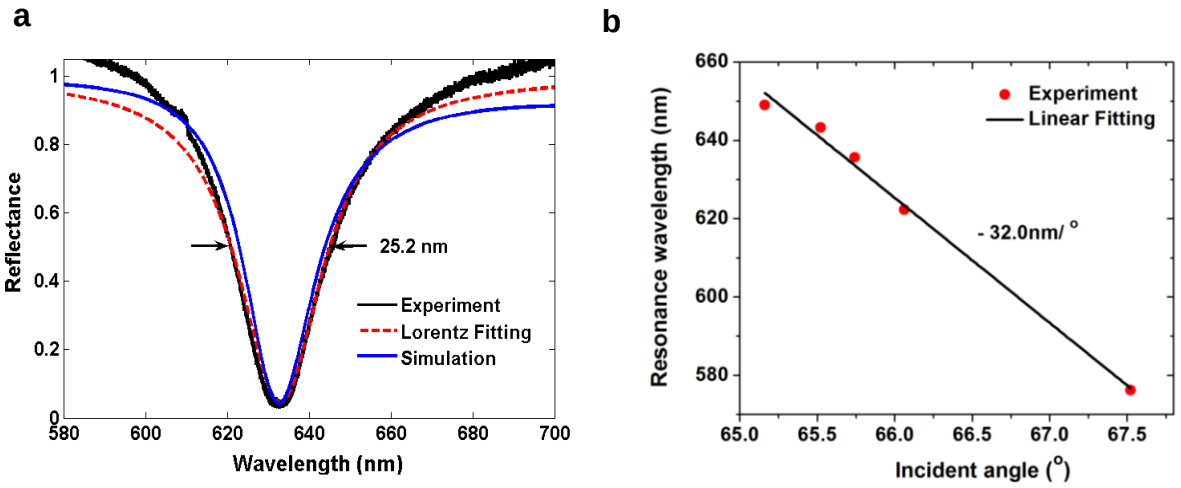

Figure 6.8 (a) The experimental, Lorentzian fitting and simulated reflectance spectra of the PC-metallic structure in TIR; (b) resonant wavelength shifts with incident angle changing.

The results verified that a 1-D PC structure (with a defect layer) could be used to excite a plasmon mode in the adjacent metallic structure. Moreover, it showed that the light from a desired wavelength could be totally absorbed in the metal (R_{min} = 0), that the resonance wavelength shifted with a resonance conditions change (e.g., incident angle, etc.), and that the resonance width became narrower than those of normal SPR sensors, which could be further optimized by increasing the number of the PC dielectric layers and decreasing the thickness of the metal layer.

It is an innovative idea to use a PC-metallic structure to excite plasmon modes in a TIR configuration, since this introduces a new mechanism and opens up a whole new range of applications. In the following, I will discuss some applications in details. As shown above, a large absorption of light at a specific wavelength can be used for strong ultrasound generation; a narrow and deep resonance dip can be used for sensitive ultrasound detection or biomolecular sensing; and high field enhancement can be used for total-internal-reflection fluorescence measurement.

6.3.4 All-optical ultrasound transducer

There is a strong demand that high-resolution imaging techniques obtain comprehensive morphological and functional information of important biological or industrial samples. Currently, the unavailability of two-dimensional (2-D) high-frequency transducer arrays (> 50 MHz) is a major bottleneck preventing further development of high-frequency ultrasound, especially in real-time 3-D high-resolution applications [118]. Piezoelectric ultrasound transducers are the currently dominant products on the market. Piezoelectric technology uses electronic signals to generate and detect ultrasound in piezoelectric materials (such as ceramic). It is mature for arrays operating at less than 10 MHz, but it is extremely difficult to produce 2-D arrays operating above 20 MHz. The major problems for piezoelectric technology include the difficulty of cutting piezoceramic materials to micrometer-scale elements in order to get high frequency ultrasound, electrical connections to small elements, crosstalk between elements, and increased detection noise with reduced element size, as well as the lack of quality high frequency materials and electronics.

Using optical methods to generate and detect ultrasound is an attractive technology and has been investigated for years [122]. However, most of the optical methods could only generate or detect high frequency ultrasound on separate transducer elements. The current state-of-the-art, all-optical ultrasound transducer was based on a two-dimensional gold nanostructure [119]. It can absorb 30% of the light energy of a laser pulse for ultrasound generation and transmit 90% at the wavelength of a probe laser so that it can be part of a Fabry-Pérot cavity for ultrasound detection, which allows an optoacoustic generator and detector to be integrated into the same transducer. Although this single-

element transducer achieved a broad bandwidth of ~ 57 MHz and a resolution of ~ 38 μm, its fabrication process is much more complicated and expensive than with piezoelectric technologies, and its ultrasound generation efficiency is low (~ 30%) and the detection sensitivity is not high.

The innovative PC-metallic structure provides many unique advantages in high frequency ultrasound generation and detection. It can act as an ideal ultrasound transmitter which absorbs 100% of the energy of the laser pulse to generate a stronger broad-band ultrasound signal than the complicated 2-D gold nanostructures; at the same time, it can be used as a high-sensitivity optoacoustic receiver to the reflected ultrasound. Moreover, our device has a simple configuration which is very easy to fabricate with current fabrication technology and with low cost.

In the following, I will discuss in detail how to use the PC-metallic structure to develop an ultrasound transmitter, an ultrasound receiver, and an integrated all-optical ultrasound transducer.

6.3.4.1 Optoacoustic transmitter (generator)

A variety of mechanisms have been studied for the optical generation of ultrasound, and the most common and efficient one is the thermoelastic effect, where the key component is a light-absorbing film deposited on a transparent substrate. The biggest advantage of the thermoelastic effect is that the acoustic pressure in the far field is proportional to the time derivative of the laser pulse, meaning that the center frequency and bandwidth of the generated ultrasound is mainly determined by the incident laser pulse; thus, acoustic waves with desired properties can be achieved simply by modulating the optical input.

Previous studies of thermoelastic expansion for the optical generation of ultrasound had concentrated on utilizing metal films to generate acoustic waves because they are effective optical absorbers. However, their thermal expansion coefficients are generally low, in the range of $0.1 \sim 0.2 \times 10^{-4}$/K, which limited the transduction efficiency [123]. Obviously, high transduction efficiency can be significantly improved by using materials with higher thermal expansion coefficients, such as polydimethylsiloxane (PDMS),

which has a coefficient of 3.1×10^{-4}/K, more than ten times higher than common metals. However, PDMS is a transparent polymer, thus it does not absorb optical energy. Hou et al. used a spin-cast film consisting of a mixture of carbon black and PDMS where carbon black was used as the optical absorber and increased the optoacoustic conversion efficiency by more than 30 dB, compared to a metallic film [118]. However, the increased viscosity due to mixing PDMS with carbon black limits the spin-cast film thickness to 11 μm, which restricted the bandwidth and amplitude of the generated ultrasound because only 1 μm of the PDMS layer from the substrate contributed to the thermoelastic effect and other overlying PDMS just attenuated the generated ultrasound by roughly 1 dB/μm. Furthermore, Hou et al. developed a 2-D gold nanostructure as an optical absorber with a 3~4 μm PDMS film. Although it had low light absorption efficiency (~30%), it improved the generated optoacoustic bandwidth to 57 MHz and acoustic surface pressure to 100 MPa [117,119].

As described above, the innovative PC-metallic structure can be designed to absorb 100% of the optical energy of specific wavelengths in a TIR geometry. With one more thin PDMS layer on top of the metallic structure as shown in Figure 6.9 (a), it can act as a perfect ultrasound generator.

In order to demonstrate it, I collaborated with Sung-Liang Chen and Hyoung Won Baac from Professor Jingjie Jay Guo's group, and performed the experiments. The pulsed laser we used was 532 nm wavelength, 10 ns pulse duration width and 20 Hz repetition rate. Then we designed and fabricated the structure as follows: substrate / TiO_2 / $(SiO_2/TiO_2)^3$/ X / Ti / Au/ PDMS. The 1-D PC structure was made of pairs of alternating 87-nm TiO_2 layer and 286.5-nm SiO_2 layer; the "defect" layer X was composed of another 165-nm SiO_2 layer, and the metallic structure was a 15-nm gold layer with 1-nm Ti film to increase the adhesion between the SiO_2 and the gold. The structure was fabricated by electron beam deposition on a flat BK-7 glass substrate. After that, a 2.03-μm PDMS transparent film (adjacent to the gold layer) was spin-coated on top of the whole structure.

The PC-metallic structure was put on a prism via index-matching liquid. When the incident angle in the substrate was 64^o and the top surface was covered by DI water, we

measured the reflectance spectrum with a white light source (*p* polarization) and a spectrometer (as Figure 6.9b shows). Although there were some differences between the experimental results and the simulation for the 2nd or 3rd dip due to the non-uniformity of the spin-coated PDMS film, the first dip at 532 nm fit the simulation well, and the reflectance was 10%, which meant that about 90% of the light from the wavelength of 532 nm was absorbed.

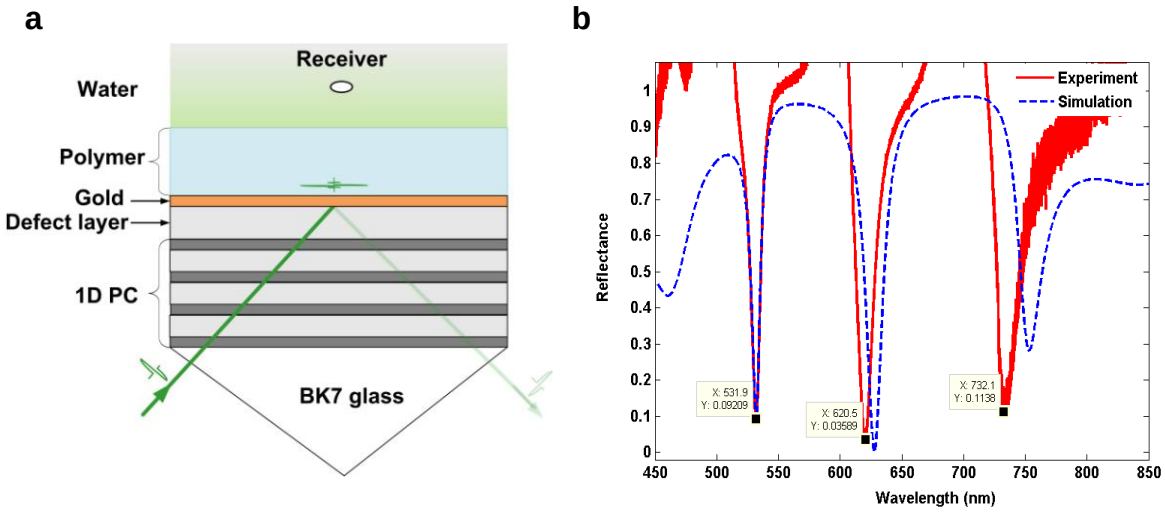

Figure 6.9 (a) Schematic structure of ultrasound generation using a PC-metallic device; (b) the experimental and simulated reflectance spectra of the structure.

Then we changed to the pulsed laser (532nm, 10 ns) and performed a series of experiments to check the generated ultrasound signal.

1) We used a standard piezoelectric transducer (20 MHz, flat) as the ultrasound detector to calibrate the generated acoustic amplitude. The probe beam's diameter size was 1 mm and the transducer in DI-water was 1.5 mm far from the PDMS surface. After being amplified by 32 dB, the detected signal was directly recorded without average and is shown in Figure 6.10 (a). When the laser wavelength 532 nm was out of the resonance dip (off-resonance), there was no light absorbed in the structure, so no ultrasound was generated as expected; when the laser wavelength 532 nm was on resonance, about 90% of the injected laser pulse energy was absorbed and used to generate ultrasound. A very strong ultrasound signal was observed, as Figure 6.10(a) shows, and the generated acoustic pressure (amplitude) at the far field was linearly proportional to the power of the laser-pulsed energy (Figure 6.10b). That means that we can always achieve a much

higher acoustic pressure by increasing the pulsed laser power.

As a matter of fact, this is a big advantage for our system. Because the PC-metallic structure is in a total-internal-reflection geometry, with most of the incident light absorbed by the structure, the extra part is reflected back and there won't be any light injecting on the object away from the top, which means that a large laser pulse power would not do harm to the object; on the contrary, in most of the current optoacoustic methods, the laser pulse is normally injected on the film or human objects. Due to poor light absorption efficiency, a little part of the light is absorbed, but most of the light transmits through the film and injects onto the object, which may cause damage to it. The maximum permissible pulse energy and the maximum permissible pulse repetition rate are governed by the ANSI laser safety standards, which are typically at least an order of magnitude less than the damage thresholds. From this point of view, the ultrasound transducer based on the PC-metallic structure is more practical for applications.

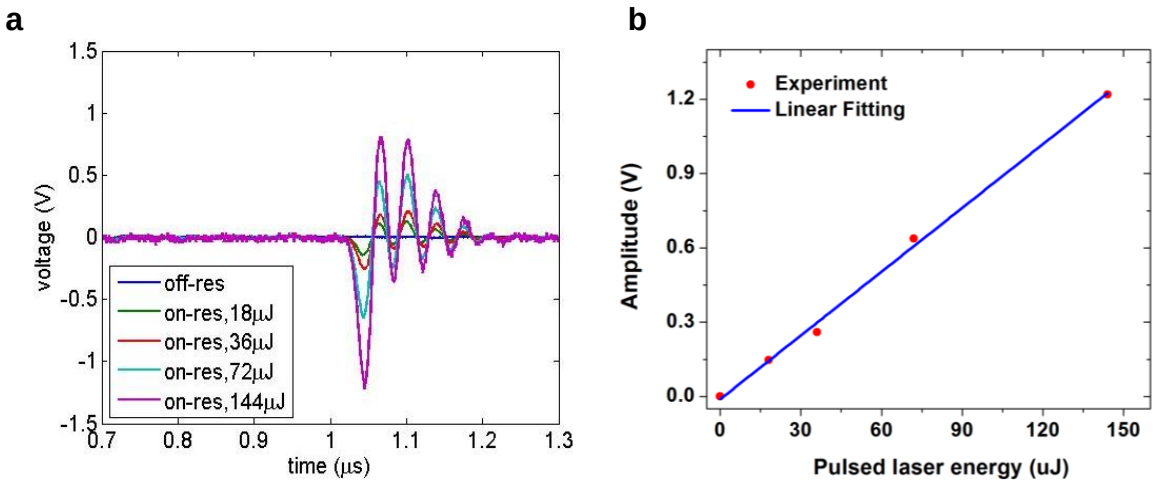

Figure 6.10 (a) Generated ultrasound signal with different input pulse laser energy; (b) the relationship between the generated ultrasound amplitude and the input pulse laser energy.

2) We used a polymer microring resonator as the ultrasound detector to calibrate the generated acoustic spectrum and pressure. The polymer microring resonator was demonstrated to have high ultrasound detection sensitivity and a wide detection bandwidth of over 90MHz at -3 dB [124]. Since the microring resonator size was very small (~100 μm) and was sensitive to the ultrasound from different angles, the position relative to the generator surface was critical. Here we tested the generated ultrasound

with different laser spot sizes (diameter 1 mm & 5 mm) with the same incident optical fluence (23mJ/cm^2). With the amplification of 16 dB by a photodetector, the ultrasound signal was directly recorded without average. The high SNR indicates that strong ultrasound was generated (Figure 6.11).

The measured signal amplitude was 0.72 V for a 1 mm spot size, so the original signal was 18 mV without amplification. Considering that the microring had a sensitivity of 150 pm/MPa and the microring resonance dip shifts 36 pm with the slope of 0.5 mV/pm, we calculated that the acoustic pressure at 1.16 mm was 240 kPa. Taking into account the attenuation in water (0.0022 dB/cm/MHz^2), the acoustic pressure at 10 mm was about 28 kPa, which was one order of magnitude higher than the 2-D gold nanostructure film (the current state-of-the-art result) [117].

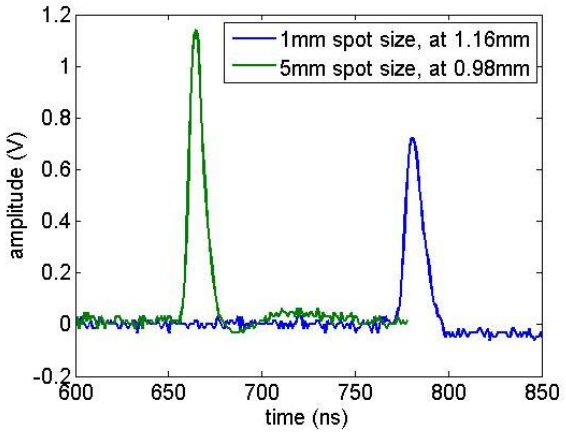

Figure 6.11 Generated ultrasound signal measured by polymer microring resonator with 1 mm and 5 mm probe spot sizes.

We also analyzed the generated ultrasound spectrum and compared it with that of the pulsed laser, as Figure 6.12 shows. The generated ultrasound spectrum was close to that of the laser pulse and had ~50 MHz bandwidth at -6 dB. Much broader bandwidth could be achieved with a narrower laser pulse (e.g., 2 ns for 250 MHz bandwidth at -6 dB).

In summary, we have developed a novel and ideal ultrasound transmitter based on a PC-metallic device in a TIR configuration, which requires us to use a thin and suitable polymer film to achieve large light absorption efficiency and to generate broad-band, high-pressure ultrasound. What is more, it is very promising for much higher and much broader ultrasound generation for practical applications.

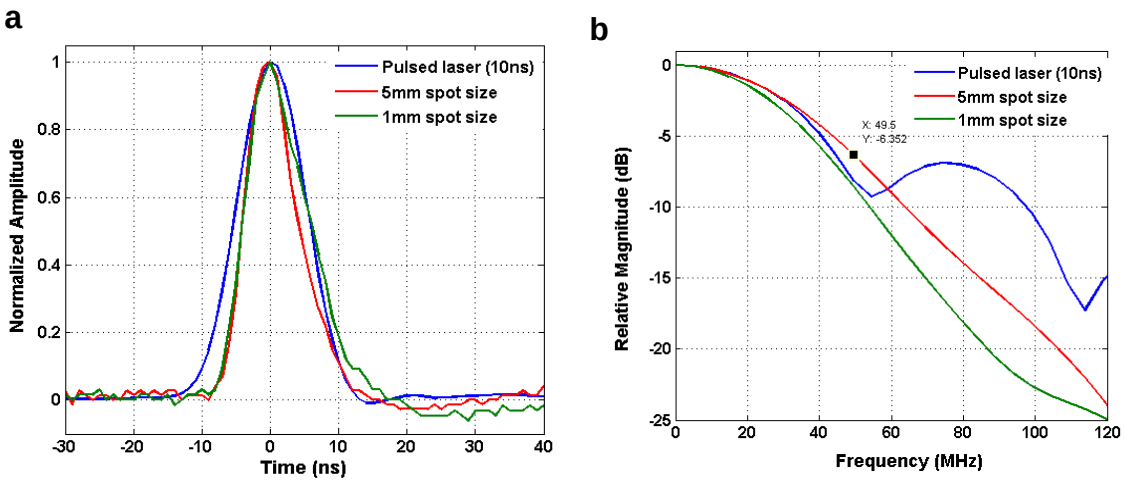

Figure 6.12 Comparison between laser pulse and detected ultrasound for (a) signal and (b) spectrum.

6.3.4.2 Optoacoustic receiver (detector)

As shown above, we used a piezoelectric transducer and a microring resonator as ultrasound detectors to calibrate our ultrasound generator. As a matter of fact, the structure we developed can also be used as the ultrasound detector, which provides many significant advantages compared to those that are currently available.

An ideal ultrasound detector should be highly sensitive to a broadband ultrasound. However, traditional piezoelectric detectors have the problems described above and are limited to a frequency below 20 MHz. In order to overcome the difficulties, the optical detection of ultrasound has been studied as a promising alternative technology, one which can detect higher frequency (several tens of MHz), accomplish small detection size using optical focusing (a few tens of microns), and form an array using optical multiplexing.

One of the most effective optoacoustic detection methods is to utilize an etalon structure, also called a Fabry-Pérot interferometer (FPI) [120]. Normally it consists of a transparent slab (cavity layer) placed between two partially reflecting mirrors. However, there is always a trade-off between the high finesse and the large ultrasound modulation for the etalon sensor, and it is impossible to combine a polymer film with high acoustic sensitivity as the cavity layer and a high-reflection dielectric coating to optimize the sensitivity of ultrasound detection.

In contrast, the PC-TIR configuration we studied creates a unique structure with an open cavity, overcoming the limitations of the etalon sensors, and allows choosing a wide range of materials as the cavity layer for high acoustic modulation sensitivity and having a 1-D PC structure (that is, dielectric multilayers) and a TIR boundary as the high reflectors to provide high finesse at the same time. Moreover, much thin film can be used, which decreases the ultrasound propagation attenuation. The high finesse of the PC-TIR sensor has been verified in our previous experiments for biomolecular detection, which had a narrow resonance width ~ 1 nm with silica as the cavity layer; and the PC-TIR sensor was also demonstrated as being an effective ultrasound receiver with a broad bandwidth (> 120 MHz), having Polymethyl-methacrylate (PMMA) as the cavity layer and *s* polarization light as the probe beam [61]. However, this PC-TIR optoacoustic detector suffered some limitations: first, a small amount of light-absorbing dye had to be incorporated into the PMMA cavity layer in order to characterize the resonance mode, but the dye amount was very hard to control to get a sharp resonance dip (usually the effective extinction coefficient for the defect layer needed is $\sim 10^{-5}$ for several micrometer thickness, or even less if considering scattering loss); second, the probe laser beam size was large, 0.5 mm, which limited the detector element size and thus the detection resolution.

However, the novel PC-metallic structure in the TIR configuration not only possesses the advantages of the PC-TIR sensor but also solves its limitations, which provides many significant advantages as a highly sensitive and broad-bandwidth ultrasound receiver. In the following, I discuss several parameters of this PC-metallic ultrasound receiver, including detection sensitivity, frequency response and effective element size.

A. Sensitivity

When an ultrasound signal reaches the PC-metallic sensor (Figure 6.13a), the ultrasonic pressure wave changes the optical thickness of the structure, especially of the top polymer layer. This results in a change of resonance wavelength, thus altering the reflected laser intensity with the laser wavelength tuning to the steep portion of the resonance dip, as Figure 6.13(b) shows. The detection sensitivity of a PC-metallic sensor

depends on two figures of merit: the conversion efficiency of the resonance wavelength shift to the optical intensity change (optical sensitivity O_s) and the conversion efficiency of the acoustic pressure to the resonance wavelength shift (acoustic sensitivity A_s).

The optical sensitivity O_s is defined as the optical power modulation per unit wavelength shift ($\mu W/nm$) at the bias λ_0 of the PC-metallic sensor, and the maximum optical sensitivity is given by (as Equation 2.26)

$$O_s\big|_{\max} = \left[\frac{dI_r}{d\lambda}\right]_{\lambda_0}\Big|_{\max} = \pm 1.3 I_0 \bullet \frac{1-R_{\min}}{\Delta\lambda} \qquad (6.2)$$

where I_0 is the incident laser intensity, and R_{min} and $\Delta\lambda$ are the minimum reflectance and the FWHM of the resonance dip, respectively. Therefore, O_s is dependent upon the incident laser power and the finesse of the cavity of the PC-metallic sensor.

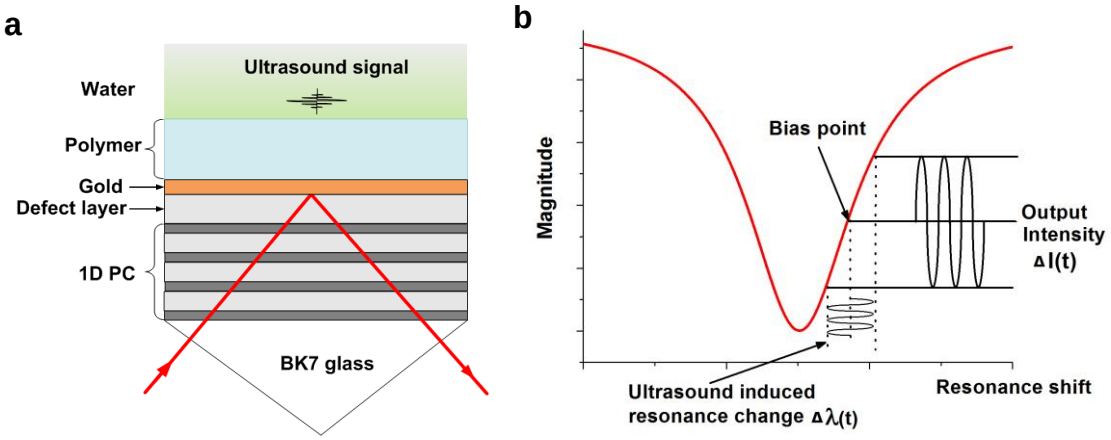

Figure 6.13 (a) Schematic structure of ultrasound detection using a PC-metallic device;
(b) illustration of operating principle using a resonance shift for ultrasound detection.

On the other hand, the acoustic sensitivity A_s represents the magnitude of the resonance wavelength shift produced per unit of acoustic pressure (*nm/MPa*), which is the product of the resonance shift sensitivity to the optical thickness change B_S (*nm/nm*) and the acoustic pressure sensitivity to the polymer optical thickness change P_S (*nm/MPa*). The first one, B_S, is related to the whole structure and can be calculated by transfer matrix simulation, and the latter P_S can be expressed as:

$$P_s = \frac{\delta d}{\delta P} = \frac{\delta \varepsilon}{\delta P} \bullet d = -\frac{d}{E} \qquad (6.3)$$

where ε is the strain due to acoustic pressure on the polymer layer, E is the Young's Modulus of the polymer material, and d is the thickness of the polymer layer.

Therefore, the maximum overall sensitivity S ($\mu W/MPa$) of the PC-metallic sensor is given by the product of I_s and A_s:

$$S_{\max} = \frac{dI_r}{dP} = \frac{dI_r}{d\lambda}\frac{\partial\lambda}{\partial P} = O_s \bullet A_s = \mp 1.3 I_0 \bullet \frac{1-R_{\min}}{\Delta\lambda} \bullet \frac{d}{E} \bullet B_S \qquad (6.4)$$

In order to achieve high sensitivity of the ultrasound receiver, we need high incident laser intensity, a narrow and deep resonance dip (small R_{min} and $\Delta\lambda$), large polymer thickness and resonance shift sensitivity, and polymer material with low Young's modulus. For example, for the experimental structure shown in Figure 6.9, $R_{min} \sim 0$, $\Delta\lambda$ = 20 nm, d = 2.03 μm, B_S = 0.13 *nm/nm,* and E = 5 *MPa* for PDMS, then the ultrasound detection sensitivity S_{max} is 3.4×10^3 $\mu W/MPa$ when the incident laser intensity I_0 = 1 mW. It is about 3 times higher than the state-of-the-art microring detector [124] that is 20 times more sensitive than a commercial product (75 μm piezoelectric polyvinylidene fluoride (PVDF) transducer) [HPM075/1]. What is more, we can easily improve the detection sensitivity over 10 times by optimizing the PC-metallic structure to get narrow resonance.

B. Frequency response

The frequency response is an important characteristic parameter for an ultrasound detection system. Since the elastic displacement due to the acoustic pressure is mainly from the thickness change of the polymer layer, the frequency response is dependent upon the acoustic properties of the film, the backing material, and the surrounding media (usually water). The frequency-dependent modifying term $P_I(k)$ can be obtained by considering the mean distribution of stress P_T across the thickness d of the polymer layer due to an incident acoustic wave:

$$P_I(k) = \frac{1}{d}\int_d P_T dy \qquad (6.5)$$

where $k = 2\pi f / v$ is the acoustic wave number, f is the acoustic frequency, and v is the ultrasound wave traveling speed in the polymer layer. Further, the frequency-dependent term can be derived as [120]:

$$\left|P_I(k)\right| = \frac{T\sqrt{2}}{kd}\sqrt{\frac{(R_1^2 + 2R_1\cos(kd)+1)(1-\cos(kd))}{(R_1R_2)^2 - 2R_1R_2\cos(2kd)+1}} \qquad (6.6)$$

where T is the pressure-amplitude transmission coefficient resulting from the acoustic-impedance mismatch between the spacer layer and surrounding media, R_1 and R_2 are the pressure-amplitude reflection coefficients at the two surfaces of the film, and

$$T = \frac{2Z}{Z+Z_2},\ R_1 = \frac{Z_1 - Z}{Z_1 + Z},\ R_2 = \frac{Z_2 - Z}{Z_2 + Z} \qquad (6.7)$$

where Z is the acoustic impedance of the polymer sensing film, and Z_1 and Z_2 are the acoustic impedances of the backing media and surrounding media.

Therefore we can get the response spectrum for each frequency, which is mainly related to the polymer sensing film's impedance and thickness. Here we simulate the response spectrum of the PC-metallic structure shown in Figure 6.13(a) with two polymer materials, PDMS and PMMA with different thicknesses (1 ~ 4 μm), then Z = 1.9 $\times 10^6$ Kg/m^{2}s for PDMS or 3.23×10^6 Kg/m^{2}s for PMMA; $Z_1 = 63.8\times10^6$ Kg/m^{2}s for gold; $Z_2 = 1.483\times10^6$ Kg/m^{2}s for water, and the acoustic velocities are 1000 m/s, 2740 m/s, 3240m/s and 1480 m/s for PDMS, PMMA, gold and water, respectively. The results are shown in Figure 6.14. It shows that a larger acoustic impedance material (that is, larger Young's Modulus) detects a larger frequency response, as does a thinner sensing film thickness. There is a trade-off between the sensitivity and the frequency response of the ultrasound detector using the PC-metallic structure in TIR with polymer film. In other ways, we could choose suitable polymer material and thickness for specific requirements. For example, we can use a 2-μm PDMS layer to detect a 200MHz high frequency ultrasound signal within -6 dB range, with a large sensitivity, $3.4\times10^3\ \mu W/MPa$.

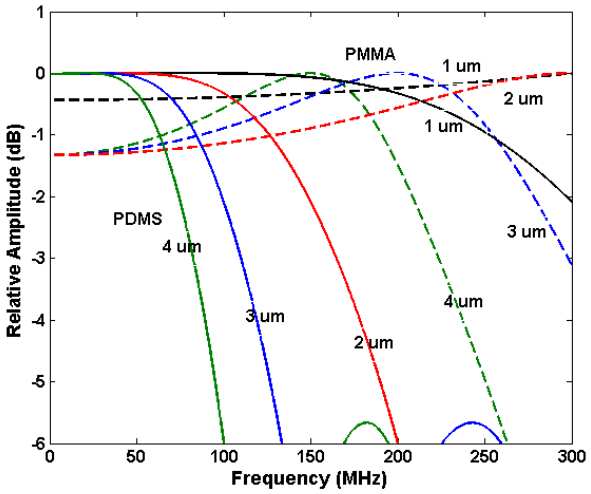

Figure 6.14 Normalized frequency response of a PC-metallic structure with different thicknesses of PDMS (solid line) and PMMA (dash line) as the sensing film.

C. Effective element size

The effective element size is a measure of the acoustic aperture of a receiver. Its effect on lateral spatial resolution makes it a key parameter in an ultrasonic measurement and imaging system. Normally the spot size of the focused probe laser determines the effective element size and then the spatial resolution, which can be smaller to several micrometers. However, the focused probe's resolving a small spot on the detector requires a large range of spatial frequencies, corresponding to the angular spread of the illuminating beam, which will broaden the resonance mode width. As shown in Equation 6.5, the overall detection sensitivity of our sensor will decrease (similar to etalon detectors). There is always a tradeoff between detection sensitivity and element size.

We compared the effect of the focused beam on the resonance dip for a PC-TIR sensor which runs with *s* polarization and has a very narrow resonance (FWHM ~ 0.003^{o}) mode, and for a PC-metallic structure which runs with *p* polarization and has a broad resonance mode (FWHM ~ 0.5^{o}). As Figure 6.15 shows, the PC-metallic structure is more flexible in its ability to use a small spot size for high spatial resolution detection, with reasonable decreasing of the detection sensitivity. Moreover, if we use the PC-metallic structure for an all-optical ultrasound transducer, the whole sensitivity can be improved by generating strong acoustic pressure with a high-power laser pulse.

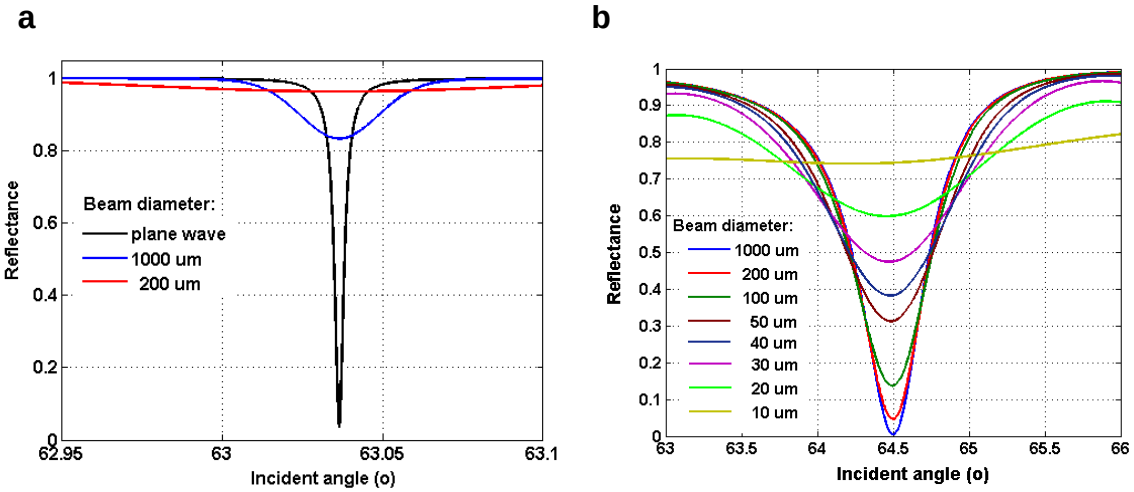

Figure 6.15 (a) Effect of focus beam on narrower resonance width (for PC-TIR sensor); (b) effect of focused beam size on larger resonance width (for PC-metallic sensor).

In summary, we have developed a sensitive, broad-band ultrasound receiver based on a PC-metallic structure in a TIR configuration. With an open cavity, this PC-metallic sensor provides many advantages over a conventional etalon sensor such as a PC-TIR optoacoustic detector [61], but it is more promising to get better overall performance than a PC-TIR sensor.

6.3.4.3 All-optical ultrasound transducer

In the previous two sections, we discussed the development of the PC-metallic structures for ultrasound generation and ultrasound detection, separately, and both of them can compete with state-of-the-art ultrasound transmitters and detectors, respectively. Moreover, the biggest advantage for our PC-metallic structure is that we can integrate an ultrasound transmitter and a receiver on the same structure and develop a broad-band, highly sensitive, all-optical ultrasound transducer.

Figure 6.16 (a) shows the concept of the all-optical ultrasound transducer using a photonic crystal structure with gold and polymer films on the top. A pulsed laser is used to generate an ultrasound signal, which then transmits onto objects in water; then the ultrasound wave is reflected by the objects and back to the polymer. This causes strain in the polymer, which is monitored by a CW laser operating at the large slope region of a resonance dip of the structure. By monitoring the reflected CW laser intensity change, we can get the reflected ultrasound signal and then the information of the object.

There are two ways to run the integrated system: we can either design the PC-metallic structure to have a resonance dip at the wavelength of the pulsed laser for ultrasound generation and can then tune the incident angle to make the resonance dip close to the CW laser for ultrasound detection, as Figure 6.16 (b) shows; or if the wavelengths of the pulsed laser and the CW laser are far away from each other, we can control the thickness of the polymer film to get multiple resonance dips, as Figure 6.9 (b) shows, and then pick one for the pulsed laser (e.g., 532 nm) and another one for the CW laser (e.g., 632.8 nm). The properties of the photonic crystal structure and total internal reflection geometry make the whole structure operate easily at the same area for both wavelengths just by our changing the incident angle.

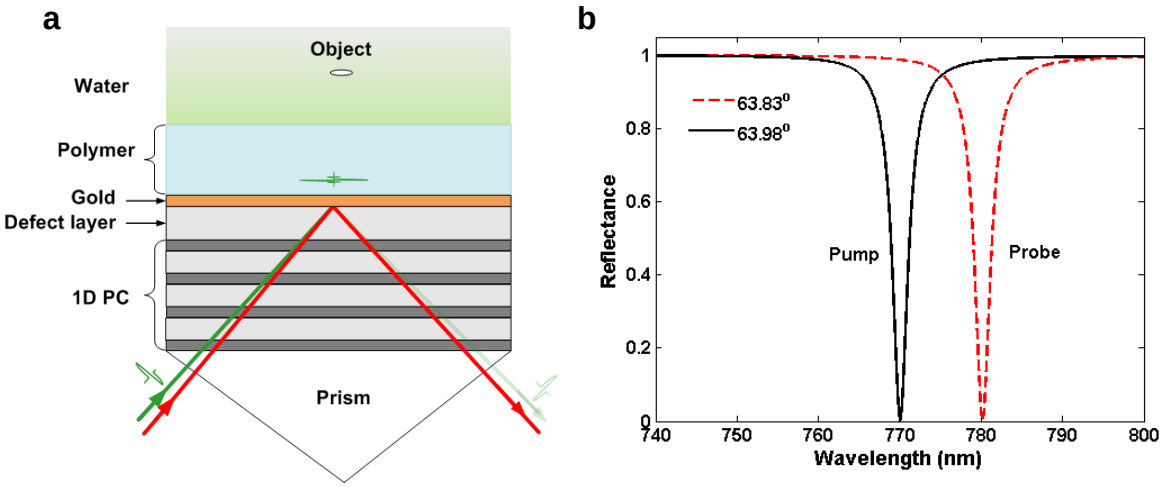

Figure 6.16 (a) Schematic structure of an all-optical ultrasound transducer based on PC-metallic structure; (b) the resonance dip can be tuned to a suitable wavelength by changing the incident angle of the laser beams.

As an integrated system, we need to consider both ultrasound generation and detection and to choose suitable parameters to get good comprehensive performance. As we discussed above, for ultrasound generation, we need an effective light absorber and a large thermal expansion coefficient polymer material, and we also need to design the PC structure, defect layer thickness, and polymer layer thickness to get the largest absorption at the wavelength of the pulse laser. Moreover, the polymer thickness should be thin (1~ 4 μm) so that it won't attenuate a generated optoacoustic signal. For ultrasound detection, we need low Young's modulus polymer material to get a large strain; high acoustic impedance and thin polymer thickness for a high frequency response; a large product of

polymer thickness and binding sensitivity; and a suitable focus beam for smaller element size. There is always a trade-off for all these parameters, but we can also choose suitable parameters for specific requirements.

There are several ways to achieve a narrow and deep resonance dip for highly sensitive ultrasound detection. For example, for the structure: substrate/TiO_2 / $(SiO_2/TiO_2)^N$ / SiO_2 / gold / PDMS, there is another Fabry-Pérot cavity formed in the PDMS layer, as Figure 6.17(c) shows. Therefore, the resonance dip becomes narrower with a thicker polymer layer (Figure 6.17a&b). Moreover, by increasing the number of multiple dielectric layers N and decreasing the thickness of the gold layer, we can get a much narrower resonance dip.

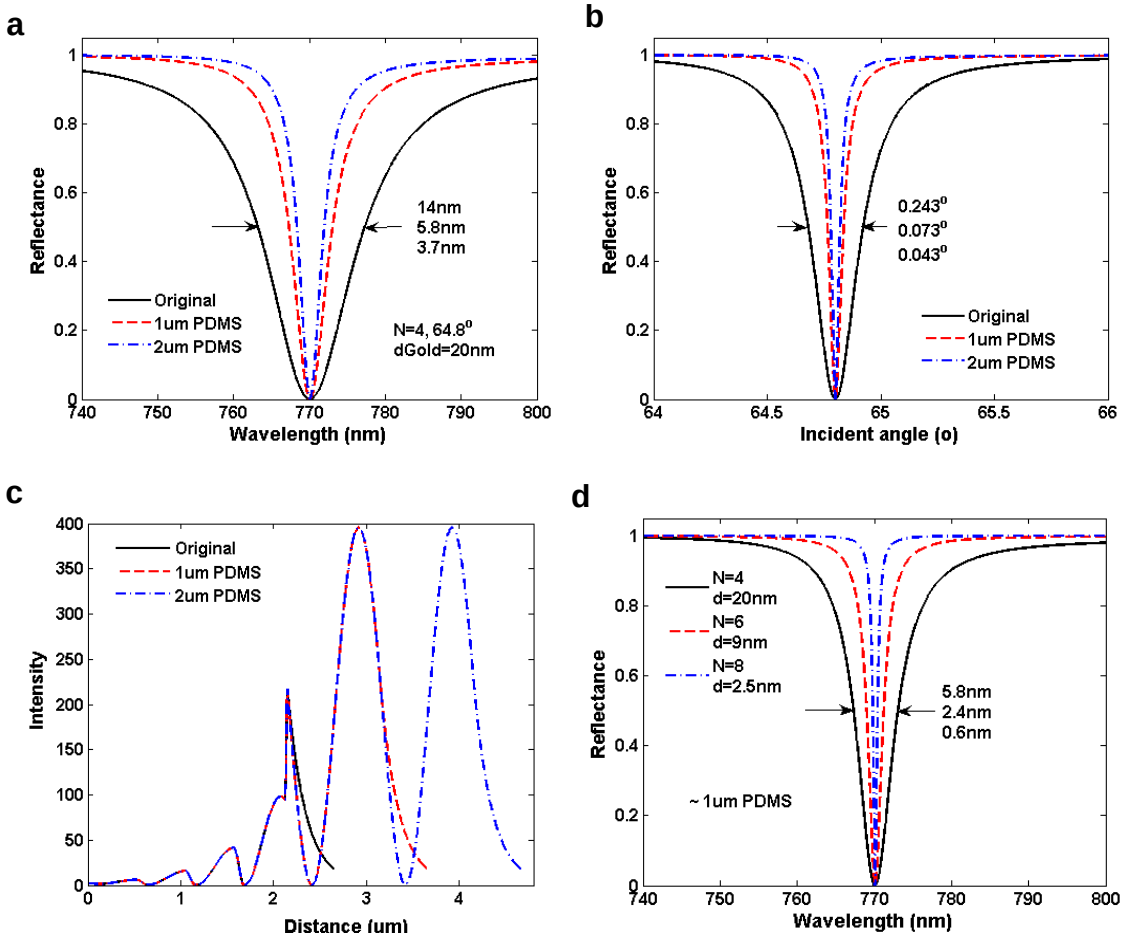

Figure 6.17 (a) and (b) Reflectance spectrum of the PC-Metallic structure with different thicknesses of PDMS layer; (c) field intensity distribution of the structure for different thicknesses of PDMS layer; (d) resonance dip width with different number of multiple dielectric layers.

In addition, one of the biggest advantages of our all-optical ultrasound transducer is that it operates in total-internal-reflection geometry. On one side, we can always use a high power pulse laser to generate strong acoustic waves without damaging the objects; on the other side, open cavity configuration allows us to choose low Young's modulus polymer material to get high sensitivity without decreasing the cavity finesse as etalon sensors do.

What is more, the unique PC-metallic structure allows us to operate the ultrasound transducer at any wavelength, giving much more flexibility to choose pulse laser and CW laser sources, which is very helpful for applications and commercialization. Furthermore, the PC-metallic structure can be fabricated easily with low cost.

In all, the ultrasound transmitter and the receiver using the PC-metallic structure exhibit better performance than the state-of-the-art optoacoustic transmitter and receiver, respectively. Thus integrated, the all-optical ultrasound transducer based on the structure possesses all the advantages and has great potential to provide a broad-band (> 200MHz), highly sensitive acoustic system for biomedical and industrial applications.

6.3.5 Biosensor based on the PC-metallic structure

The photonic crystal-metallic structure introduces a novel plasmon excitation mechanism, and it also can be used to construct optical biosensors, similar to conventional surface-plasmon-resonance (SPR) sensors. The unique configuration provides many advantages compared to SPR sensors, such as a narrower resonance dip, more controllable operative wavelength and angle, longer propagation length, etc. In addition, with a narrower resonance mode, we can achieve higher detection sensitivity with intensity modulation instead of angular (or wavelength) modulation, which is the most common approach used in high-performance commercial SPR-based system Biacore Instruments. In the following, we will discuss the properties of a biosensor based on the PC-metallic structure in detail.

We performed a series of simulations and compared the PC-metallic sensor with classical SPR sensors. In order to achieve a pronounced dip around the operative

wavelength 632.8 nm and the incident angle around 64° in the substrate, the PC-metallic structure were designed as: substrate (BK7 glass) / TiO_2 / $(SiO_2/TiO_2)^5$/ X (SiO_2) / Au (as Figure 4 shows), and their thicknesses were determined to be 90 nm, 340 nm, 340 nm, and 9 nm for the TiO_2, SiO_2, X and Au layers respectively, using a transfer matrix calculation. For comparison, the classical SPR sensor is composed of 48-nm gold film on a BK7 glass substrate. Figure 6.18 shows the simulated reflectance spectra for these two sensors. It is easily found that the PC-metallic sensor can get at least an order of magnitude narrower resonance dip width ($\Delta\lambda$ or $\Delta\theta$) than the SPR sensor (refer to Table 6.2). However, its bulk solvent index sensitivity (S) is just a little bit lower than the SPR sensor.

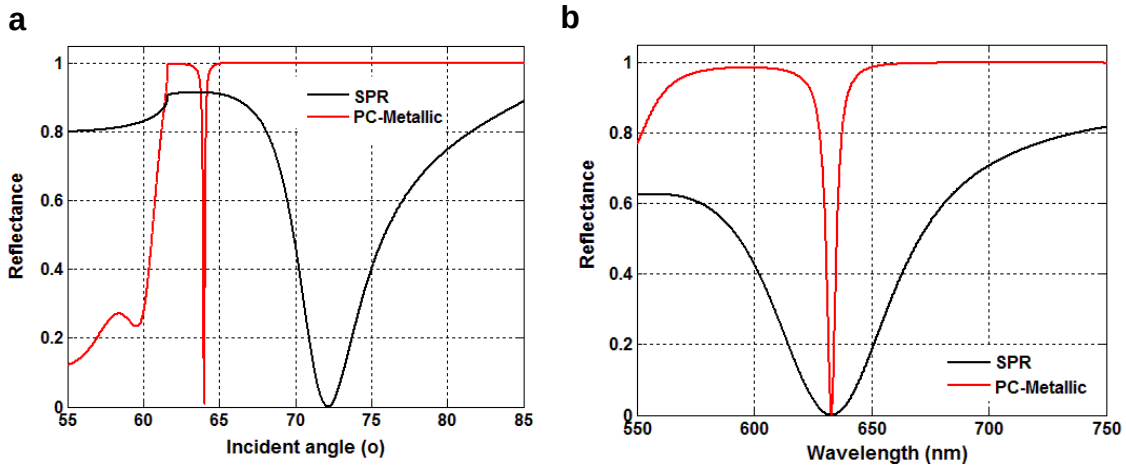

Figure 6.18 Simulated reflectance spectra of the SPR sensor and the PC-metallic sensor (a) angle; (b) wavelength.

In order to compare the PC-metallic sensor and the SPR sensor, I calculated their figure of merit (FOM) according to Equation 4.6. As listed in Table 6.3, the FOM value of the PC-metallic sensor is ~10 times larger than that of SPR sensors. Moreover, for the same operative wavelength 632.8 nm, the incident angle is 64.04° for the PC-metallic sensor, smaller than that of the SPR sensor (72.14°), which makes it easier to operate in experiments. In addition, I compared the plasmon propagation length L_{SP} along the metal sensing surface. I have shown that the propagation length for the PC-metallic sensor is over 30 times longer than the SPR sensor, which will greatly increase the detection area.

Sensors	Resonance width	Bulk sensitivity	FOM	Propagation length
SPR	$\Delta\lambda \sim 60$ nm	1900 nm/ RIU	31.7	2.3 μm
	$\Delta\theta \sim 5.5^{o}$	145 ^{o}/RIU	26.4	
PC-metallic	$\Delta\lambda \sim 4.7$ nm	1400 nm/RIU	297.9	72.5 μm
	$\Delta\theta \sim 0.12^{o}$	36 ^{o}/RIU	300	

Table 6.3 Comparison of the PC-metallic sensor and the SPR sensor.

For SPR sensors, the adjustment of the operative wavelength, incident angle, and resonance dip width is difficult due to the limited variable parameters (mainly the thickness of the metal layer). In sharp comparison, the PC-metallic sensor can fully take advantage of the properties of the photonic crystal structure and has several variable parameters (the number of dielectric layers, the defect layer thickness, the metal layer thickness) to adjust to get the pronounced resonance dip in the reflectance spectrum. For example, we can easily narrow down the resonance dip width by increasing the number of PC layers and decreasing the metal layer thickness. What is more, we can add one more dielectric layer (e.g., 633-nm SiO_2 layer in Figure 6.19) on top of the metal layer, since the structure can form another Fabry-Pérot resonant microcavity. It provides several advantages: 1) it gets a narrower resonance mode, which is impossible for SPR sensors; 2) it still gets large field intensity on the sensing surface; and 3) it can protect the metal layer and use common surface chemistry (on glass slides) for biomedical applications.

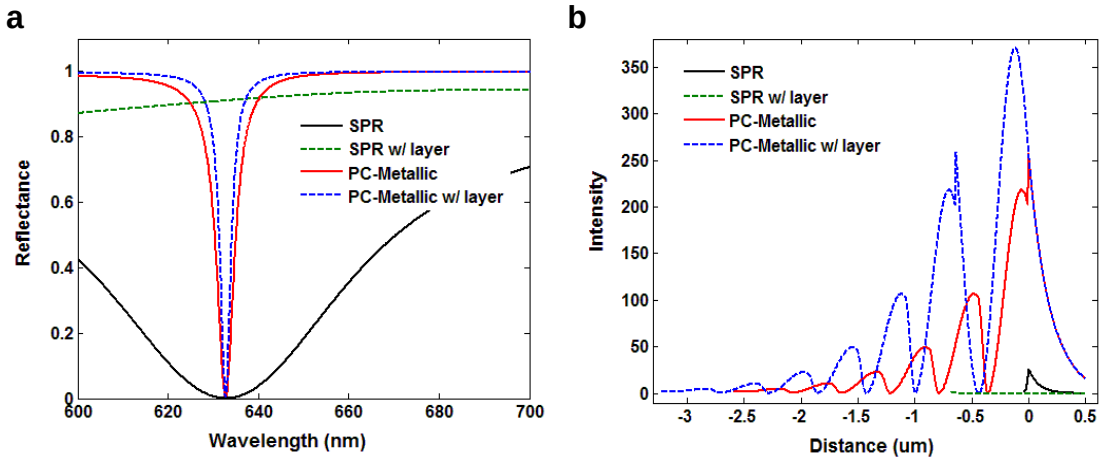

Figure 6.19 Effects of one more SiO_2 layer on top of the SPR sensor and the PC-metallic sensor: (a) resonance dip; (b) field enhancement on the sensing surface.

In conclusion, using the PC-metallic structure as an optical biosensor could provide many distinct advantages compared to the state-of-the-art commercial SPR-based system. It greatly improves the detection sensitivity with a simple structure and configuration and could find many applications in biomolecular detections.

6.3.6 Enhanced total-internal-reflection fluorescence microscopy (TIRFM)

The PC-metallic structure not only leads to enhanced absorbance and reflectance of light of a specific wavelength, which can be used to develop the ultrasound transducer and biosensor shown above, but also can obtain large intensity enhancement for light of a specific wavelength. Moreover, the metallic structure itself has unique properties compared to dielectric materials and has been widely used in many areas (e.g., fluorescence measurements, Raman spectroscopy). The PC-metallic structure provides a powerful and unique substrate (instead of glass or a purely metallic surface) for many applications that need a metallic structure. In the following, I will discuss its application in total-internal-reflection fluorescence microscopy (TIRFM).

6.3.6.1 Introduction

TIRFM is a powerful technique [125]. It can excite and visualize fluorophores present in extremely thin axial sectioning (such as the near-membrane region of live or fixed cells grown on coverslips), which allows wide-field imaging with very low background and minimal out-of-focus fluorescence. The unique features of TIRFM make it invaluable in biological studies, such as single molecule detection, single particle tracking, and the observation of dynamic membrane events on live cell surfaces (signaling, endocytosis, and exocytosis).

The principle behind TIRFM is the phenomenon of total internal reflection. The reflected light will generate an electromagnetic field that penetrates only a very short distance (~100 nm beyond the interface as an evanescent wave into the surrounding medium). It can be used to excite fluorescence in objects within the evanescent field. Unwanted background and out-of-focus fluorescence signals are dramatically reduced with TIRFM, thus improving the sensitivity of the system and the ability to view very dim fluorescence events.

The sensitivity of TIRFM is directly related to the excitation intensity, which is maximal at the interface and decreases exponentially with increasing distance from the interface. However, the intensity enhancement for the excitation light within the evanescent field (using pure glass as the substrate) is small, which disfavors fluorescence emission.

If we can increase the excitation light intensity by field enhancement in the evanescent region, then the fluorescence emission in TIRFM will be enhanced. Ye et al. used a 1-D PC structure with fluorescent dye molecules as the defect layer in TIR geometry and observed an over ~20-fold enhanced fluorescence emission signal [57]. Soboleva et al. took advantage of the field enhancement due to surface electromagnetic waves on a 1-D PC structure in TIR and also got very high fluorescence emission [126]. Although these PC structures both reached a large fluorescence emission signal, the background noise was also increased. Moreover, their propagation lengths along the surface were long (~ 200 μm) [126], which increases the detection area and decreases the signal-to-noise ratio. Surface plasmon (SP) enhanced TIRFM was also developed where the cover glass was coated on one side with a nanometer metallic film (such as silver) [127]. The fluorescence signal was increased by 5~6-fold by SP enhancement; at the same time, the background noise was dramatically reduced because of the unique properties of the metallic film: the collection efficiency varies with the fluorophore-metal distance. It made the SP-enhanced TIRFM only sensitive to the intermediate distance (10-50 nm) that the basal membrane cell was estimated to lie within. However, it also had some drawbacks; for example, it had to use a large incident angle (and thus a high N.A. objective lens) to excite surface plasmons, especially for shorter wavelengths.

6.3.6.2 PC-metallic structure for prism-type TIRFM

Compared to the glass-based, PC-based, and SP-based TIRFM summarized above, the PC-metallic structure combines the properties of a photonic crystal structure with that of a metallic structure and provides many unique advantages in TIRFM. The configuration is the same as conventional TIRFM, except for using a cover glass coated with our PC-metallic structure on one side, as Figure 6.20 (a) shows.

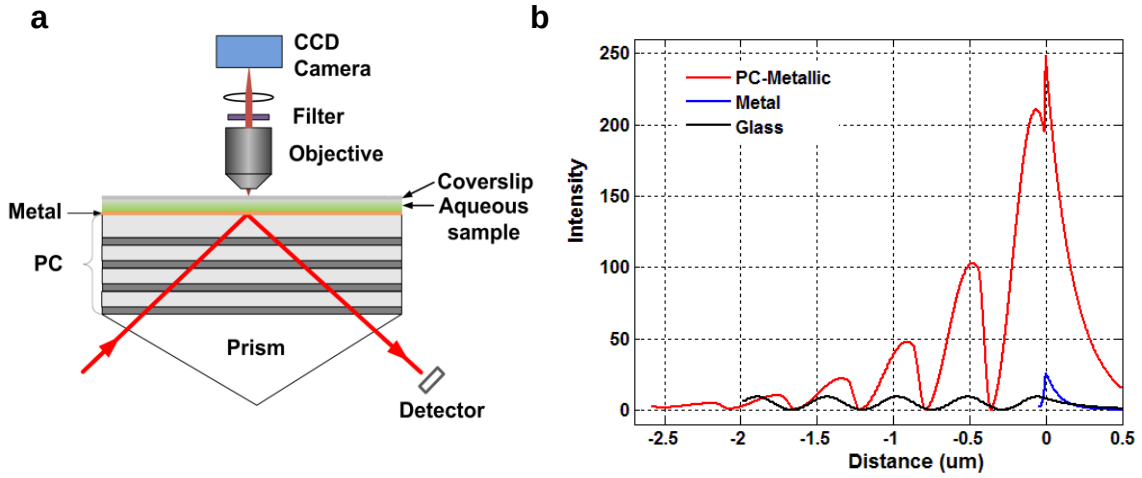

Figure 6.20 (a) Schematic structure of using the PC-metallic structure in prism-based TIRFM; (b) simulations of intensity enhancement in PC-metallic, pure metal ,and glass structures.

First, the PC-metallic structure can greatly improve the fluorescence signal. As Figure 6.20(b) shows, it is predicted to reach a ~10-fold intensity enhancement over the pure metal structure, and a 40- to 50-fold enhancement over glass.

Second, the PC-metallic structure can also dramatically reduce the background noise, similar to the SP-TIRFM. The presence of the metallic structure acts as a strong distance-dependent filter, effectively selecting fluorophores at the correct distance for live membrane observation: at very short distances (<10 nm), the fluorescence is quenched, which reduces noise from fluorescent molecules adhering to the cover glass surface; at larger distances (>150 nm), most of the emitted fluorescence (>90%) is reflected by the metal and the detection efficiency is low, which is useful in reducing background fluorescent noise from the inner part of the cell; only at intermediate distances (10-50 nm) is the detection efficiency high, which is ideal for detecting fluorescence in the membranes of cells.

Third, the PC-metallic structure is only sensitive to *p*-polarization, which enables better suppression of background noise than conventional TIRFM that is sensitive to both *s*- and *p*-polarization. The fluorescence's coupling to surface plasmons depends dramatically on the orientation of the molecule transition moment: Coupling is very efficient for an orthogonal dipole orientation (*p*-polarization); conversely, coupling is

much weaker for a dipole orientation in the plane of a metal surface (*s*-polarization). This feature makes our PC-metallic structure useful for measurements of orientation changes.

Fourth, the PC-metallic structure can be designed to operate at different incident angles. According to Equation 11, for the same incident light wavelength, it has the same penetration depth as conventional TIRFM does. However, for an SP-based TIRFM, the angle needed for surface plasmon excitation increases with decreasing light wavelengths, which is a limiting factor for short wavelength excitation [127]. In contrast, for PC-metallic-based TIRFM, we can design the PC structure to make it work at a smaller incident angle. For example, as Figure 6.18(a) shows, the wavelength of the incident light is 632.8 nm, and the incident angle needed to reach the highest intensity enhancement (that is, the resonance angle) for a PC-metallic structure is 64.04^{o}, while the resonance angle is 72.14^{o} for an SPR structure. So the PC-metallic structure is more convenient to use in TIRFM.

Fifth, the PC-metallic structure can accurately control the resonance angle for incidence and the penetration length. The detection of TIRFM is largely dependent on the penetration length, which is often unknown. In conventional TIRFM, the incident angle is difficult to control well enough to achieve a desired penetration length because of variable experimental conditions. However, for our PC-metallic structure, we can determine the correct incident angle and then the penetration length. As Figure 6.20(a) shows, we can use a detector to monitor the reflected intensity. When the incident angle is the resonance angle of the PC-metallic structure, the reflected intensity reaches a minimum. Since the structure can have a very small resonance width, the incident angle can be accurately prescribed, and so can the penetration length.

In summary, the PC-metallic structure can enhance the fluorescence signal by more than one order of magnitude above that of conventional TIRFM and can reduce the background noise dramatically, which improves the detection sensitivity and resolution of TIRFM. In addition, the PC-metallic structure can be operated at smaller incident angles and the penetration length can be accurately determined. These features make the PC-metallic structure proposed here useful for TIRFM applications.

6.3.6.3 PC-metallic nanostructure for TIRFM

The performance of PC-metallic structure-based TIRFM can be further improved by nanostructuring the metal layer. Although our PC-metallic structure leads to a shorter propagation length along the metal surface (10~80 μm) than that of a PC-based structure (~200 μm), it may still increase the detected area in TIRFM to a certain degree. Using a metallic (e.g., gold) nanostructure, which can be made less than 50 nm deep [128], the plasmon modes can be localized in a very small area, further reducing the detection volume to reach a high signal-to-noise (SNR) ratio. Zero-mode waveguides consisting of subwavelength holes in a metal film on a glass substrate have been developed and commercialized to study single-molecule (DNA) dynamics [129]. Etching the glass substrate with a certain thickness will further improve the detection SNR so that it could be used to directly study protein-protein interactions at a low intracellular concentration in real time [130].

Here I propose a novel structure as depicted in Figure 6.21(a). The defect and metal layers are nanostructured so that several parameters can be designed to optimize performance. Besides the advantages provided by a zero-mode waveguide, such as a reduction in detection volume and an increase in signal-to-noise, our PC-metallic nanostructure will further improve the signal-to-noise ratio. The structure is designed to reach high on-resonance intensity with the gold layer and off-resonance for the region without gold at a certain angle. As Figure 6.21(b) shows, the intensity enhancement with light injecting on the gold region is predicted to be much higher (~ 200-fold) than that on the region without gold.

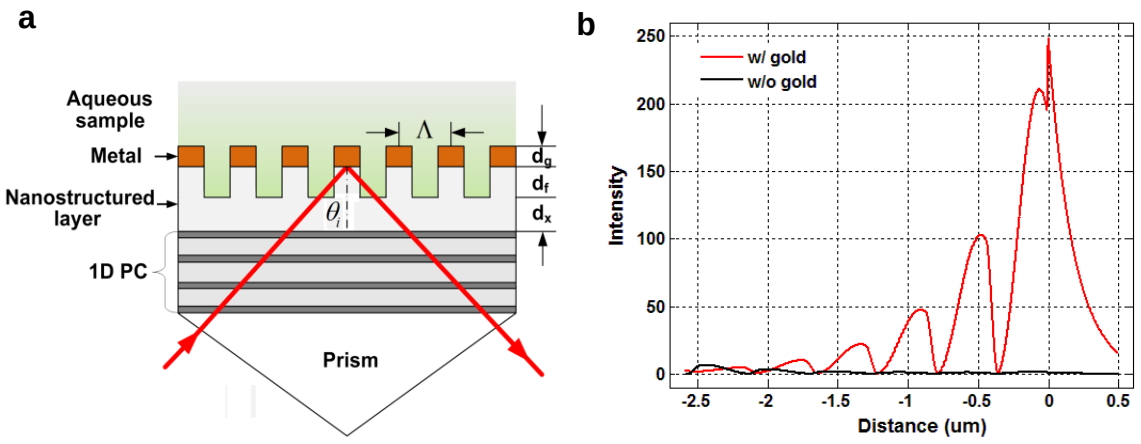

Figure 6.21 (a) Combination of PC and metallic nanostructure in TIRFM; (b) simulations of intensity enhancement of the PC-metallic nanostructure for regions with gold or without gold.

6.3.6.4 PC-metallic structure for object-type TIRFM

Besides prism-type TIRFM shown in Figure 6.20(b), the PC-metallic structure can be also used in objective-type TIRFM as Figure 6.22(a) shows. The input laser light is focused into the objective lens, and the intensity is enhanced by the PC-metallic structure at a resonance angle, which is used to excite a large fluorescence signal. The emitted fluorescence signal is collected back through the objective lens. Figure 6.22(b) shows the angular spectrum of the transmission of a single wavelength light, when the emission fluorescence light goes through either a glass, metal or PC-metallic structure.

Although the PC-metallic structure has lower transmission for certain angles compared to pure glass, it can enhance the light intensity for fluorescence excitation, which will increase the transmitted fluorescence signal. Moreover, a PC-metallic structure has a larger transmission over the angle range than pure metal (such as a 40-nm thick silver film), which has been demonstrated to afford 5- to ~6-fold enhancement of a fluorescence signal when compared to pure glass, thus achieving improved TIRF imaging [127]. Therefore, PC-metallic structure based objective-type TIRFM shows promise as a potential power technique for highly sensitive, real-time cell imaging.

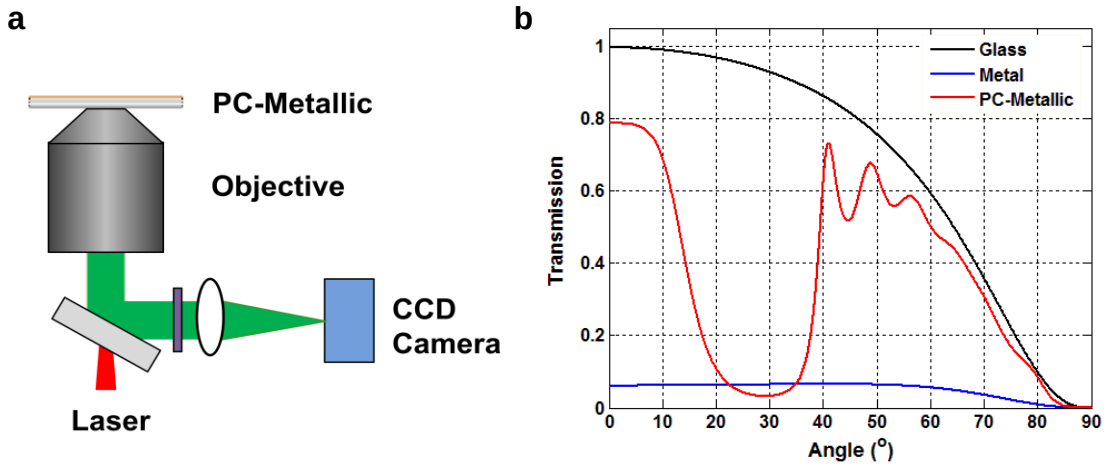

Figure 6.22 (a) PC-metallic structure used in objective-type TIRFM; (b) simulated transmission curves versus incident angles for objective-type TIRFM with different substrates (glass, metal, and PC-metallic).

In summary, the PC-metallic structure could be used in both prism-type and objective-type TIRFM and shows great potential to comprehensively improve the performance of TIRF imaging, including an enhanced fluorescence signal and low background noise. Moreover, for prism-type TIRFM, it can be easily integrated with the biosensing measurements to provide more information about biomolecular interactions.

6.3.7 Conclusion

In this section, I proposed and developed a novel plasmon excitation mechanism using a photonic crystal structure and a metallic structure in a total-internal-reflection geometry. This unique configuration, possessing the advantages of photonic crystal and metallic structures, has been explored to develop novel broad-band, all-optical ultrasound transducers for high-resolution ultrasound imaging, a highly sensitive biomolecular sensor, and enhanced total-internal-reflection fluorescence microscopy. Moreover, multiple capabilities also make the PC-metallic structure useful in developing integrated systems, such as a combination of biosensing and TIRF measurement or biosensing and SERS, that will provide more information for biomolecular interactions. In addition, the PC-metallic structure can be integrated on optical fibers or waveguides, which provides other advantages and allows broader applications.

With its great potential for commercialization, this part of work has been submitted for U.S. Patent Application:

Guo, Y., Norris, T. B., Baker, J. R., Guo, L. J., and Walter, N. G. Photonic crystal-metallic structures and applications. University of Michigan, Invention report #4669 (2010).

Bibliography

1. *The worldwide market for in vitro diagnostic tests* (Kalorama Information, 2006).
2. Wells, J. A. & McClendon, C. L. Reaching for high-hanging fruit in drug discovery at protein-protein interfaces. *Nature* **450**, 1001-1009 (2007).
3. Arkin, M. R. & Wells, J. A. Small-molecule inhibitors of protein-protein interactions: progressing towards the dream. *Nat. Rev. Drug Discov.* **3**, 301-317 (2004).
4. Cooper, M. A. Optical biosensors in drug discovery. *Nat. Rev. Drug Discov.* **1**, 515-528 (2002).
5. Narayanaswamy, R. & Wolfbeis, Otto S. (eds) *Optical Sensors: Industrial, Environmental and Diagnostic Applications* (Springer, 2004).
6. Rich, R. L. & Myszka, D. G. Survey of the year 2007 commercial optical biosensor literature. *J. Mol. Recognit.* **21**, 355-400 (2008).
7. Lakowicz, J. R. *Principles of Fluorescence Spectroscopy* (Springer, 2006).
8. Moerner, W. E. New directions in single-molecule imaging and analysis. *Proc. Natl. Acad. Sci.* **104**, 12596- 12602 (2007).
9. Elf, J., Li, G.W. & Xie, X. S. Probing transcription factor dynamics at the single-molecule level in a living cell. *Science* **316**, 1191-1194 (2007).
10. Cox, W.G., & Singer, V. L. Fluorescent DNA hybridization probe preparation using amine modification and reactive dye coupling. *Biotechniques* **36**,114-122 (2004).
11. Fan, X. et al. Sensitive optical biosensors for unlabeled targets: A review. *Anal. Chim. Acta.* **620**, 8-26 (2008).
12. Rasooly, A. & Herold, K. E. (eds) *Biosensors and Biodetection: Methods and Protocols Volume 1: Optical-Based Detectors (Methods in Molecular Biology)* (Humana Press, 2008).
13. Cooper, M. A. (eds) *Label-Free Biosensors: Techniques and Applications* (Cambridge University Press, 2009).
14. Lechuga, L. M. Optical sensors based on evanescent field sensing - Part II. Integrated optical sensors. *Quim. Anal.* **19**, Suppl. 1, 61-67 (2000).
15. White, I. M. & Fan, X. On the performance quantification of resonant refractive index sensors. *Opt. Express* **16**, 1020-1028 (2008).
16. Kabashin, A.V., *et al.* Plasmonic nanorod metamaterials for biosensing. *Nat. Mater.* **8**, 867-871 (2009).
17. Homola, J. Present and future of surface plasmon resonance biosensors. *Anal. Bioanal. Chem.* **377**, 528-539 (2003).
18. Homola, J. Surface plasmon resonance sensors for detection of chemical and biological species. *Chem. Rev.* **108**, 462-493 (2008).

19. Hoaa, X. D., Kirk, A.G. and Tabrizian, M. Towards integrated and sensitive surface plasmon resonance biosensors: A review of recent progress. *Biosens. Bioelectron.* **23**, 151-160 (2007).

20. Myszka, D. G. Analysis of small-molecule interactions using Biacore S51 technology. *Anal. Biochem.* **329**, 316-323 (2004).

21. Vollmer, F. et al. Protein Detection by Optical shift of a Resonant Microcavity. *Appl. Phys. Lett.* **80**, 4057-4059 (2002).

22. Vollmer, F. & Arnold, S. Whispering-gallery-mode biosensing: label-free detection down to single molecules. *Nat. Methods* **5**, 591-596 (2008).

23. Armani, A.M., Kulkarni, R.P., Fraser, S.E., Flagan, R.C. & Vahala, K.J. Label-free, single-molecule detection with optical microcavities. *Science* **317**, 783-787 (2007).

24. White, I. M. et al. Integrated multiplexed biosensors based on liquid core optical ring resonators and antiresonant reflecting optical waveguides. *Appl. Phys. Lett.* **89**, 191106 (2006).

25. Ilchenko, V. S. & Gorodetskii, M. L. Thermal nonlinear effects in optical whispering gallery microresonators. *Laser Phys.* **2**, 1004-1009 (1992).

26. Weiss, S.M., Rong, G., and Lawrie, J. L. Current status and outlook for silicon-based optical biosensors. *Physica E* **41**, 1071-1075 (2009).

27. Jane, A., Dronov, R., Hodges, A., and Voelcker, N. H. Porous silicon biosensors on the advance. *Trends Biotechnol.* **27**, 230-239 (2009).

28. Orosco, M. M., Pacholski, C., and Sailor, M. J. Real-time monitoring of enzyme activity in a mesoporous silicon double layer. *Nat. Biotechnol.* **4**, 255-258 (2009).

29. Lin, V. S.Y., Motesharei, K., Dancil, K.P.S., Sailor, M.J. & Ghadiri, M.R. A porous silicon-based optical interferometric biosensor. *Science* **278**, 840-843 (1997).

30. Ouyang, H. et al. Macroporous silicon microcavities for macromolecule detection. *Adv. Funct. Mater.* **15**, 1851-1859 (2005).

31. Ouyang, H., Striemer, C. C., and Fauchet, P. M. Quantitative analysis of the sensitivity of porous silicon optical biosensors. *Appl. Phys. Lett.* **88**, 163108 (2006).

32. Silicon Kinetics. http://www.siliconkinetics.com/pages/technology.html

33. Lee, M. R. and Fauchet, P. M. Two-dimensional silicon photonic crystal based biosensing platform for protein detection. *Opt. Express* **15**, 4530-4535 (2007).

34. Zlatanovic, S. et al. Photonic crystal microcavity sensor for ultracompact monitoring of reaction kinetics and protein concentration. *Sens. Actuators B: Chem.* **141**, 13-19 (2009).

35. Kang, C. & Weiss, S. M. Photonic crystal with multiple-hole defect for sensor applications. *Opt. Express* **16**, 18188-18193 (2008).

36. Wu, D. K. C., Kuhlmey, B. T. and Eggleton, B. J. Ultrasensitive photonic crystal fiber refractive index sensor. *Opt. Lett.* **34**, 322-324 (2009).

37. Mandal, S. and Erickson, D. Nanoscale optofluidic sensor arrays. *Opt. Express* **16**, 1623-1631 (2008).

38. Konopsky, V. N. and Alieva, E. V. Photonic crystal surface waves for optical biosensors. *Anal. Chem.* **79**, 4729-4735 (2007).

39. Lin B. et al. A label-free optical technique for detecting small molecule interactions. *Biosens. Bioelectron.* **17**, 827-834 (2002).

40. Guo, Y. et al. Sensitive bioassay using a photonic crystal structure in total internal reflection. *Opt. Express* **16**, 11741-11749 (2008).

41. Guo, Y. et al. Label-free biosensing using a photonic crystal structure in a total-internal-reflection geometry. *Proc. SPIE* **7188**, 71880B (2009).

42. Guo, Y. et al. Real-time biomolecular binding detection using a sensitive photonic crystal biosensor. accepted by *Anal. Chem.* (2010).

43. Fink, Y. et al. A dielectric omnidirectional reflector. *Science* **282**, 1679-1682 (1998).

44. Tocci, M.D. et al. Thin-Film Nonlinear Optical Diode. *Appl. Phys. Lett.* **66**, 2324-2326 (1995).

45. Radic, S., George, N., and Agrawal, G. P. Theory of low-threshold optical switching in nonlinear, phase-shifted, periodic structures, *J. Opt. Soc. Am. B* **12**, 671-680 (1995).

46. Hsueh, W.J. & Lin, J. C. Numerical stable method for the analysis of Bloch waves in a general one-dimensional photonic crystal cavity. *J. Opt. Soc. Am. B* **24**, 2249-2258 (2007).

47. Yeh, P. *Optical Waves in Layered Media* (John Wiley & Sons, 2005).

48. Knittl, Z. *Optics of Thin films (An Optical Multilayer Theory)* (Wiley, 1976).

49. Muriel, M. A., Carballar, A., Azaña, J. Field distributions inside fiber gratings. *J. IEEE J. Quantum Electron.* **35**, 548-558 (1999).

50. Li, Z.Y. & Lin, L.L. Photonic band structures solved by a plane-wave-based transfer-matrix method. *Phys. Rev. E* **67**, 046607 (2003).

51. Mishra, S. & Satpathy, S. One-dimensional photonic crystal: The Kronig-Penney model. *Phys. Rev. B.* **68**, 045121(2003).

52. Srivastava, S. K. & Ojha, S. P. Omnidirectional reflection bands in one-dimensional photonic crystal structure using fluorescence films. *Progress In Electromagnetics Research, PIER* **74**, 181-194 (2007).

53. Bergstein, D.A. et al. Resonant cavity imaging: a means toward high-throughput label-free protein detection. *IEEE J. Sel. Top. Quantum Electron.***14**, 131-139 (2008).

54. Ye, J. Y. et al. Enhancement of two-photon excited fluorescence using one-dimensional photonic crystals. *Appl. Phys. Lett.* **75**, 3605 (1999).

55. Hattori, T. Third-order nonlinearity enhancement in one-dimensional photonic crystal structures. *Jpn. J. Appl. Phys.* **41**, 1349-1353(2002).

56. Ye, J.Y. & Ishikawa, M. Light enhancement method and device and their applications in fluorescence detection. Japan Patent JP 2001-242083 (2001).

57. Ye, J. Y. & Ishikawa, M. Enhancing fluorescence detection with a photonic crystal structure in a total-internal-reflection configuration. *Opt. Lett.* **33**, 1729-1731 (2008).

58. Inouye, H., Arakawa, M., Ye, J. Y., Hattori, T., Nakatsuka, H., and Hirao, K. Optical properties of a total-reflection-type one-dimensional photonic crystal. *IEEE J. Quant. Electr.* **38**, 867-871(2002).

59. Inouye, H. & Kanemitsu, Y. Direct observation of nonlinear effects in a one-dimensional photonic crystal. *Appl. Phys. Lett.* **82**, 1155-1157 (2003).

60. Nelson, R. L. & Haus, J. W. One-dimensional photonic crystals in reflection geometry for optical applications. *Appl. Phys. Lett.* **83**, 1089-1091 (2003).

61. Chow, C. M., Zhou, Y., Guo, Y., Norris, T. B., Wang, X., Deng, C. X. and Ye, J. Y. High-frequency ultrasonic sensor using an open-cavity photonic crystal structure. Submitted to *J. Biomed. Opt.* (2010).

62. Ye, J. Y., Guo, Y., Norris, T. B. and Baker, J. R. Photonic Crystal Sensor. US Patent 7,639,362 (2009).

63. Jung, L. S. et al. Quantitative interpretation of the response of surface plasmon resonance sensors to adsorbed films. *Langmuir* **14**, 5636-5648 (1998).

64. Kaiser, R. et al. Resonant enhancement of evanescent waves with a thin dielectric waveguide. *Opt. Commun.* **104**, 234-240 (1994).

65. Villa, F. et al. Photonic crystal sensor based on surface waves for thin-film characterization. *Opt. Lett.* **27**, 646-648 (2002).

66. Robertson, W. M. & May, M. S. Surface electromagnetic wave excitation on one-dimensional photonic band-gap arrays. *Appl. Phys. Lett.* **74**, 1800-1802 (1999).

67. Shin, M. & Robertson, W. M. Surface plasmon-like sensor based on surface electromagnetic waves in a photonic band-gap material. *Sens. Actuators B* **105**, 360-364 (2005).

68. Usievich, B. A. et al. Surface waves at the boundary of a system of coupled waveguides. *Quant. Electr.* **37**, 981-984 (2007).

69. Piliarik, M. & Homola, J. Surface plasmon resonance (SPR) sensors: approaching their limits? *Opt. Express* **17**, 16505-16517 (2009).

70. Schmidt, O., Kiesel, P., Mohta, S. and Johnson, N. M. Resolving pm wavelength shifts in optical sensing. *Appl. Phys. B* **86**, 593-600 (2007).

71. Ran, B. & Lipson, S. G. Comparison between sensitivities of phase and intensity detection in surface plasmon resonance. *Opt. Express* **14**, 5641-5650 (2006).

72. Liu, X., Cao, Z., Shen, Q. and Huang, S. Optical Sensor Based on Fabry-Perot Resonance Modes. *Appl. Opt.* **42**, 7137-7140 (2003).

73. Shurnaker-Parry, J. S. & Campbell, C. T. Quantitative methods for spatially resolved adsorption/desorption measurements in real time by surface plasmon resonance microscopy. *Anal. Chem.* **76**, 907-917 (2004).

74. Myszka, D. G. Improving biosensor analysis. *J. Mol. Recognit.* **12**, 279-284 (1999).

75. Kolomenski, A. et al. Propagation length of surface plasmons in a metal film with roughness. *Appl. Opt.* **48**, 5683-5691 (2009).

76. Seshan, K. (eds) *Handbook of Thin Film Deposition Processes and Techniques (Materials and Processing Technology)* (Noyes Publications, 2002).

77. CVI Melles Griot. *Dispersion Equations*. www.cvimellesgriot.com

78. Rao, K. N. Influence of deposition parameters on optical properties of TiO_2 films. *Opt. Eng.* **41**, 2357-2364 (2002).

79. Virginia Semiconductor, Inc. *Optical Properties of Silicon*. www.vriginiasemi.com

80. Tamir, T. & Bertont, H. L. Lateral displacement of optical beams at multilayered and periodic structures, *J. Opt. Soc. Am.* **61**, 1397-1413 (1971).

81. Suter, J. D., White, I. M., Zhu, H., and Fan, X. Thermal characterization of liquid core optical ring resonator sensors. *Appl. Opt.* **46**, 389-396 (2007).

82. Jung, L. S., Nelson, K. E., Stayton, P. S. and Campbell, C. T. Binding and dissociation kinetics of wild-type and mutant streptavidins on mixed biotin-containing alkylthiolate monolayers. *Langmuir* **16**, 9421-9432 (2000).

83. Anker, J. N. et al. Biosensing with plasmonic nanosensors. *Nat. Mater.* **7**, 442-453 (2008).

84. Stewart, C. E., Hooper, I. R. and Sambles, J. R. Surface plasmon differential ellipsometry of aqueous solutions for bio-chemical. *J. Phys. D: Appl. Phys.* **41**,105408 (2008).

85. Wang, W.U., Chen, C., Lin, K.H., Fang, Y. & Lieber, C.M. Label-free detection of small-molecule-protein interactions by using nanowire nanosensors. *Proc. Natl. Acad. Sci. USA* **102**, 3208-3212 (2005).

86. Weber, P. C. et al. Structural origins of high-affinity biotin binding to streptavidin. *Science* **243**, 85-88 (1989).

87. *Biacore 3000 getting started*, Biacore, Sweden (2003).

88. Bhushan, B. et al. Morphology and adhesion of biomolecules on silicon based surfaces, *Acta Biomaterialia* **1**,327-341(2005).

89. Schiestel, T., Brunner, H. & Trovar, G.E.M. Controlled surface functionalization of silica nanospheres by covalent conjugation reactions and preparation of high density streptavidin nanoparticles. *J. Nanosci. Nanotech.* **4**, 504-511 (2004).

90. Choi, S. Y., Lee, J. W., and Sim, S. J. Enhancement of the sensitivity of surface plasmon resonance (SPR) immunosensor for the detection of anti-GAD antibody by

changing the pH for streptavidin immobilization. *Enzyme Microb. Technol.* **35**, 683-687 (2004).

91. Fortina, P., Surrey, S., Kricka, L.J., Molecular diagnostics: hurdles for clinical implementation.*Trends Mol. Med.* **8**, 264-266 (2002).

92. Charles, P.T. et al. Fabrication and surface characterization of DNA microarrays using amine- and thiol-terminated oligonucleotide probes. *Langmuir* **19**, 1586-1591. (2003).

93. Nelson, B.P., Grimsrud, T.E., Liles, M.R., Goodman, R.M. & Corn, R.M. Surface plasmon resonance imaging measurements of DNA and RNA hybridization adsorption onto DNA microarrays. *Anal. Chem.* **73**, 1-7 (2001).

94. Suter, J. D., White, I. M., Zhu, H., Shi, H., Caldwell, C.W., Fan, X. Label-free quantitative DNA detection using the liquid core optical ring resonator. *Biosens. Bioelectron.* **23**, 1003-1009 (2008).

95. Yang, N., Su, X., Tjong, V. & Knoll, W. Evaluation of two- and three-dimensional streptavidin binding platforms for surface plasmon resonance spectroscopy studies of DNA hybridization and protein–DNA binding. *Biosens. Bioelectron.* **22**, 2700-2706 (2007).

96. http://www.thermo.com/eThermo/CMA/PDFs/Articles/articlesFile_2449.pdf

97. Swann, M.J., Peel, L.L., Carrington, S. & Freeman, N. J. Dual-polarization interferometry: an analytical technique to measure changes in protein structure in real time, to determine the stoichiometry of binding events, and to differentiate between specific and nonspecific interactions. *Anal. Biochem.* **329**, 190-198 (2004).

98. Cottier, K., Wiki, M., Voirin, G., Gao, H. & Kunz, R.E. Label-free highly sensitive detection of (small) molecules by wavelength interrogation of integrated optical chips. *Sens. Actuators B: Chem.* **91**, 241-251 (2003).

99. Chao, C., Fung, W. & Guo, L.J. Polymer microring resonators for biochemical sensing applications. *IEEE J. Sel. Top. Quantum Electron.* **12**, 134-142 (2006).

100. Lin, B. *et al.* A label-free optical technique for detecting small molecule interactions. *Biosens. Bioelectron.* **17**, 827-834 (2002).

101. Comley, J. et al. LABEL-FREE DETECTION New biosensors facilitate broader range of drug discovery applications. *Drug Discovery World Winter*, 63-74 (2004/5)

102. Zhu, H., White, I.M., Suter, J.D., Dale, P.S. and Fan, X. Analysis of biomolecule detection with optofluidic ring resonator sensors. Opt. Express 15, 9139-9146 (2007).

103. Cunningham, B., et al. A plastic colorimetric resonant optical biosensor for multiparallel detection of label-free biochemical interactions. *Sens. Actuators B: Chem.* **85**, 219-226 (2002).

104. Orosco, M.M., Pacholski, C. & Sailor, M.J. Real-time monitoring of enzyme activity in a mesoporous silicon double layer. *Nat. Biotechnol.* **4**, 255-258 (2009).

105. Madeira, A. et al. Coupling surface plasmon resonance to mass spectrometry to discover novel protein-protein interactions. *Nat. Protoc.* **4**, 1023-1037 (2009).

106. Freudiger, C.W. et al. Label-free biomedical imaging with high sensitivity by stimulated Raman scattering microscopy. *Science* **322**, 1857-1861 (2008).

107. http://www.biacore.com/lifesciences/technology/introduction/Flow_cells/index.html

108. Zhang, W., Ganesh, N., Block, I.D., Cunningham, B. T. High sensitivity photonic crystal biosensor incorporating nanorod structures for enhanced surface area. *Sens. Actuators B: Chem.***131**, 279-284 (2008).

109. Popa, A. M. et al. Nanostructured waveguides for evanescent wave biosensors. *Appl. Surf. Sci.* **256S**, S12-S17 (2009).

110. Saarinen, J.J. et al. Reflectance analysis of a multilayer one-dimensional porous silicon structure: Theory and experiment. *J. Appl. Phys.* **104**, 013103 (2008).

111. Park, H. J., Kang, M. G., and Guo, L. J. Large area high density sub-20 nm SiO_2 nanostructures fabricated by block copolymer template for nanoimprint lithography *ACS Nano* 3, 2601-2608 (2009).

112. Mathur, S. et al. Nanostructured films of iron, tin and titanium oxides by chemical vapor deposition. *Thin Solid Films* **502**, 88-93(2006).

113. Kashyap, R. & Nemova, G. Surface Plasmon Resonance-Based Fiber and PlanarWaveguide Sensors. *J. of Sensors* **645162** (2009).

114. http://catalog2.corning.com/Lifesciences/media/pdf/Analysis_of_Small_Molecule_and_Enzyme_Schering_Corning_Poster_PP_%20SBS_2006.pdf

115. http://www.fortebio.com/small_molecule.html

116. Skorobogatiy, M.A. & Kabashin, A. Plasmon excitation by the Gaussian-like core mode of a photonic crystal waveguide. *Opt. Express* **14**, 8419-8424 (2006).

117. Hou, Y., Kim, J. S., Ashkenazi, S., Donnell, M. O. and Guo, L. J., "Optical generation of high frequency ultrasound using two dimensional gold nanostructure," *Appl. Phys. Lett.* 89, 093901 (2006).

118. Hou, Y., Ashkenazi, S., Huang, S. W., and Donnell, M. O. Improvements in optical generation of high frequency ultrasound. *IEEE Trans. Ultrason. Ferroelect. Freq. Contr.* **54**, 682-686 (2007).

119. Hou, Y., Kim, J. S., Ashkenazi, S., Huang, S.W., Guo, L. J. and Donnell, M. O. "Broadband all-optical ultrasound transducers," *Appl. Phys. Lett.* 91, 073507, (2007).

120. Beard, P. C., Perennes, F. and Mills, T. N., "Transduction mechanisms of the Fabry-Perot polymer film sensing concept for wideband ultrasound detection," *IEEE Trans. Ultrason. Ferroelect. Freq. Contr.* 46, 1575-1582 (1999).

121. Foster, S. F., Pavlin, C. J., Harasiewicz,K. A., Christopher, D. A. and Turnbull, D. H. Advances in ultrasound biomicroscopy. *Ultrasound Med. Biol.* **26**, 1-27(2000).

122. Wang, L.H *Photoacoustic Imaging and Spectroscopy* (CRC Press, 2009).

123. Buma, T., Spisar, M. and Donnell, M. O. High-frequency ultrasound array element using thermoelastic expansion in an elastomeric film. *Appl. Phys. Lett.* **79**, 548-550 (2001).

124. Huang, S. W., Chen, S. L., Ling, T., Maxwell, A., and Donnell, M.O. Low-noise wideband ultrasound detection using polymer microring resonators. *Appl. Phys. Lett.* **92**, 193509 (2008).

125. Schneckenburger, H. Total internal reflection fluorescence microscopy: technical innovations and novel applications. *Curr. Opin. Biotech.* **16**, 13-18 (2005).

126. Soboleva, I. V., Descrovi, E., Summonte, C., Fedyanin, A. A. and Giorgis, F. Fluorescence emission enhanced by surface electromagnetic waves on one-dimensional photonic crystals. *Appl. Phys. Lett.* **94**, 231122 (2009).

127. Balaa, K. and Fort, E. Surface Plasmon Enhanced TIRF Imaging. *Imaging & Microscopy* **11**, 55-56 (2009).

128. Chou, S. Y. & Xia, Q. F. Improved nanofabrication through guided transient liquefaction. *Nat. Nanotech.* **3**, 295-300 (2008).

129. Levene, M. J., Korlach, J., Turner, S. W., Foquet, M., Craighead, H. G. and Webb, W.W. Zero-Mode Waveguides for Single-Molecule Analysis at High Concentrations. *Science* **299**, 682-686 (2003).

130. Miyake, T. et al. Real-Time Imaging of Single-Molecule Fluorescence with a Zero-Mode Waveguide for the Analysis of Protein-Protein Interaction. *Anal. Chem.* **80**, 6018-6022 (2008).